Synthesis and Structural Study of Positive Electrode Materials for Rechargeable Li-ion Batteries

A Dissertation Presented

by

Hailong Chen

to

The Graduate School

in Partial Fulfillment of the

Requirements

for the Degree of

Doctor of Philosophy

in

Chemistry

Stony Brook University

May 2009

Stony Brook University

The Graduate School

Hailong Chen

We, the dissertation committee for the above candidate for the Doctor of Philosophy degree, hereby recommend acceptance of this dissertation.

Clare P. Grey – Dissertation Advisor
Professor, Department of Chemistry

Stephen A. Koch – Chairperson of Defense
Professor, Department of Chemistry

Robert F. Schneider
Associate Professor Emeritus, Department of Chemistry

Glenn G. Amatucci (External Committee)
Associate Research Professor, Department of Chemistry
State University of New Jersey, Rutgers

This dissertation is accepted by the Graduate School

Lawrence Martin
Dean of the Graduate School

Abstract of the Dissertation

Synthesis and Structural Study of Positive Electrode Materials for Rechargeable Li-ion Batteries

by

Hailong Chen

Doctor of Philosophy

in

Chemistry

Stony Brook University

2009

The objective of this dissertation work is to improve the rate performance of cathode materials used in LIBs (mostly the $LiMO_2$ type cathode materials) by controlling their particle size and morphology. To achieve this goal, three research programs were performed: (1) the design and development of synthetic methods which allow ready and effective control of both particle size and morphology of the cathode materials; (2) The structural and electrochemical investigation of the cathode materials synthesized in part (1), providing better understanding of how particle size, morphology, and structure (long range and local structure) affect their electrochemical performances, especially their rate performances; (3) the investigation of the growth mechanism of cathode materials under different solution conditions (molten flux, hydrothermal, etc.).

$LiCoO_2$ samples with tunable particle sizes ranging from ~10 nm to sub-micrometers were synthesized by using a co-precipitation method. Synchrotron X-ray diffraction was used to monitor their structural changes *in situ* during the electrochemical charge/discharge cycle. The phase evolution of nano-$LiCoO_2$ was found to be different from that of bulk $LiCoO_2$ and is size-dependent. Electron microscopy was used to study the microstructural changes of highly charged nano-$LiCoO_2$. The appearance of large concentrations of lattice dislocations reveals one of the origins of the capacity fade.

A novel nanostructure of $LiCoO_2$, so called a “desert rose” structure, which resembles the morphology of natural minerals such as Gypsum, is synthesized by a new synthetic method, the low temperature molten salt method. A dissolution-reprecipitation mechanism is proposed to explain the formation of this unusual morphology. A lithium ion battery using this $LiCoO_2$ material as a cathode shows excellent rate performance.

$LiCoO_2$, with a novel and unique morphology, the concaved cuboctahedron, was synthesized by using hydrothermal synthesis. Electron diffraction shows that these particles comprise a 4-fold twin crystal of $LiCoO_2$. The growth mechanism of the twin crystal is proposed to involve selective leaching of CoO and Li-Co ion-exchange in the cubic precursor, CoO, followed by the isotropic growth of the $LiCoO_2$ plates.

Static ^{7}Li NMR spectroscopy, combined with deconvolutional fitting, is used to *in situ* monitor the functioning batteries and to provide information on the local structure of the electrodes.

TABLE OF CONTENTS

LIST OF FIGURES

CHAPTER 1

CHAPTER 2

CHAPTER 3

CHAPTER 4

CHAPTER 5

LIST OF TABLES

CHAPTER 4

CHAPTER 5

LIST OF ABBREVIATIONS

2D, 3D	two-dimensional, three-dimensional
CVD	chemical vapor deposition
DMC	dimethyl carbonate
EC	ethylene carbonate
FWHM	full width at half maximum
HEV	hybrid electric vehicle
LDH	layered double hydroxide
LIB	lithium ion battery
MAS	magic angle spinning
NMP	N-methyl pyrrolidone
PDF	pair distribution function
PVDF	poly-vinylidene fluoride
OCV	open circuit voltage
TEM	transmission electron microscopy
HRTEM	high resolution transmission electron microscopy
SEI	solid-electrolyte-interphase
SEM	scanning electron microscopy
FESEM	field emission scanning electron microscope
STEM	scanning transmission electron microscope
SAED/SAD	selected area electron diffraction/ selected area diffraction

ACKNOWLEDGEMENTS

First and sincerely, I would like to thank my advisor, Professor Clare P. Grey, for her giving me the chance doing exciting research in this group and for her guidance through the last 5 years. Her patience, caring, understanding, encouragements and supports have walked me through every step toward Ph.D. I am forever grateful to her for being my advisor. Her attitude, to science, to research, to teaching, to students and colleges provides me a perfect model of an outstanding scientist and a great teacher. Her dedication to science and her enthusiasm will always inspire me in my future career.

I would also like to thank my committee members, Professor Stephen Koch, Professor Robert Schneider and Professor Glenn Amatucci, for their help and thoughtful advices, which lead me towards a deeper and wider understanding of science.

Prof. Yimei Zhu, Dr. Lijun Wu, Dr. Lihua Zhang and Dr. Dong Su from Brookhaven National Laboratory, Baris Key and Dr. Rangeet Bhattacharyya from the Grey group and Bill Bowden from Duracell Corp. are acknowledged for fruitful discussions and collaborations. Dr. Xiaoqing Yang and Dr. Won-Sub Yoon from BNL are acknowledged for their help on synchrotron experiments and helpful discussions. I also thank Prof.Ying S. Meng from University of Florida, Prof. John Parise, Professor Richard Reeder and Prof. Brian Philips from our university for helpful discussions. I am thankful for the assistance from the beam line scientists and national laboratory scientists: Jonathan Hanson, Peter W. Stephens, Kevin Stone, Wen Wen, Lixia Rong, Jie Zhu, (Brookhaven National Laboratory), Peter L. Lee, Peter J. Chupas, Christopher S. Johnson, and Michael M. Thackeray (Argonne National Laboratory). I also thank Dr. James Quinn for his kind help on TEM and SEM experiments. Yuanzhi Tang is acknowledged for DCP experiments, Shanshan Liang and Feng Zuo for TGA measurements.

I would like to thank all the past and present group members: Nicolas Dupré, Won-Sub Yoon, Benjamin Meyer, Jordi Cabana Jiménez, Ulla Gro Nielsen, Sylvio Indris, Rangeet Bhattacharyya, Fred Blanc, Derek Middlemiss, Peter J. Chupas, Younkee Paik, Namjun Kim, Santanu Chaudhuri, Luming Peng, John Palumbo, Julien Breger, Meng Jiang, Paul Sideris, Stephen Boyd, Nicole Leifer, Lesley Holmes, Hua Huo, Jongsik Kim, Dongli Zeng, Baris Key, Fulya Dogan, Kellie Morgan, Lucienne Buannic, Ken Rosina, Yunxu Zhu, Riza Dervisoglu, Gunwoo, Xiao Hua, Lina Zhou, Hao Wang, Kenia Julmis; and all the visiting scholars ever in the group during my Ph.D: Junichi Shirakawa, Naoko and Zhouguang Lu. I learned a lot from everyone both scientifically and personally, and shared so many unforgettable moments with you. Lauretta Passanant is also thanked for her kindness and help in these years.

I always enjoyed the friendly supports from my peer students in stony brook: Jian Feng, Wei Li, Wenqian Xu, Harris Mason, Stacey Cochiara, Lin Chen, Ti Wang, Feng Zuo, Hongjun Zhou. We have been good friends and invaluable academic colleagues. I am also consistently impressed with them.

I would like to express my thanks to Katherine Hughes and Diane Godden. They are always patient and provide all supports and answers to questions.

My families have always been the greatest support for me. Wandering abroad and being not able to travel back home often, I owe them a thousand thanks and they are always my source of strength and courage. Of course my girlfriend Yuanzhi Tang has been a tremendous support all the time in these 5 years and I feel truly lucky to have her with me. I hold a heartful thanks for her understanding and unselfish support for me. Without her, I would not have stepped this far while still enjoying life so much.

CHAPTER 1

INTRODUCTION

1. For a Greener World: Motivations and Introduction

With the world's population and the averaged energy consumption for each person increasing for the past half century, the world's annual total energy consumption has increased significantly. Fig 1.1 shows the world's annual total energy consumption from 1980 to 2006 based on the 2009 annual report of Department of Energy (DOE) of the United States [1]. Total energy consumption has increased 67% in the 26 years from 1980 to 2006, with a sharper increase in the most recent 10 years. It is very likely that in the year of 2010, the annual total energy consumption will double that of 1980. On the other hand, about four fifths of the produced energy is from fossil fuels, such as oil, natural gas and coal, as shown on the left side of Fig 1.2 [1]. Combustion of these fossil fuels produces huge amounts of greenhouse gases such as carbon dioxide. Although the origin of all sources of global warming is still under debate, the fast increasing emission of greenhouse gases is generally considered as the major cause over the last 50 years.

Among various sources of greenhouse gases emission, emission from petroleum vehicles has drawn lots of public attention. As shown on the right side of Fig. 1.2 [1], about one third of the US total energy consumption is for transportation. Because the

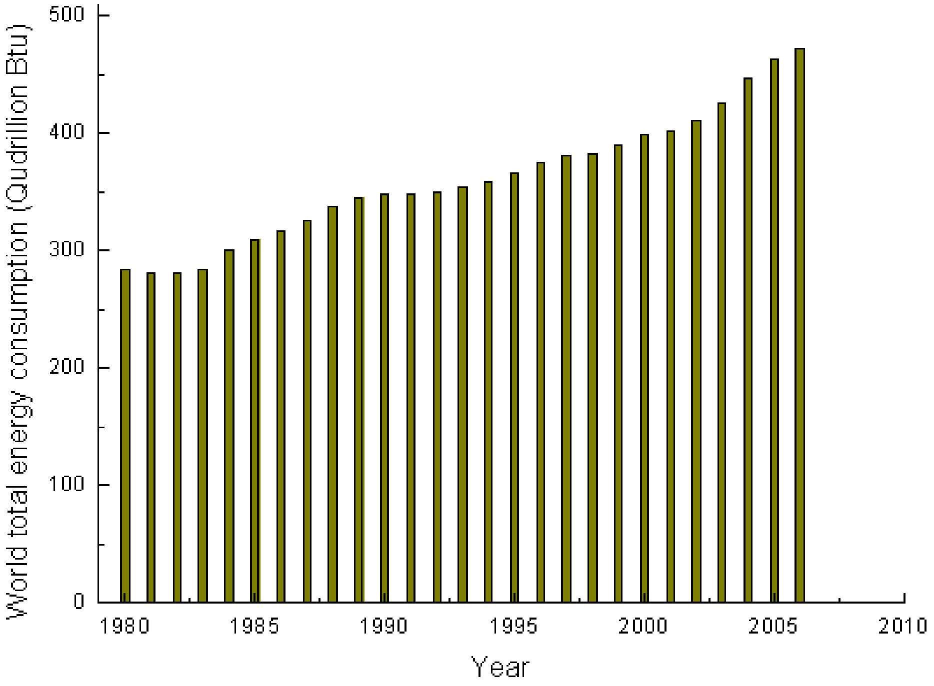

Figure 1.1. The world’s total energy consumption from 1980 to 2006 [1].

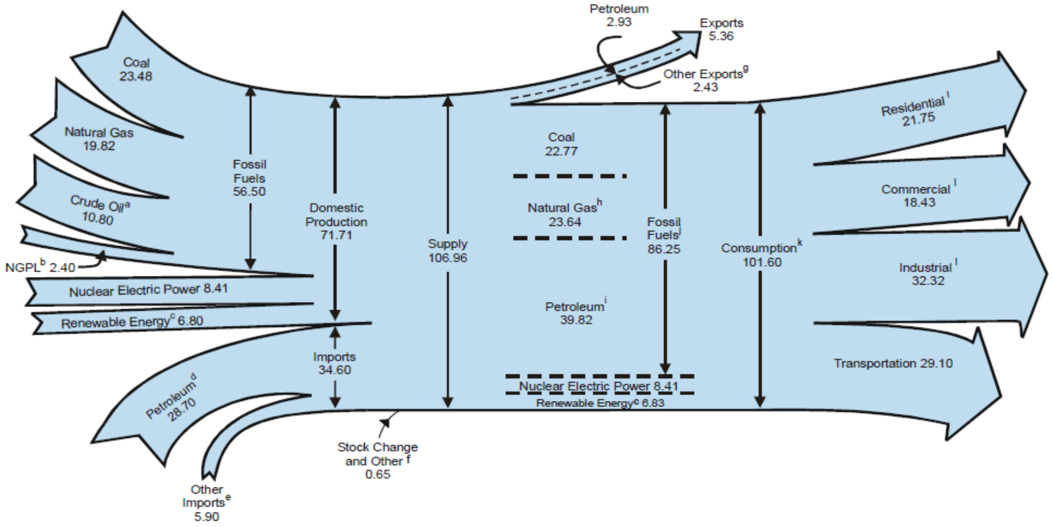

Figure 1.2. Energy production and consumption of the United States in year 2003 [1].

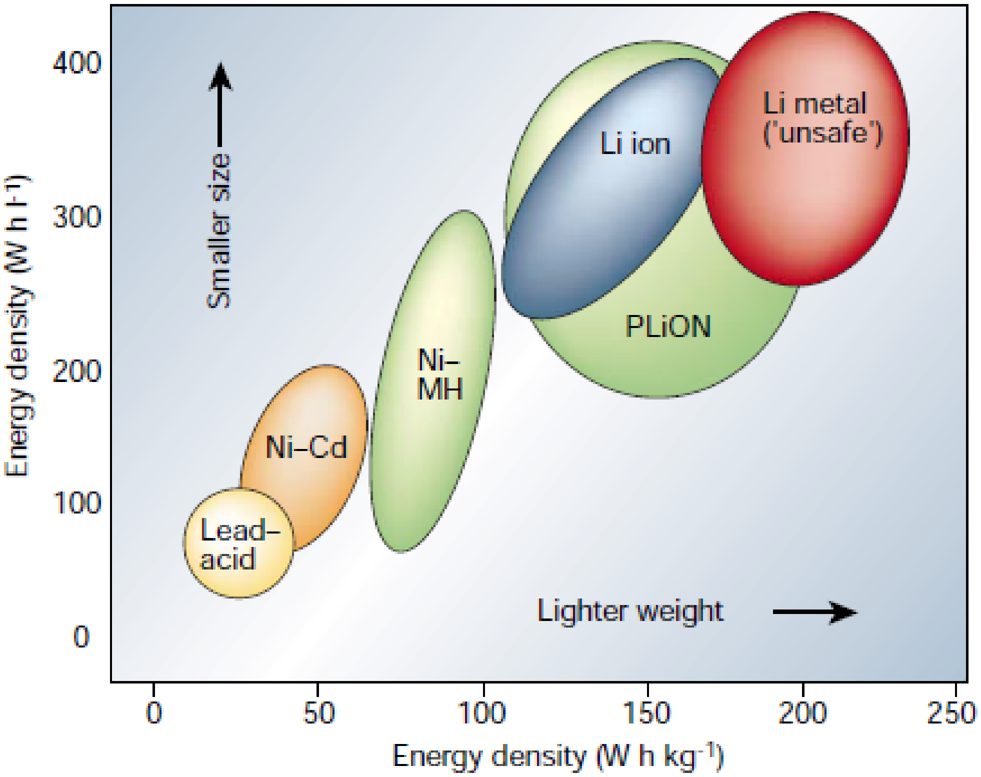

Figure 1.3. A comparison of different battery technologies in terms of volumetric and gravimetric energy density. The share of worldwide sales for Ni–Cd, Ni–MeH and Li-ion portable batteries is 23, 14, and 63%, respectively. The use of Pb–acid batteries is restricted to mainly SLI (starting, lighting, ignition) in automobiles or standby applications. Ni–Cd batteries remain as the most suitable technology for high-power applications (e.g., power tools). Reproduced from reference [2].

energy efficiency of car engines is usually only 18 – 20%, the usage of petroleum vehicles is a huge waste of energy with poor energy usage/gas emission ratios. Using plug-in hybrid electric vehicles (PHEVs) or hybrid electric vehicles (HEV) to replace conventional petroleum vehicles has been suggested as a good solution to this problem, since electric motors can easily afford efficiencies over 90%. To achieve this goal, rechargeable batteries with high enough energy and power densities are required.

Furthermore, to fully utilize other kinds of clean energies such as solar, wind, and hydroelectric energies, problems associated with energy storage and buffering also need to be solved. Using high energy and high power rechargeable batteries represent one possible solution.

Among the various rechargeable batteries ever invented, the lithium ion battery (LIB) shows the best volumetric and gravimetric energy density, as shown in Fig. 1.3 [2]. LIBs also have the advantages of long cycling life and good stability over other rechargeable batteries (e.g., nickel-hydride and lead-acid batteries). Because of the good performances of LIBs, ever since its first commercial production by SONY Co. in 1991, LIBs have become the most popular rechargeable battery as power sources for low energy and portable electric devices, such as cell phones, cameras, and laptop computers. Because of its relative low charge/discharge rate, the application of LIBs for high power tools and devices such as EVs and HEVs, are still limited to a few cases, such as some electric bikes and golf-cars. The motivation of this dissertation work is to improve the rate performance of LIBs, which might have applications for LIBs on high power devices, and will contribute to global efforts to save energy and protect the environment.

There are many factors affecting the high rate performance of LIBs. Li transport/diffusion on the cathode side is believed to be one of the rate-limiting steps in a LIB system. This dissertation work is focused on the improvement of the rate performance of the cathode materials, including: (I) the development of new synthetic methods for lithium transition metal oxides, and the design, synthesis, and electrochemical tests of new cathode materials; and (II) the investigation of the long range order and local structure of synthesized cathode materials, in order to understand the relationships between the electrochemical properties and crystal/electronic structure features of the cathode materials. Complementary techniques will be used, including solid state nuclear magnetic resonance spectroscopy (NMR), X-ray diffraction (XRD) and electron microscopy

2. High Power of Lithium Ion Batteries

2.1. A Lithium Ion Battery System

A LIB system consists of three parts: the cathode, the anode, and the electrolyte. Depending on the type of electrolyte used, LIBs can be generally categorized as (I) all-solid-state LIBs, where all three components are solid state compounds/composites; (II) liquid electrolyte LIBs, where the organic solvent is used to dissolve the electrolyte salts. A polymer membrane separator, soaked with the liquid electrolyte solution, is placed between the cathode and anode, as shown in Fig 1.4 [2]; and (III) polymer LIBs, where electrolyte salts are held in a polymer composite. This dissertation work will focus on the type (II) LIBs, the liquid electrolyte LIBs, because it is currently the most popular and widely used commercial LIB. The charge and discharge process of LIB is schematically shown in Fig.1.5 [3]. In the charge process of LIBs, Li ions are removed from the cathode, diffuse through the electrolyte and relocate in the anode. At the same time, an equal amount of electrons are removed from the cathode, go through the out circuit to the anode. The discharge process is vice versa.

The anode and cathode of LIB are usually Li-intercalation compounds, with the cathode materials having higher potentials to Li/Li^+ than the anodes. Common anode materials include (I) lithium transition metal oxides, e.g., $Li_4Ti_5O_{12}$ [4, 5] and LiV_3O_8 [6, 7]; (II) alloys, e.g., CuSn [8, 9]; (III) binary compounds, e.g., CoO [10] and

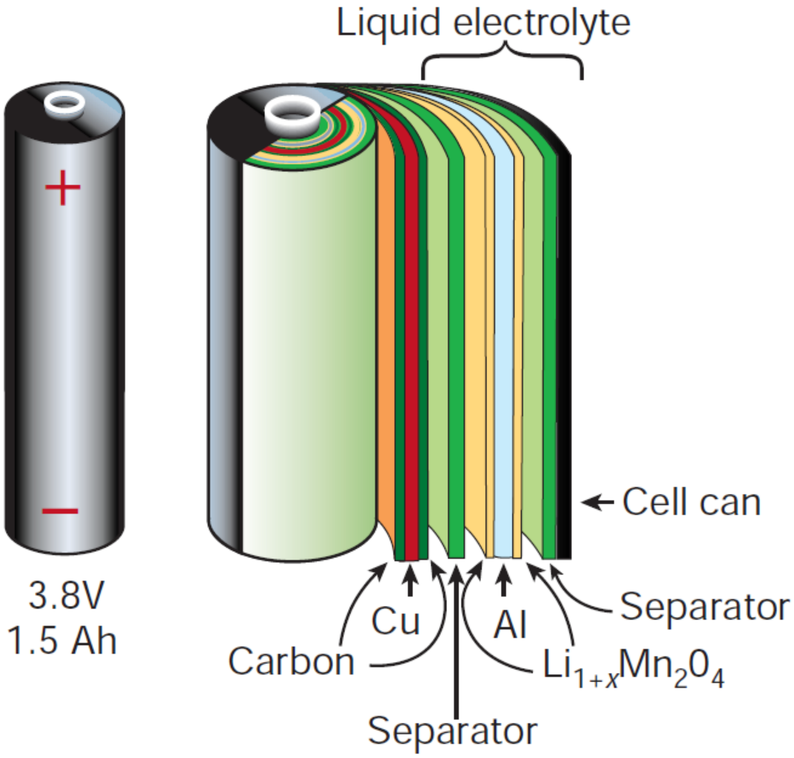

Figure 1.4. Schematics of a cylindrical LIB. Reproduced from reference [2].

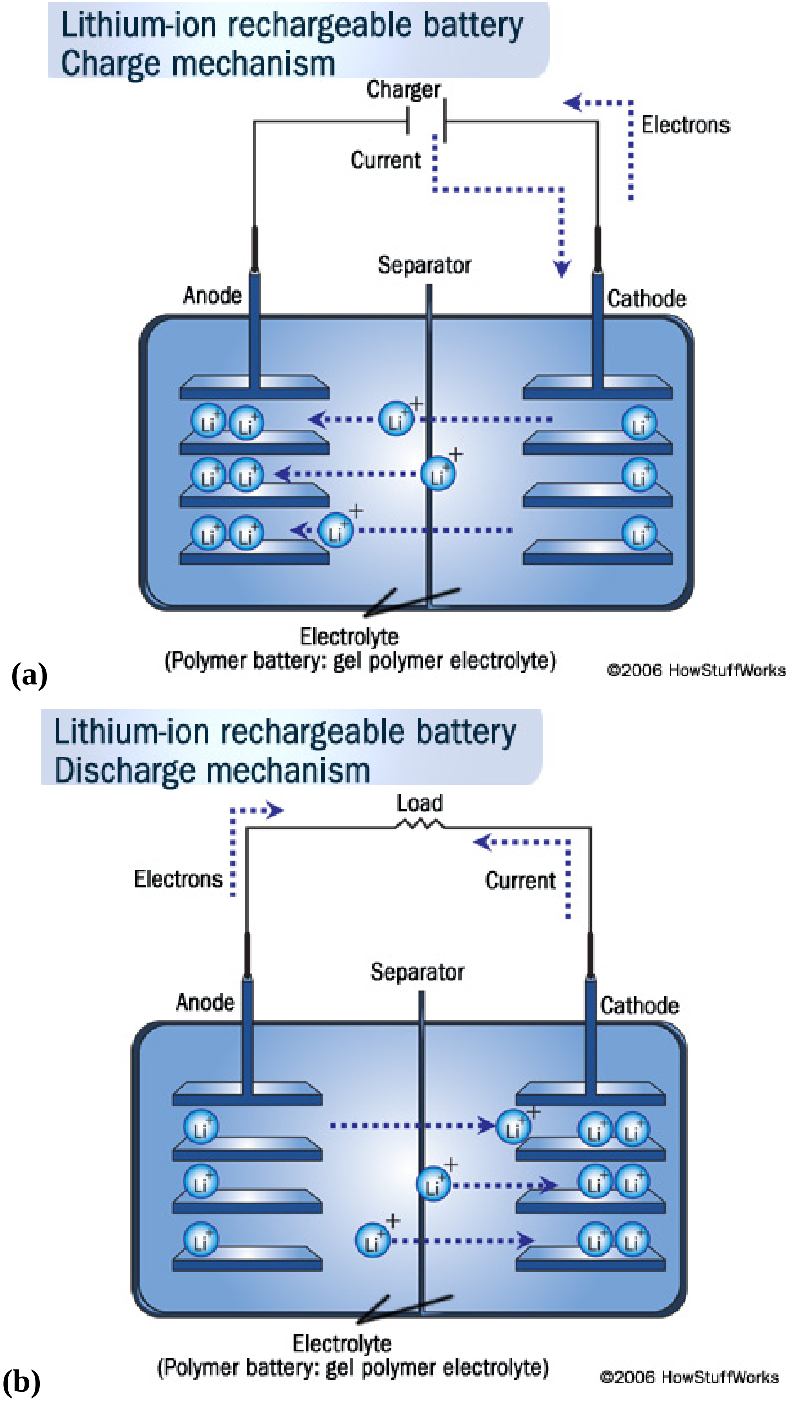

Figure1.5. Schematics of the charge (a) and discharge (b) mechanisms of LIBs. Reproduced from reference [3].

Cu_2O [11, 12]; and (IV) various carbon and silicon materials, e.g., graphite, mesocarbon microbeads (MCMB) [13-15], nanocrystalline silicon [16, 17] and silicon nanowires [18, 19]. Li metal has also been used as anode material in the primary lithium batteries. The serious safety problem due to short circuit caused by the formation of Li dendrites on the surface of Li metal anode makes it unsafe to recharge a primary lithium battery. However, Li metal is still widely used as the anode of LIBs in experimental cells in the laboratories, because it is used also as the reference electrode in order to calibrate the cell potential to Li/Li^+ and to simplify and separate the electrochemical analysis, so that only the processes (vs Li) involving the second electrode material are observed.

The cathodes of LIBs include two main types of materials: the conventional intercalation compounds and the recently developed conversion compounds. The mostly used intercalation compounds can be classified into three types by their crystal lattice types: (I) the layered oxides, e.g., $LiCoO_2$ (the first commercialized cathode material) [20], $LiNiO_2$ [21, 22] and $Li(Ni_{1/3}Co_{1/3}Mn_{1/3})O_2$ [22]; (II) the spinels, e.g., $LiMn_2O_4$ [23, 24]; (III) the olivines, e.g., $LiFePO_4$ [25-29] and $LiMnPO_4$ [30, 31]. These intercalation cathode materials usually have a stable 2-D or 3-D framework consisting of metal-oxygen octahedra or tetrahedra, with Li taking the interstitial sites. During the charge and discharge cycle, Li can be extracted from (charge) and inserted back to (discharge) the framework without significant disruption of the framework. The recently developed conversion compounds are binary compounds with a general formula of A_xB_y (A = metal ions, B = F, O, S, etc.). As compared to the conventional intercalation compounds, these conversion compounds take a quite different scenario of reacting with Li ions, in that the original lattice reforms accompanying the replacement of A (metal ions) by Li and the formation of nanodomains or nanocrystals of the metal, surrounded by lithium salts (Li_2O, LiF, Li_2S etc.) [32, 33].

2.2. Towards High Rate LIBs

2.2.1. The Rate-Limiting Steps in a LIB System

During charge, the diffusion path of Li ions from cathode to anode can be divided to many steps:

1. Li diffusion from the core/bulk of particles of the cathode material to the surface
2. Li transport from the electrode surface to the electrolyte
3. Li diffusion in the liquid electrolyte from cathode side to the anode side through the pores of the separator.
4. Li transport from the electrolyte to the surface of the anode particle
5. Li diffusion from the surface to the core/bulk of particles of the anode material

The discharge process is the reverse of these steps. Among these steps, step 3 is not commonly considered to be a rate-limiting step. Li diffusion in the electrolyte but through the pores in the electrode is now being viewed as a rate-limiting step. The Li self diffusion coefficient (D_S) in various organic solvent-based liquid electrolyte systems have been studied by field gradient NMR. For example, the D_s of Li in $LiPF_6$-PC electrolyte varies from 1.32×10^{-10} m^2/s to 2.04×10^{-10} m^2/s, depending on different concentrations [34]. The D_s of Li in LiPF6-EC/DMC (2:8) system was reported to be in the order of 10^{-10} m^2/s too [35]. During charge/discharge, the Li transport in the electrolyte is mostly ascribed to the electric field gradient driven migration, which is much faster than self-diffusion, therefore, although the above numbers are in the same order of magnitude as those of anodes and cathodes, the rate-limiting steps are more on the electrode side, especially at high rates.

Between the anodes and cathodes of LIBs, the Li diffusion in anodes is usually faster. For example, in graphite, the widely used anode material in commercial LIBs, the Li diffusion coefficient is 3.9×10^{-10} m^2/s [36]. As a comparison, $LiCoO_2$, also a widely used cathode material of commercial LIBs, has a diffusion coefficient of 10^{-11} to 10^{-12} m^2/s, as reported by various groups using different measurement methods [37-39] .

Ionic conductivity is not the only rate-limiting factor for a LIB system. In step 1 and 2 above, Li diffusion should be associated with corresponding electron transport from the lattice of the cathode material, through the conductive additives, to the current collector and outside circuit. Otherwise due to the accumulation of static charges, overpotential against the charging potential will be built up on the surface, and will eventually stop the charge current. This is also true for anodes. But on the other hand, the anode materials, such as graphite, are usually good electrical conductors or semiconductors. However, the cathode materials, most of which are transition metal oxides, are somtimes poor electrical conductors. This may in some systems limit the current density on the cathode. Therefore, improving the electrical conducting of the cathode is very important for improving the cycling rate of LIBs.

In summary, the Li diffusion on the cathode side is believed to be the rate-limit step in most cases. Improving both the ionic and electrical conduction of the cathode is the key to the development of the high rate LIBs.

2.2.2. Approaches to Improve the Rate Performance of Cathode Materials

To improve the rate performance of the cathodes of LIBs, various approaches have been tried previously. A brief summary of some of these approaches is given below:

1. Increase the surface area of electrode, by synthesizing the cathode materials in nanoparticles [40-44], nanowires [45-48], or other nanostructures [49, 50]. This can effectively increase the charge/discharge rate of LIBs. However, the increase of the surface area increases the side reactions of cathode materials and electrolyte/solvents, thus the capacity retention of the batteries is decreased and the self discharge becomes a serious problem.

2. Increase the intrinsic Li diffusion. The Li diffusion in the solid frameworks is determined by the site activation energies and is also closely related to the type and density of defects. For example, $Li(Ni_{1/2}Mn_{1/2})O_2$ was known as material with poor rate performance. Kang et. al [51, 52] used ion-exchange method synthesize $Li(Ni_{1/2}Mn_{1/2})O_2$ from a $Na(Ni_{1/2}Mn_{1/2})O_2$ precursor. This materials showed a much higher discharge rate (up to 6C), than the solid state reaction synthesized $Li(Ni_{1/2}Mn_{1/2})O_{2.}$ It is thought that the

ion-exchange synthesis decreases the Li-Ni exchange, therefore facilitates the Li-diffusion in the 2-D channels.

3. Improvement of the electrical conduction of the cathode. In commercial LIBs, it has been a routine to add small amount (3%-8 wt %) of conductive additive (commonly carbon black) in the cathode composite to facilitate the electrical conduction. It is possible to largely increase the cycling rate of LIBs by adding a large amount, e.g. 30-70wt%, of carbon black to the cathode composite. However, this will also greatly lower the energy and power densities. Other materials of good electrical conductivities, such as carbon nanotubes [53-56] and metal nanowires [57], have been used as conductive additives instead of carbon blacks in order to form a better conductive 3-D network with taken up much less volume and weight percentages of the overall electrode. Carbon or metal coating on the particles of cathode materials has also been extensively studied, especially for the cathode materials with poor electrical conductivities, such as $LiFePO_4$. In very recently work, Kang and Ceder [58] applied a phase-segregation caused coating on non-stoichiometry $LiFePO_4$. This greatly improved the rate capability of $LiFePO_4$. A cycling rate as high as 600C was achieved, but only when using high carbon content.

2.3. High Rate Cathode Materials

2.3.1. $LiCoO_2$ and Layered Oxides

Goodenough et al. first reported the use of $LiCoO_2$ as a cathode materials in 1980 [20]. Ever since its first use in commercial LIBs by SONY Co. in 1991, $LiCoO_2$ has been the most popular cathode material for LIBs. The crystal structure of $LiCoO_2$ is shown in Fig. 1.6. The Co-O octahedra form 2-D layers by edge-sharing and stacking in an ABCABC sequence, with Li-O octahedra residing between these layers through edge-sharing with the Co-O octahedra. Li can diffuse through the octahedral sites in the lithium layer. However, the activation energy for Li diffusion through a tetrahedral intermediate site to the Co layer is much higher. Therefore Li diffusion in this kind of layered material is typically the 2-D diffusion.

The theoretical capacity of $LiCoO_2$ is 274 mAh/g, if all the Li in the formula can be removed. However, in practice, only about 50% of the total Li can be reversibly deintercalated and intercalated. This is due to the irreversible phase transition when more than 50% Li is extracted [59-64]. Therefore, the practical capacity of $LiCoO_2$ is about 130-140 mAh/g, with a working voltage window of 3.5-4.2 V. $LiCoO_2$ performs stably in LIBs and shows long cycling life. But because Co is expensive and toxic, many other transition metals were used to replace Co or to dope for Co in the layered structure. Many lithium-transition metal compounds isostructural to $LiCoO_2$ or with similar layered structures have been studied, e.g., $LiNiO_2$, $LiMnO_2$, $LiNi_{0.8}Co_{0.2}O_2$, $LiNi_{1/2}Mn_{1/2}O_2$, and

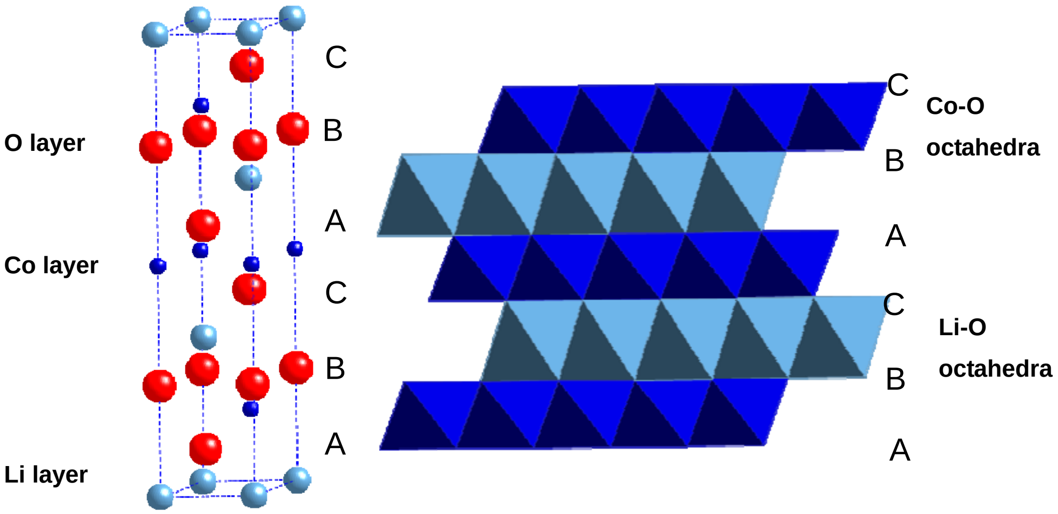

Figure 1.6. Structure of $LiCoO_2$ showing (a) the unit cell, and (b) the ABC-close-packed stacking of the different layers of $LiCoO_2$.

$Li(Ni_{1/3}Co_{1/3}Mn_{1/3})O_2$.

$LiNiO_2$ is isostructural to $LiCoO_2$ and shows higher practical capacity than $LiCoO_2$ [21]. However, the Li intercalation reaction for $LiNiO_2$ is not as reversible as $LiCoO_2$. This is because quite an amount (~3%-12% [65-67]) of Ni site-exchanges with Li blocking the Li diffusion in the 2-D channels. The Mn-doped compound, $LiNi_{1/2}Mn_{1/2}O_2$, has similar problems and shows poor high rate capacities. Kang et al. improved the rate performance of this compound by eliminating Ni-Li exchange in the layers. For $LiCoO_2$, the Co-Li exchange is very small, which is also a reason for $LiCoO_2$ showing better rate performance than these two other compounds. The other multi transition metal-doped compound, $Li(Ni_{1/3}Co_{1/3}Mn_{1/3})O_2$, shows good rate performance. It is also ascribed to the relatively lower Ni-Li exchange [68] by decreasing the amount of Ni and increasing the amount of Co in transition metal layers. Kant et al. also showed that the change on the cation and the separation between the layers played a very important role in controlling the activation energy for diffusion.

The 2-D diffusion of Li in the layered materials suggests that the electrochemical performance of these materials is orientation and morphology dependent. Such electrochemistry-orientation dependence is very obvious for thin film batteries. In the work of Kanno et al., a (110) orientated epitaxially grown $LiCoO_2$ film, with the 2-D channels (between the (003) planes) being exposed at the surface of the thin film, gives a normal charge-discharge curve and good capacity. In comparison, the (003) orientated $LiCoO_2$ film, with the 2-D channels parallel to the surface of the thin film, shows almost no capacity [69, 70]. Similarly, for $LiCoO_2$ powers, morphology of the particles plays an important role in their electrochemical performance. Fig. 1.7a shows the schematics of electrochemically favorable and unfavorable morphologies of $LiCoO_2$ particles. For the hexagonal plate-like morphology, the “active surface”, which is defined as the surface where Li ion can be extracted from or inserted to the lattice, is on the thin edges of the particle, and the area is very small. However, the “non-active surface”, i.e., the (003) surface, is very large. Since Li intercalation reaction can only occur through the active surface on the edges, this morphology is not electrochemically favorable. On the other hand, the rod- or wire-like morphologies, with very small (003) surface and large “active surface”, are expected to be electrochemically favorable. Unfortunately, for $LiCoO_2$ and other layered compounds with hexagonal lattices, the common morphology from solid state reaction and hydrothermal synthesis is plate-like or rounded hexagonal blocks. Fig.1.7b shows the typical morphology of $LiCoO_2$ synthesized by hydrothermal method, which shows poor rate performance. Therefore, to improve the rate performance of the layered materials, morphology control is very important.

2.3.2. $LiMn_2O_4$

Because of the low cost and environmental friendliness of Mn over Co, $LiMn_2O_4$ has been extensively studied as cathode material for LIBs [71]. Fig. 1.8 shows the crystal structure of $LiMn_2O_4$. It has a spinel-type lattice structure, with a 3-D framework formed

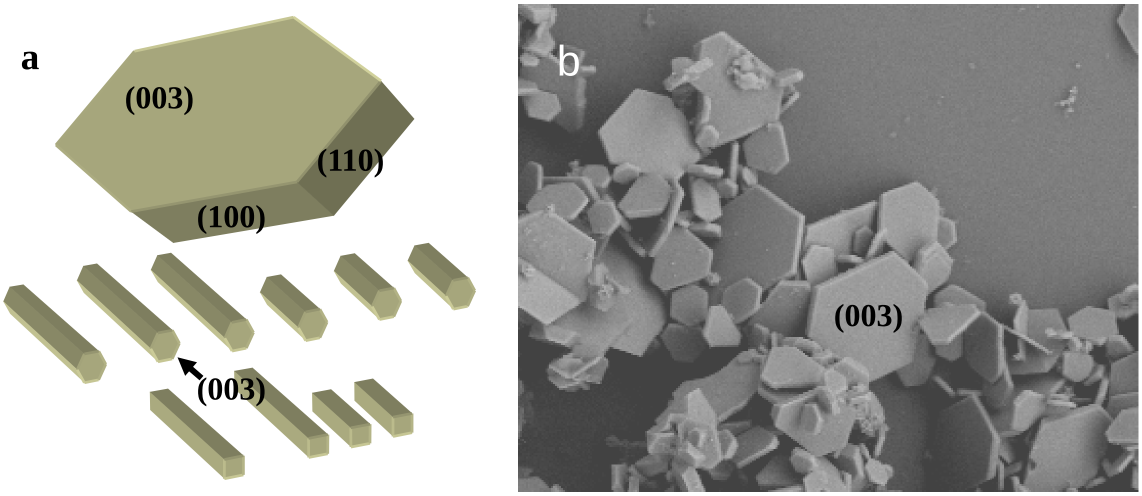

Figure 1.7. (a) Schematics of electrochemically unfavored (plate-like) and favored (rod-like) morphology morphologies of layered $LiMO_2$ materials. (b) Morphology of $LiCoO_2$ synthesized by a hydrothermal method. The (003) face of one hexagonal particle is marked

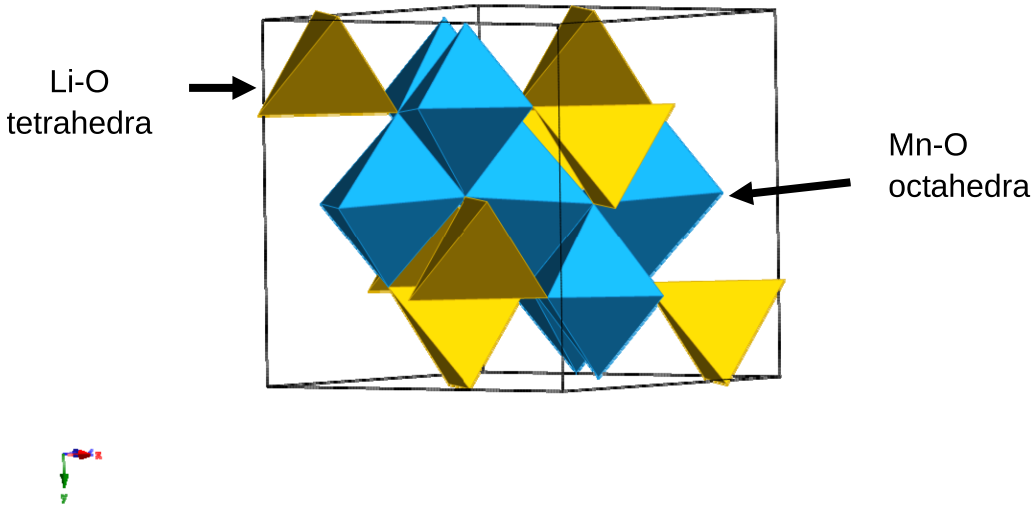

Figure 1.8. Structure of $LiMn_2O_4$.

by edge-sharing Mn-O octahedral. Li sits in the tetrahedral interstitial sites. Because it has a cubic (space group Fd-3m) lattice, Li diffusion in this material is through the 3-D channels and thus is isotropic. This 3-D style diffusion is expected to be more capable of high rate cycling than the 2-D type. However, this material shows some problems on cycling. First is the Mn dissolution in the electrolyte. This has a large effect on the cyclability, especially at elevated temperatures (e.g., 55 ^{o}C) [72, 73]. The theoretical capacity of $LiMn_2O_4$ is only 120 mAh/g, lower than the layered compounds. This is because the reaction of Li with $LiMn_2O_4$ to form $Li_2Mn_2O_4$ is associated with the Jahn-Teller distortion of Mn^{3+} and this reaction cannot be used in a practical LIB. In fact, due to this problem, the practical capacity of $LiMn_2O_4$ is only 110 mAh/g, since dopants are added to prevent the Jahn-Teller distortion occurring on deep discharge [74, 75].

2.3.3. $LiFePO_4$

The application of $LiFePO_4$ as a cathode material for LIBs was first reported by Goodenough and co-workers in 1997 [25]. The framework of $LiFePO_4$ and its delithiated phase, $FePO_4$, are shown in Fig.1.9 [25]. Both belong to the tetragonal space group P*nma*, and only differ slightly in cell parameters in order to accommodate the occupation of Li ions. The intercalation/deintercalation of Li into the framework is almost 100% reversible. However, when first reported, the electrochemical performance of $LiFePO_4$, especially its cycling rate, was poor due to its low electronic conductivity. Armand and coworkers [76],

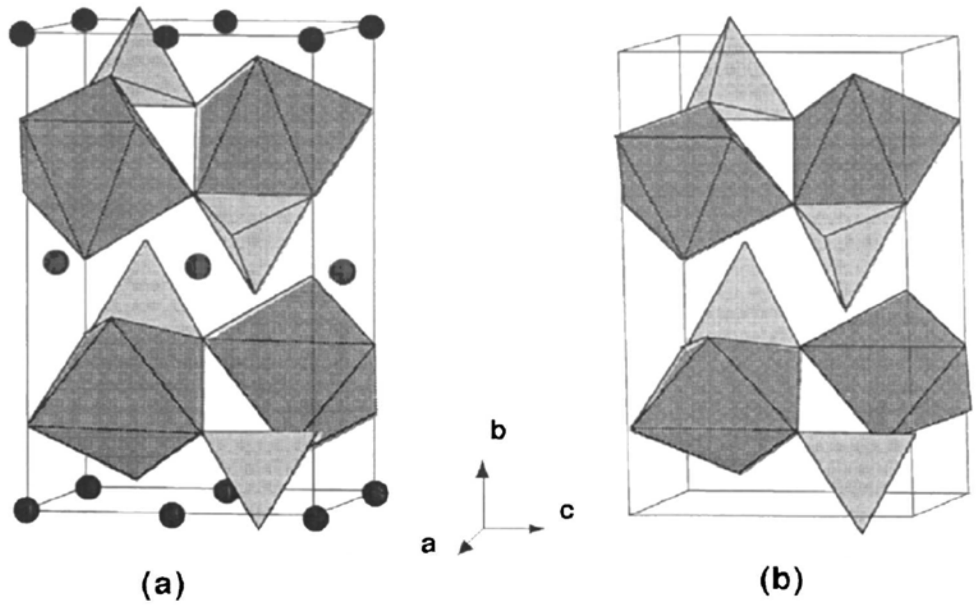

Figure 1.9. Structure of (a) $LiFePO_4$ and (b) $FePO_4$. PO_4 and FeO_6 groups are shown in light tetrahedra and dark octahedra, respectively. Li atoms are shown as black spheres.

Chiang and coworkers [26] and Nazar and coworkers [28] improved the capacity and rate performance of $LiFePO_4$ by making it nanocrystalline and by using carbon coating to improve its electronic conductivity and possibly via doping, although this has generated considerable debate. Recently, Kang and Ceder [58] reported a surprising improvement of the rate performance of $LiFePO_4$. They used a non-stoichiometric ratio of Fe to P in the starting materials to grow a very thin coating layer on the surface of the $LiFePO_4$ nanoparticles by phase-segregation upon heat treatment. This coating layer contains highly ionic and electrical conductive species such as FeP and $Li_2FeP_2O_7$, which they proposed facilitated Li transport in the batteries. A constant 60C cycling without obvious capacity fading and a highest rate of 600C were demonstrated using this material as cathode in the LIBs. This result may further open up the possibilities of using LIBs as power sources for plug-in EVs, or for applications where supercapacitors have traditionally been used.

Although $LiFePO_4$ has a 3-D framework, both theoretical calculations [77, 78] and experimental observations [79] show that Li diffusion in $LiFePO_4$ is 1-D type, through the channels along *b* direction. This suggests that the rate performance of $LiFePO_4$ may also depend on the morphology of its primary particle. Its rate performance may be further improved by controlling the morphology of the particles.

3. Objectives and Outline

The objective of this dissertation work is to improve the rate performance of the cathode materials of LIBs (mostly the $LiMO_2$ type cathode materials) by control their particle size and morphology. To achieve this goal, three parts of research work were carried on: (1) the design and development of synthetic methods which allow readily and effective control on both particle size and morphology of the cathode materials; (2) The structural and electrochemical investigation of the synthesized cathode materials, which provides better understanding of how particle size, morphology, and structure (long range and local structure) affect their electrochemical performances, especially their rate performances; (3) the investigation of the growth mechanism of cathode materials in solution under different conditions (molten flux, hydrothermal, etc.). The overall methodology of this dissertation is summarized in Fig. 1.10.

In Chapter 2, the new co-preicipitation synthetic method will be discussed. The electrochemical performances of $LiCoO_2$ and other layered compounds obtained by using this method will be studied. As a model compounds, $LiCoO_2$, with nanoparticles, is carefully investigated on its long range and local structures, both as-synthesized and upon cycling, by using comprehensive analytical methods such as synchrotron XRD, NMR etc.

In Chapter 3, the molten salt synthesis and the novel nanostructure of $LiCoO_2$ synthesized by using this method is investigated. The growth mechanism of this unusual morphology of $LiCoO_2$ is also discussed.In Chapter 4, the hydrothermal synthesis method and a unique morphology of $LiCoO_2$ obtained by using this method is studied. The growth mechanism is proposed based on crystallographic possibilities and is proved by combined analytical techniques.

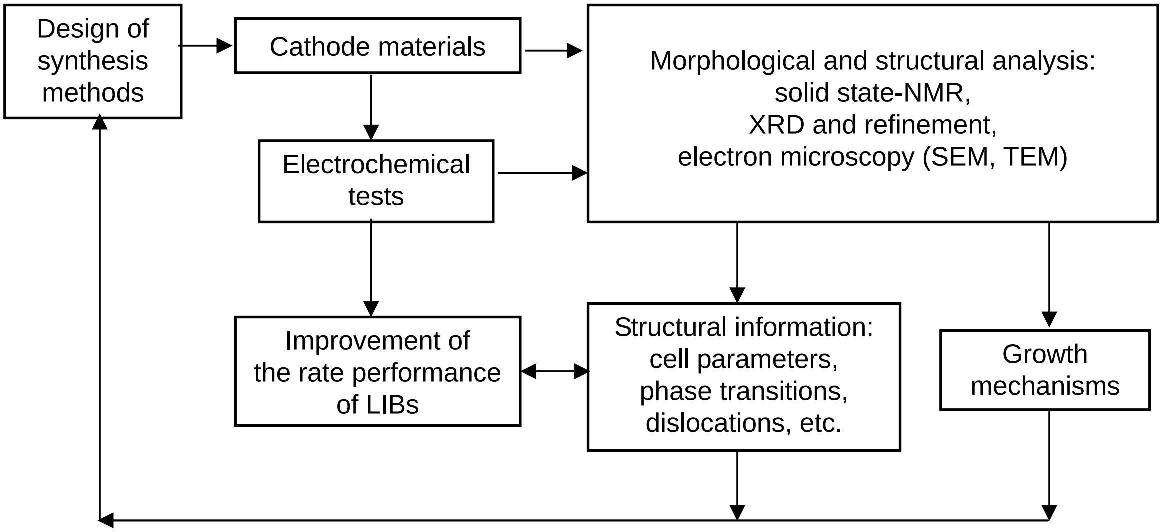

Figure 1.10. Summary of the experimental strategies of this dissertation work.

REFERENCE

1. http://www.energy.gov/.
2. Tarascon, J. M.; Armand, M., *Nature* **2001,** 414, (6861), 359-367.
3. www.howstuffswork.com.
4. Ferg, E.; Gummow, R. J.; Dekock, A.; Thackeray, M. M., *J. Electrochem. Soc.* **1994,** 141, (11), L147-L150.
5. Zaghib, K.; Simoneau, M.; Armand, M.; Gauthier, M., *J. Power Sources* **1999,** 81, 300-305.
6. Cao, A. M.; Hu, J. S.; Liang, H. P.; Wan, L. J., *Angew. Chem. Int. Edit.* **2005,** 44, (28), 4391-4395.
7. West, K.; ZachauChristiansen, B.; Skaarup, S.; Saidi, Y.; Barker, J.; Olsen, II; Pynenburg, R.; Koksbang, R., *J. Electrochem. Soc.* **1996,** 143, (3), 820-825.
8. Kepler, K. D.; Vaughey, J. T.; Thackeray, M. M., *J. Power Sources* **1999,** 81, 383-387.
9. Tamura, N.; Ohshita, R.; Fujimoto, M.; Fujitani, S.; Kamino, M.; Yonezu, I., *J. Power Sources* **2002,** 107, (1), 48-55.
10. Poizot, P.; Laruelle, S.; Grugeon, S.; Dupont, L.; Tarascon, J. M., *Nature* **2000,** 407, (6803), 496-499.
11. Debart, A.; Dupont, L.; Poizot, P.; Leriche, J. B.; Tarascon, J. M., *J. Electrochem. Soc.* **2001,** 148, (11), A1266-A1274.

12. Park, J. C.; Kim, J.; Kwon, H.; Song, H., *Adv. Mater.* **2009,** 21, (7), 803-+.

13. Mabuchi, A.; Tokumitsu, K.; Fujimoto, H.; Kasuh, T., *J. Electrochem. Soc.* **1995,** 142, (4), 1041-1046.

14. Richard, M. N.; Dahn, J. R., *J. Electrochem. Soc.* **1999,** 146, (6), 2068-2077.

15. Wang, Q.; Li, H.; Chen, L. Q.; Huang, X. J., *Solid State Ionics* **2002,** 152, 43-50.

16. Li, H.; Huang, X. J.; Chen, L. Q.; Wu, Z. G.; Liang, Y., *Electrochem. Solid State Lett.* **1999,** 2, (11), 547-549.

17. Li, H.; Huang, X. J.; Chen, L. Q.; Zhou, G. W.; Zhang, Z.; Yu, D. P.; Mo, Y. J.; Pei, N., *Solid State Ionics* **2000,** 135, 181-191.

18. Cui, L. F.; Ruffo, R.; Chan, C. K.; Peng, H. L.; Cui, Y., *Nano Lett.* **2009,** 9, (1), 491-495.

19. Chan, C. K.; Peng, H. L.; Liu, G.; McIlwrath, K.; Zhang, X. F.; Huggins, R. A.; Cui, Y., *Nat. Nanotechnol.* **2008,** 3, (1), 31-35.

20. Mizushima, K.; Jones, P. C.; Wiseman, P. J.; Goodenough, J. B., *Mater. Res. Bull.* **1980,** 15, (6), 783-789.

21. Dahn, J. R.; Vonsacken, U.; Juzkow, M. W.; Aljanaby, H., *J. Electrochem. Soc.* **1991,** 138, (8), 2207-2211.

22. Ohzuku, T.; Makimura, Y., *Chem. Lett.* **2001**, (7), 642-643.

23. Thackeray, M. M.; David, W. I. F.; Bruce, P. G.; Goodenough, J. B., *Mater. Res. Bull.* **1983,** 18, (4), 461-472.

24. Thackeray, M. M.; Johnson, P. J.; Depicciotto, L. A.; Bruce, P. G.; Goodenough, J.

B., *Mater. Res. Bull.* **1984,** 19, (2), 179-187.

25. Padhi, A. K.; Nanjundaswamy, K. S.; Goodenough, J. B., *J. Electrochem. Soc.* **1997,** 144, (4), 1188-1194.

26. Chung, S. Y.; Bloking, J. T.; Chiang, Y. M., *Nat. Mater.* **2002,** 1, (2), 123-128.

27. Yamada, A.; Chung, S. C.; Hinokuma, K., *J. Electrochem. Soc.* **2001,** 148, (3), A224-A229.

28. Huang, H.; Yin, S. C.; Nazar, L. F., *Electrochem. Solid State Lett.* **2001,** 4, (10), A170-A172.

29. Yang, S. F.; Zavalij, P. Y.; Whittingham, M. S., *Electrochem. Commun.* **2001,** 3, (9), 505-508.

30. Li, G. H.; Azuma, H.; Tohda, M., *Electrochem. Solid State Lett.* **2002,** 5, (6), A135-A137.

31. Delacourt, C.; Poizot, P.; Morcrette, M.; Tarascon, J. M.; Masquelier, C., *Chem. Mater.* **2004,** 16, (1), 93-99.

32. Li, H.; Balaya, P.; Maier, J., *J. Electrochem. Soc.* **2004,** 151, (11), A1878-A1885.

33. Li, H.; Richter, G.; Maier, J., *Adv. Mater.* **2003,** 15, (9), 736-739.

34. Zhao, J. S.; Wang, L.; He, X. M.; Wan, C. R.; Jiang, C. Y., *J. Electrochem. Soc.* **2008,** 155, (4), A292-A296.

35. Capiglia, C.; Saito, Y.; Kageyama, H.; Mustarelli, P.; Iwamoto, T.; Tabuchi, T.; Tukamoto, H., *J. Power Sources* **1999,** 81, 859-862.

36. Doyle, M.; Newman, J.; Gozdz, A. S.; Schmutz, C. N.; Tarascon, J. M., *J.*

Electrochem. Soc. **1996,** 143, (6), 1890-1903.

37. Xie, J.; Imanishi, N.; Matsumura, T.; Hirano, A.; Takeda, Y.; Yamamoto, O., *Solid State Ionics* **2008,** 179, (9-10), 362-370.

38. Dokko, K.; Mohamedi, M.; Fujita, Y.; Itoh, T.; Nishizawa, M.; Umeda, M.; Uchida, I., *J. Electrochem. Soc.* **2001,** 148, (5), A422-A426.

39. Xia, H.; Lu, L.; Meng, Y. S.; Ceder, G., *J. Electrochem. Soc.* **2007,** 154, (4), A337-A342.

40. Kim, D. H.; Kim, J., *Electrochem. Solid State Lett.* **2006,** 9, (9), A439-A442.

41. Bao, S. J.; Liang, Y. Y.; Zhou, W. H.; He, B. L.; Li, H. L., *J. Power Sources* **2006,** 154, (1), 239-245.

42. Sun, Y. K.; Myung, S. T.; Kim, M. H.; Prakash, J.; Amine, K., *J. Electrochem. Soc.* **2005,** 127, (38), 13411-13418.

43. Chen, H. L.; Qiu, X. P.; Zhu, W. T.; Hagenmuller, P., *Electrochem. Commun.* **2002,** 4, (6), 488-491.

44. Hwang, B. J.; Santhanam, R.; Liu, D. G., *J. Power Sources* **2001,** 97-8, 443-446.

45. Park, D. H.; Lim, S. T.; Hwang, S. J.; Yoon, C. S.; Sun, Y. K.; Choy, J. H., *Adv. Mater.* **2005,** 17, (23), 2834-+.

46. Zhou, Y. K.; Huang, J.; Li, H. L., *Appl. Phys. B-Lasers Opt.* **2003,** 76, (1), 53-57.

47. Zhou, Y. K.; Huang, J.; Shen, C. M.; Li, H. L., *Mater. Sci. Eng. A-Struct. Mater. Prop. Microstruct. Process.* **2002,** 335, (1-2), 260-267.

48. Hosono, E.; Kudo, T.; Honma, I.; Matsuda, H.; Zhou, H. S., *Nano Lett.* **2009,** 9,

(3), 1045-1051.

49. Li, N. C.; Patrissi, C. J.; Che, G. L.; Martin, C. R., *J. Electrochem. Soc.* **2000,** 147, (6), 2044-2049.

50. Sides, C. R.; Martin, C. R., *Adv. Mater.* **2005,** 17, (1), 125-+.

51. Breger, J.; Kang, K.; Cabana, J.; Ceder, G.; Grey, C. P., *J. Mater. Chem.* **2007,** 17, (30), 3167-3174.

52. Kang, K. S.; Meng, Y. S.; Breger, J.; Grey, C. P.; Ceder, G., *Science* **2006,** 311, (5763), 977-980.

53. Zhang, Q. T.; Qu, M. Z.; Niu, H.; Yu, Z. L., *New Carbon Mater.* **2007,** 22, (4), 361-364.

54. Li, X. L.; Kang, F. Y.; Bai, X. D.; Shen, W., *Electrochem. Commun.* **2007,** 9, (4), 663-666.

55. Li, X. L.; Kang, F. Y.; Shen, W. C., *Carbon* **2006,** 44, (7), 1334-1336.

56. Li, X. L.; Kang, F. Y.; Shen, W. C., *Electrochem. Solid State Lett.* **2006,** 9, (3), A126-A129.

57. Yang, X. L.; Wen, Z. Y.; Huang, S. H.; Zhu, X. J.; Zhang, X. F., *Solid State Ionics* **2006,** 177, 2807-2810.

58. Kang, B.; Ceder, G., *Nature* **2009,** 458, (7235), 190-193.

59. Lee, K. P.; Manesh, K. M.; Kim, K. S.; Gopalan, A. Y., *J. Nanosci. Nanotechnol.* **2009,** 9, (1), 417-422.

60. Zhou, F.; Zhao, X. M.; Liu, Y. Q.; Li, L.; Yuan, C. G., *J. Phys. Chem. Solids* **2008,**

69, (8), 2061-2065.

61. Bates, J. B.; Dudney, N. J.; Neudecker, B. J.; Hart, F. X.; Jun, H. P.; Hackney, S. A., *J. Electrochem. Soc.* **2000,** 147, (1), 59-70.

62. Wang, H. F.; Jang, Y. I.; Huang, B. Y.; Sadoway, D. R.; Chiang, Y. T., *J. Electrochem. Soc.* **1999,** 146, (2), 473-480.

63. Amatucci, G. G.; Tarascon, J. M.; Klein, L. C., *J. Electrochem. Soc.* **1996,** 143, (3), 1114-1123.

64. Ozawa, K., *Solid State Ionics* **1994,** 69, (3-4), 212-221.

65. Rougier, A.; Gravereau, P.; Delmas, C., *J. Electrochem. Soc.* **1996,** 143, (4), 1168-1175.

66. Peres, J. P.; Weill, F.; Delmas, C., *Solid State Ionics* **1999,** 116, (1-2), 19-27.

67. Wang, M. J.; Navrotsky, A., *Solid State Ionics* **2004,** 166, (1-2), 167-173.

68. Whitfield, P. S.; Davidson, I. J.; Cranswick, L. M. D.; Swainson, I. P.; Stephens, P. W., *Solid State Ionics* **2005,** 176, (5-6), 463-471.

69. Hirayama, M.; Sakamoto, K.; Hiraide, T.; Mori, D.; Yamada, A.; Kanno, R.; Sonoyama, N.; Tamura, K.; Mizuki, J., *Electrochim. Acta* **2007,** 53, (2), 871-881.

70. Hirayama, M.; Sonoyama, N.; Abe, T.; Minoura, M.; Ito, M.; Mori, D.; Yamada, A.; Kanno, R.; Terashima, T.; Takano, M.; Tamura, K.; Mizuki, J., *J. Power Sources* **2007,** 168, (2), 493-500.

71. Gummow, R. J.; Dekock, A.; Thackeray, M. M., *Solid State Ionics* **1994,** 69, (1), 59-67.

72. Jang, D. H.; Shin, Y. J.; Oh, S. M., *J. Electrochem. Soc.* **1996,** 143, (7), 2204-2211.

73. Xia, Y. Y.; Zhou, Y. H.; Yoshio, M. *J. Electrochem. Soc.* **1997**, 144, 2593-2600.

74. Amine, K.; Tukamoto, H.; Yasuda, H.; Fujita, Y., *J. Electrochem. Soc.* **1996,** 143, (5), 1607-1613.

75. Arora, P.; Popov, B. N.; White, R. E., *J. Electrochem. Soc.* **1998,** 145, (3), 807-815.

76. Ravet, N.; Chouinard, Y.; Magnan, J. F.; Besner, S.; Gauthier, M.; Armand, M., *J. Power Sources* **2001,** 97-8, 503-507.

77. Wang, L.; Zhou, F.; Meng, Y. S.; Ceder, G., *Phys. Rev. B* **2007,** 76, (16).

78. Islam, M. S.; Driscoll, D. J.; Fisher, C. A. J.; Slater, P. R., *Chem. Mater.* **2005,** 17, (20), 5085-5092.

79. Nishimura, S.; Kobayashi, G.; Ohoyama, K.; Kanno, R.; Yashima, M.; Yamada, A., *Nat. Mater.* **2008,** 7, (9), 707-711.

CHAPTER 2

Structure Evolution and Microstructural Changes of Nano-$LiCoO_2$ upon Electrochemical Cycling by in situ X-ray Diffraction, Electron Microscopy and ^{7}Li NMR Spectroscopy

Hailong Chen, Clare Grey

Department of Chemistry

Stony Brook University, Stony Brook, NY 11794-3400

To be submitted to

Chem. Mater.

ABSTRACT

$LiCoO_2$ samples with tunable particle sizes ranging from ~10 nm to sub-micrometers were synthesized by using a co-precipitation method. Synchrotron X-ray diffraction was used to monitor the structural changes of $LiCoO_2$ with 100 and 300 nm average particle sizes in situ during the electrochemical charge/discharge cycle. The phase evolution of nano-$LiCoO_2$ was found to be different from that of bulk $LiCoO_2$ and is size-dependent. ^{7}Li MAS NMR was used to study the insulator-metal transition of nano-$LiCoO_2$ during charge. A self-discharge process was identified that is significant for the nanoparticles. Electron microscopy was used to study the microstructure change of highly charged nano-$LiCoO_2$. The appearance of huge concentrations of lattice dislocations reveals one of the origins of the capacity fade.

1. INTRODUCTION

One strategy that has been widely explored in recent years to increase the rate performance of lithium ion batteries (LIBs) is to use nanoparticles, nanowires and nanostructures as cathode or anode materials. Many synthetic methods have been used to obtain nanometric samples of the cathode materials, mostly lithium transition metal oxides (The recently-developed olivine phosphates and binary compounds as conversion type cathode materials will not be discussed in this chapter, but represent important classes of electrode materials where the size appears to play a significant role in controlling capacity reversibility). The common methods used include: sol-gel, hydrothermal/solvothermal, CVD (chemical vapor deposition), template synthesis and thermal hydrolysis. The “mixed-hydroxide” method [1] has been widely used in lab-scale syntheses of various lithium transition metal oxides. By using this method, molecular level mixing of transition metal cations in the layered double hydroxide (LDH) precursors is achieved. However, the usual mixed hydroxides method is still not a good method to synthesize nanoparticles. This is due to (i) the significant agglomeration of the LDH nanoparticles that can happen in aqueous solutions, (ii) high calcination temperature, that is required for the reaction of the Li salts with the precursors, which results in large particles. Here we use another relatively straightforward approach to prepare smaller particles: we use organic solvents, such as ethanol or acetone, instead of water, to make the mixed-hydroxides precursor [2]. By using this method, nanoparticles of a series of compounds, such as $LiCoO_2$, $Li(Ni_{1/2}Mn_{1/2})O_2$, $Li(Ni_{1/3}Co_{1/3}Mn_{1/3})O_2$ were obtained. The size and morphology of the particles can be controlled by tuning the calcination temperature and time. The as synthesized materials were tested in experimental coin cells and many of them show excellent high rate performances.

$LiCoO_2$ was selected as a model compound to study the possible size-dependent electrochemical properties of layered $LiMO_2$ (M=transition metals) compounds. *In situ* synchrotron XRD was used to study the long range structural changes of $LiCoO_2$ with different particle sizes during the charge/discharge processes. *Ex situ* ^{7}Li MAS NMR was used to study the local structural changes of these samples and in situ static ^{7}Li NMR was also use to follow the local structure changes in real time.

2. EXPERIMENTAL

2.1. Synthesis

In a typical synthesis (shown in Fig. 2.1), ethanol-soluble lithium salts and cobalt salts such as $LiNO_3$ and $Co(NO_3)_2$ were dissolved in absolute ethanol to form a clear, reddish solution. The solution was slowly added into a 3 M KOH in ethanol solution under vigorous stirring. A dark green slurry was initially formed which gradually turned to dark brown. The slurry was filtered and dried to obtain the solid precursor, which contains mixed metal hydroxides (LiOH and $Co(OH)_2$) and some potassium salts. The precursor was then calcined in air in a box furnace for 5-24 hours at various temperatures from 400 to 600^{o}C. The product was cooled down to room temperature and washed with distilled water three times to remove the potassium salts impurities. The final product was dried at 80^{o}C overnight.

2.2. Sample characterization

The dried samples were characterized by using a Scintag (PAD-X) X-ray diffractometer or a Rigaku Miniflex X-ray diffractometer to check the phase purity. Cell parameters were extracted from pattern fitting and calculation by using JADE. ^{7}Li or ^{6}Li MAS NMR was used to investigate the stoichiometry of $LiCoO_2$ samples and the local structure of other samples.

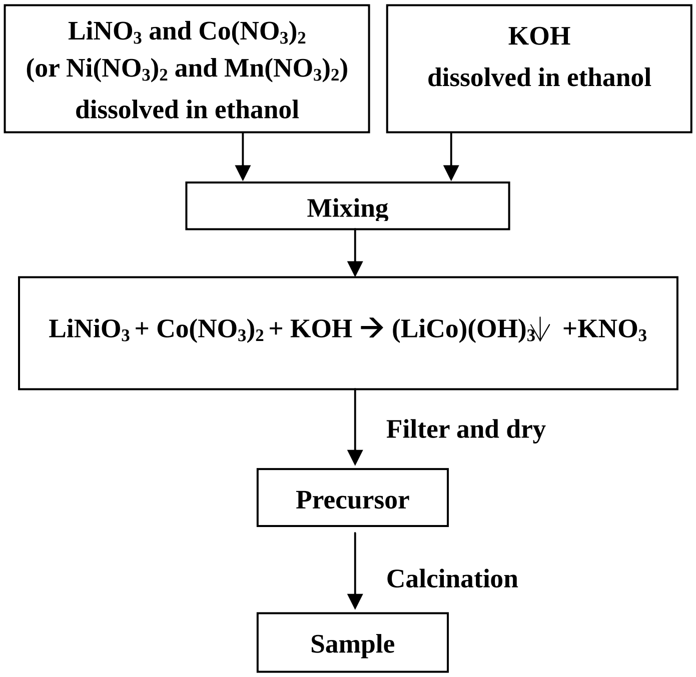

Figure 2.1. Schematics showing the co-precipitation synthesis procedure.

2.3. Electrochemical tests

The positive electrode mixture for electrochemical experiments was made with $LiCoO_2$ samples mixed with poly-vinylidene fluoride (PVDF) binder and acetylene black (6:1:3 wt %) in N-methyl pyrrolidone (NMP) to make thick slurry. The slurry was deposited on an aluminum foil by the doctor-blade method and dried at 80 ^{o}C overnight. Coin cells (CR2032, Hoshen Corp.) were assembled in an argon-filled glove box. Each cell typically contained 3-8 mg of active material, separated from the Li foil anode by a piece of Celgard separator (Celgard, Inc., U.S.A.). A 1 M solution of $LiPF_6$ in ethylene carbonate/dimethyl carbonate (1:1) was used as the electrolyte. Galvostatic electrochemical experiments were carried out with an Arbin Instruments (College Station, TX) battery cycler at various rates.

2.4. *In situ* Synchrotron X-ray Diffraction Experiments

The *in situ* cell used for the synchrotron XRD experiments is shown in Fig. 2.2.a. Fig. 2.2b shows the schematics of the construction of the cell [3]. The cell was assembled in an argon-filled glove box. Li foil, Celgard separator and cathode film (all pre-soaked with electrolyte) were put in sequence in the middle of a kapton tape lined aluminum plate. Then the other kapton tape lined aluminum plate was put on top of the assembly and was carefully aligned so as to avoid a short circuit. An insulating rubber O ring was put in between the Al plates to seal the cell and keep it air and moisture free. Screws on the edges were used to seal the cell and also to generate sufficient pressure to make good contacts between the different components. The cell was connected to an electrochemical cycler and mounted on a goniometer and aligned on the diffractometer at the beamline station, allowing the X-ray beam penetrate through the middle of the kapton window perpendicularly without hitting any part of the Al frame. The cell was cycled at a specific rate/current, set by the cycler, and the diffraction patterns were collected at the same time by using a 2D image plate or position sensitive detector (PSD). These experiments were carried on at beamline X7B and X18A at the National Synchrotron Light Source located at Brookhaven National Laboratory. A wavelength ~0.92 Å and a typical sample-detector distance of 180mm were used.

2.5. ^{7}Li NMR Experiments

^{7}Li NMR experiments were carried on using a Chemagnetics 4.7 T magnet controlled by a CMX200 spectrometer. A 1.8 mm fast spinning probe, a 4 mm probe and a 4 mm static probe were used. The pristine $LiCoO_2$ samples were dried at 80°C overnight before being packed in the rotors. The electrochemically delithiated $LiCoO_2$ was prepared as follow: A CR2032 coin cell was used to cycle the $LiCoO_2$ samples with Li foil as the anode. The cell was charged at rate of C/10 or C/20 and was stopped when a certain amount of Li, for example, 10%, was deintercalated from nano-$LiCoO_2$. The deintercalated Li amount was determined from the theoretical capacity of $LiCoO_2$ (274 mAh/g), assuming 100% columbic efficiency. Electrochemically delithiated $LiCoO_2$ samples were recovered from batteries in an Ar-filled glove box right after they were stopped at desired SOC (state of charge). The cathode film was dried at room temperature after washing with DMC or was used as is, depending on the experimental requirements. The spectra were collected using a rotor synchronized Hahn Echo pulse sequence and a 3 μs $\pi/2$ time was used. The typical pulse delay was 0.5 s for pristine samples and 1 s for charged samples.

2.6. Electron Microscopy Experiments.

The TEM samples of pristine nano-$LiCoO_2$ were prepared as follows: the pristine nano-$LiCoO_2$ powder was dispersed in absolute ethanol and ultrasonicated for 5 minutes to reduce the agglomeration of the fine particles. One drop of this suspension was dropped onto a lacey carbon thin film coated 400 mesh copper grid and the grid was dried at room temperature. To prepare the TEM sample of the charged $LiCoO_2$, the same procedure as described above for NMR experiments was used, except that after the cell was dissembled, the $LiCoO_2$ powder was scratched from the Al film, dispersed in DMC and ultrasonicated in the glove box. The dried copper grid with sample on it was kept in a glass vial until it was put in the pre-vacuum chamber of the TEM.

The low resolution TEM images were collected using a Philips CM12 TEM. The high resolution images and corresponding electron diffraction patterns were collected using a JOEL 4000 and a JOEL 2100F HRTEM.

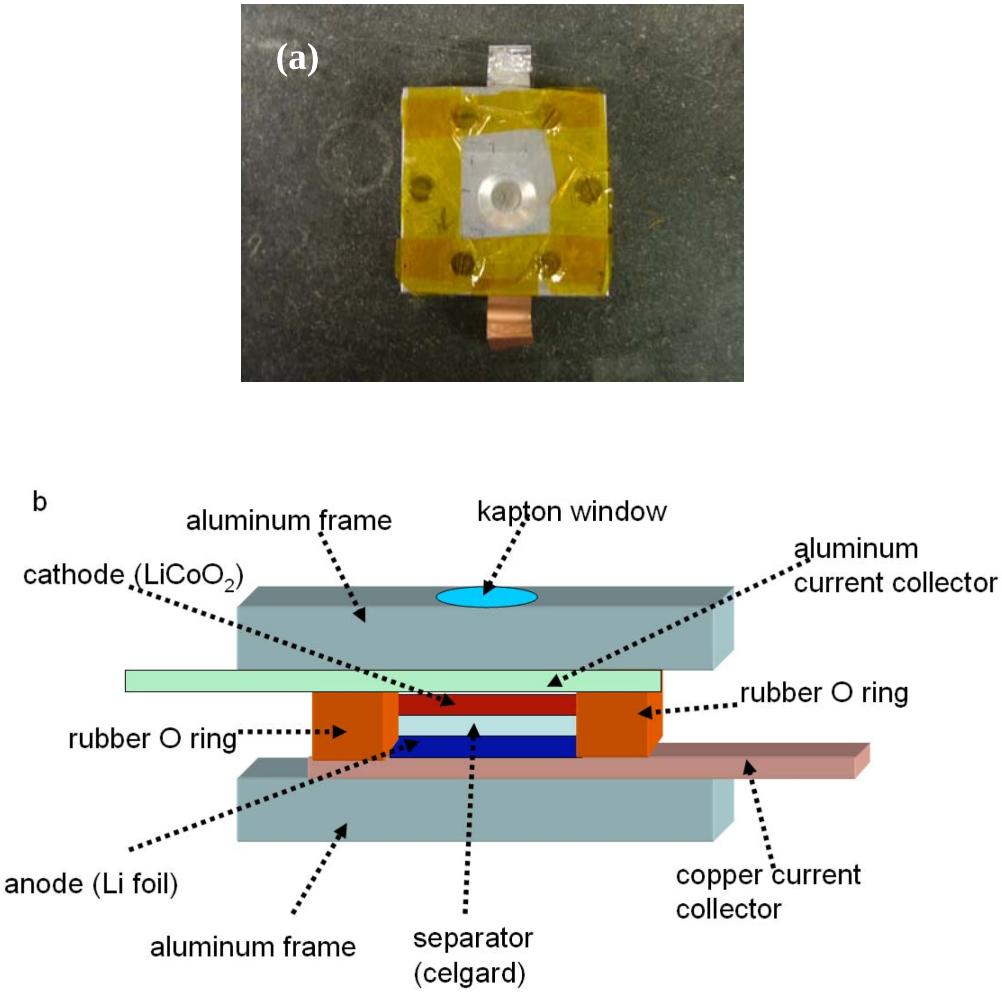

Figure 2.2. (a) Photo of an *in situ* cell; (b) Schematics showing the cross section of the *in situ* cell.

3. RESULTS AND DISCUSSION

3.1. Synthesis and Characterization of Pristine $LiCoO_2$ Particles

3.1.1. X-ray Diffraction

The mixed-hydroxides precursors containing LiOH, $Co(OH)_2$ and precipitated Li/K salts, formed using the procedure shown in Fig. 2.1 were dried overnight at 80°C. Phase-pure $LiCoO_2$ products were obtained by firing the precursor powder in air at various temperatures (400-650°C) and washing with distilled water to remove the excess Li/K salts. Fig. 2.3 shows the XRD pattern of $LiCoO_2$ sample prepared at various temperatures for different times. Cell parameters *a*, *c* and the *c/a* ratio extracted from the XRD reflections for different samples are listed in Table 1. These cell parameters are consistent with that reported by Okubo et al [4]. The particle size are also calculated from the FWHM with the Debye Scherrer equation and listed in Table 1. The results show that the particle size can be readily controlled by changing the calcination time or by annealing the sample at various temperatures. Sharper and intense reflections are seen for the samples calcined at higher temperature for longer heating times, indicating the increase of particle size and crystallinity. By this method, the particle size can be controlled to vary between 10 nm (400°C) to sub-micrometer range with a good size distribution (also see TEM results in next section). Slow cooling and quench experiments were also done to see effect of cooling on the morphology, but no significant differences were observed.

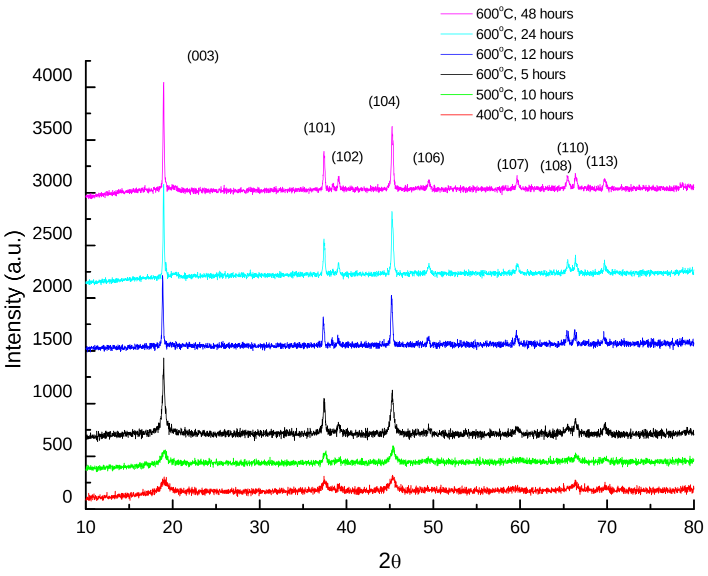

Figure 2.3. XRD patterns of $LiCoO_2$ prepared at various temperatures and reactions times. From bottom to top: 400 ^oC, 10 hr; 500 ^oC, 10 hr; 600 ^oC, 5 hr; 600 ^oC, 12 hr; 600 ^oC, 24 hr; and 600 ^oC, 48 hr. Reflections are indexed to a R-3m space group and labeled in parenthesis.

Table 1. Cell parameter and averaged particle size from XRD of $LiCoO_2$ samples synthesized at various temperatures and times

Sample	*a* (Å)	*c* (Å)	*c/a*	Particle size (nm)
600°C, 48 h	2.81(45)	14.05(06)	4.99	84
600°C, 24 h	2.81(46)	14.04(94)	4.99	80
600°C, 12 h	2.81(76)	14.12(37)	5.01	79
600°C, 5 h	2.81(35)	14.04(85)	4.99	34
500°C, 10 h	2.80(79)	14.06(42)	5.00	14
400°C, 10 h	2.81(65)	14.05(14)	4.99	8

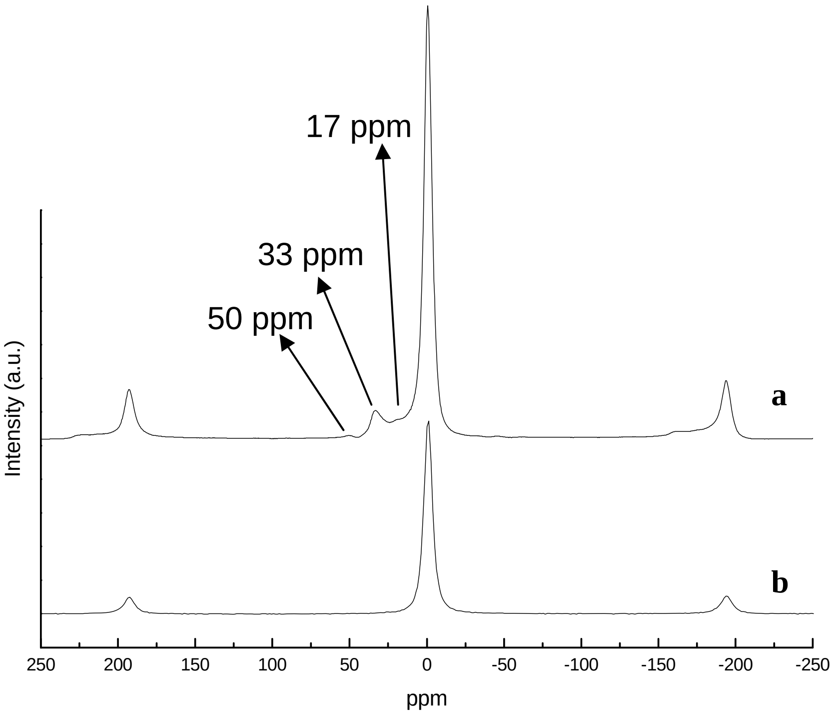

Figure 2.4. ^{7}Li MAS NMR of $LiCoO_2$ samples obtained using Li:Co ratios of (a) 1.2:1, and (b) 1.4:1 for the starting materials, and fired at 600 °C for 5 hr.

To obtain a further understanding of this synthetic method, the effect of other experimental parameters, such as starting materials, solvents, Li:Co ratio etc. were also explored. Nitrates ($LiNO_3$ and $Co(NO_3)_2.6(H_2O)$) and chlorides (LiCl and $CoCl_2$) were used as the starting materials respectively to study the effect of starting materials. The results show the chlorides and nitrates starting materials combinations can produce phase-pure $LiCoO_2$, but the chlorides starting materials sometimes give products with a small amount of Co_3O_4 impurity. One possible reason for this is the lower solubility of chlorides in comparison to nitrates in ethanol is smaller and the competitive adsorption of these chlorides makes it harder for LiOH to fully precipitate and mix with $Co(OH)_2$.

The Li:Co ratio was found to be the most critical factor to obtain phase pure and stoichiometric $LiCoO_2$. Calculations based on the solubility of LiOH in water and ethanol indicates that the ideal Li:Co ratio in starting materials is 1.3-1.4:1 when the concentration of the starting materials is 3 M and100 ml ethanol is used as solvent. ^7Li or ^6Li NMR is very sensitive to the slight change of the stoichiometry of $LiCoO_2$ because defects due to either excess Li or Li-deficiency result in different local environment for Li near the defects. Thus result in a series of characteristic Li resonances, even though defects do not lead to significant changes in the XRD reflections [5-9]. Fig 2.4 shows ^7Li MAS NMR of $LiCoO_2$ samples obtained with different starting material Li:Co ratios, fired at 600°C for 5 hours. The sample with Li:Co ratio=1.2:1 shows obvious characteristic resonances for Li-deficient $Li_{1-x}CoO_2$, at 33 ppm, -7 ppm, 16 ppm etc. [5-9]. In contrast, the sample with Li:Co ratio=1.4:1 shows only one diamagnetic resonance expected for stoichiometric $LiCoO_2$. (This ratio is used to synthesize the samples investigated in this chapter) Samples calcined at 500^{o}C wer also investigated and again the NMR showed to be dependent on the Li:Co ratio in starting materials. The results from the experiments were consistent with the calculation within a reasonable range, although in the experimental case the dissolving-precipitation equilibrium is more complicated. This results show that it is possible to control the stoichiometry of $LiCoO_2$ prepared by using this method, and the preliminary results shown above indicate that quality control of the starting materials and the solvents is very important.

3.1.2. Transmission electron microscopy (TEM)

TEM was used to investigate the morphology and particle size of $LiCoO_2$ samples. Fig. 2.5 shows TEM images of $LiCoO_2$ nanoparticles obtained by using the co-precipitation method. The typical morphology of a sample calcined at 500^{o}C for 10 hours is shown in Fig 2.5b. The particle size ranges from 50-100 nm. Analysis of multiple TEM images of this sample shows that the dominant morphology of the primary particle is rod-like. Fig 2.5 d shows a high resolution TEM image of the same sample. The spacing of the fringes shown in this figure is 0.47 nm, which correspond to the d-spacing of the (003) planes of $LiCoO_2$. This morphology is uncommon for micrometric $LiCoO_2$ obtained from mixed hydroxide and hydrothermal methods [10, 11], in which thin hexagonal plates are usually seen, or high temperature solid state reaction [12, 13], in which rounded and truncated short hexagonal blocks are typically seen. The heating

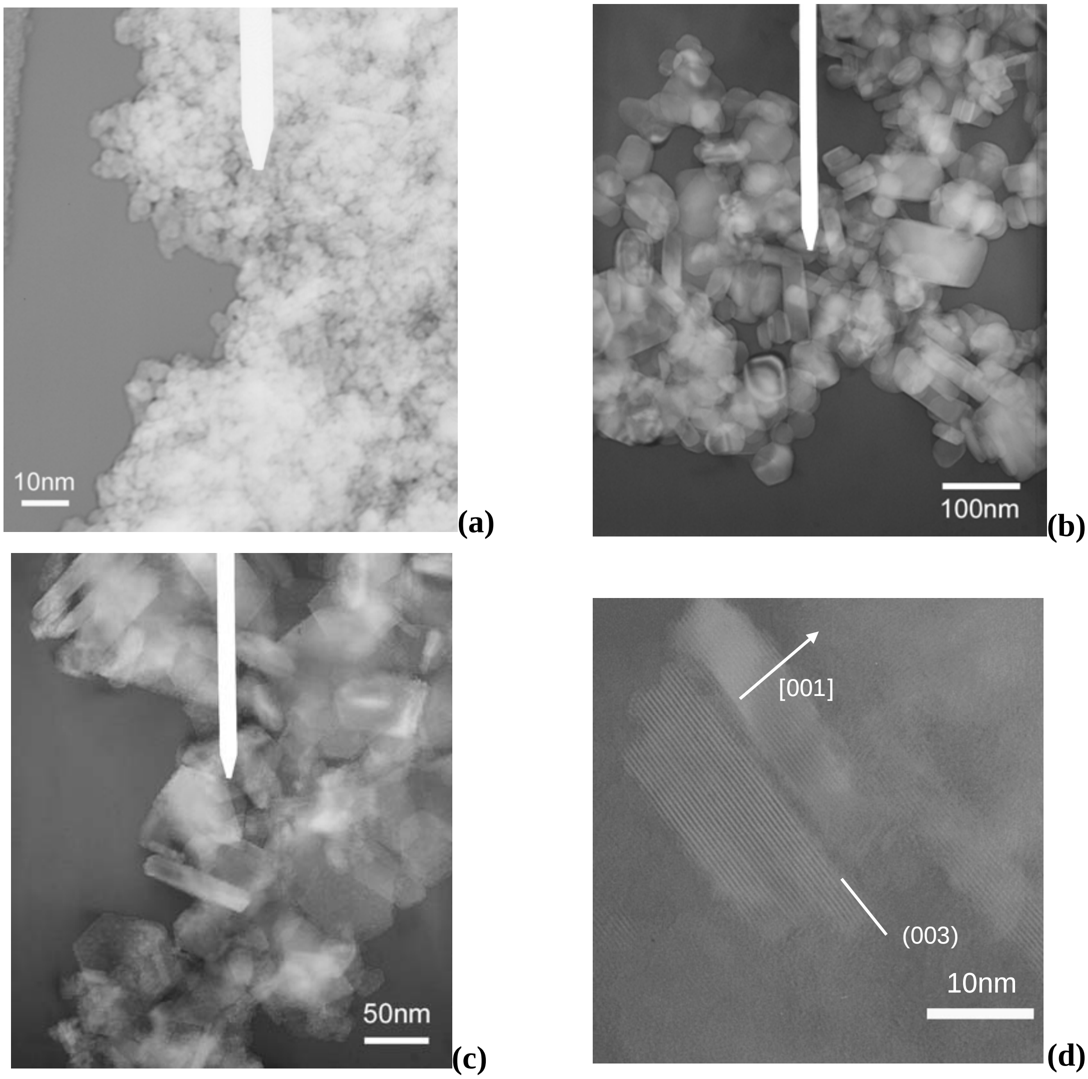

Figure 2.5. TEM images of $LiCoO_2$ nanoparticle samples synthesized at different temperature: (a) 400 °C, 10 hours, (b) 500 °C, 10 hours, (c) 600 °C, 10 hours, and (d) high resolution image of the sample shown in (b).

temperature was varied to study its effect on the size and morphology of $LiCoO_2$. The particle size of the sample synthesized at 600^oC is about 100 nm; the particle size for the sample synthesized at 500^oC is from 50-80 nm; when the calcination temperature is lowered down to 400^oC, the particle size is very small, even less than 10 nm, as shown in Fig. 2.5a. (also see Table 1.) Thus the calcination temperature plays a very important role in controlling the particle size of $LiCoO_2$. When the calcination temperature is high, e.g. 600^oC and above, other than the rod-like particles, hexagonal plate-like particles are seen. As the calcination temperature increases or the heating time increases, more plate-like particles and fewer rod-like particles are formed. While at lower temperatures, e.g. $400\text{-}500^oC$, more rod-like particles are obtained. The 400^oC sample shows a smaller aspect ratio than the 500^oC sample, the particle resembling small cubes or bricks. Thus, although the thermodynamically stable morphology of $LiCoO_2$ at high temperature appears to be hexagonal plates, by this co-precipitation method, we can achieve a control over the growth kinetics to obtain the metastable morphologies, the cube/bricks and the rods, which we believe may be electrochemistry preferred morphologies. We will explore this hypothesis in next sections.

3.1.2. $Li(Ni_{1/2}Mn_{1/2})O_2$ and $Li(Ni_{1/3}Co_{1/3}Mn_{1/3})O_2$

Cathode materials other than $LiCoO_2$ were also prepared by this method. Fig. 2.6 shows the XRD patterns of materials with nominal stoichiometry $Li(Ni_{1/2}Mn_{1/2})O_2$ and $Li(Ni_{1/3}Co_{1/3}Mn_{1/3})O_2$ prepared at 600^oC. The very broad reflections imply very small

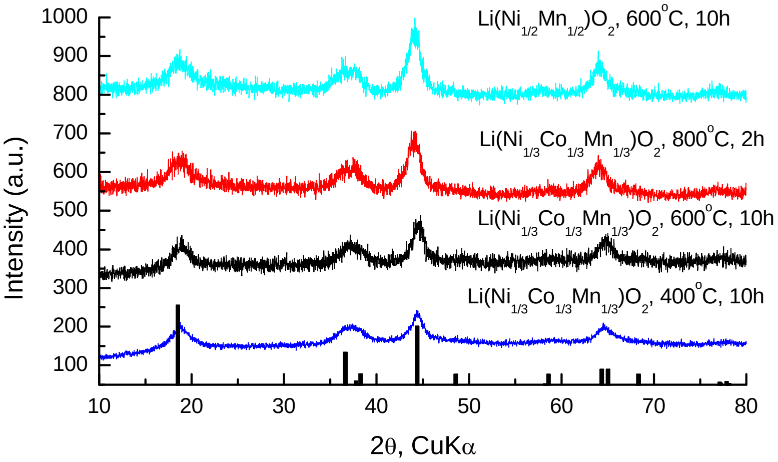

Figure 2.6. XRD patterns of $Li(Ni_{1/2}Mn_{1/2})O_2$ and $Li(Ni_{1/3}Co_{1/3}Mn_{1/3})O_2$ synthesized under different conditions. Black streaks indicate the calculated position and relative intensity of $Li(Ni_{1/3}Co_{1/3}Mn_{1/3})O_2$ XRD reflections.

particle sizes. The particles of these two compounds are even finer than $LiCoO_2$. This is ascribed to the smaller particle/clusters formed by $Ni(OH)_2$ and $Mn(OH)_2$ in the ethanol solution.

The fact that this non-aqueous system co-precipitation method gives finer particles than the usual mixed hydroxides method for all the materials showed here is ascribed to following reasons: 1. In ethanol or acetone, LiOH is not soluble and is co-precipitated out together with the LDHs. This makes a very good mixing of LiOH and the LDHs, and allows them to react at much lower calcination temperature and a shorter time being reqired for complete reaction. 2. The agglomeration of the precursors, which is caused by formed by surface bonding, such as hydrogen bonding and electrostatics, between the neighboring particles, is decreased due to a significant decrease of the polarity of the organic solvents compared with aqueous solution. The agglomerated particles can growth rather quickly when they are dried at temperature even as low as $80^{o}C$. This may be due to formation of increased bonding between the particles, instead of bonding with hydrogen bonds, between the particles, which is due to the dehydration on the surface. Fig 2.7 shows XRD pattern of $Co(OH)_2$ obtained in ethanol and aqueous solutions. It is very obvious that the sample produced in ethanol is much finer, showing much broader diffraction peaks. The variation of the peak widths is due to the isotropic particle shape, which is common for LDHs [14]. 3. Li/K salts/hydroxides are adsorbed on the surface of the mixed hydroxides. The side products of the precipitation reaction are Li/K salts. These salts, especially chlorides, are not very soluble in ethanol. And because no washing

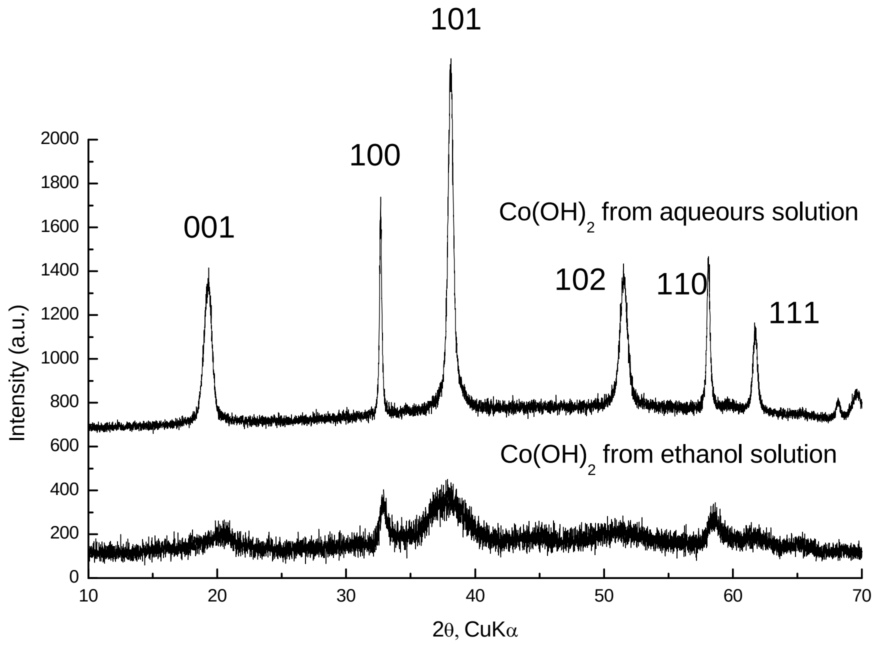

Figure 2.7. XRD patterns of $Co(OH)_2$ obtain from titration in aqueous solution and ethanol solution

procedure was performed after filtering, given that washing by either ethanol or distilled water can cause LiOH loss in the hydroxides mixture, some Li/K salts remain in the mixture and presumably cover the surface of the hydroxides. The weight ratio of these salts to the "real" precursors is estimated to be about 2:1, by comparing the actual weight of the precursor and the theoretical weight of the LiOH-Co(OH)$_2$ mixture. These salts are mostly low melting Li/K nitrates or hydroxides, and in the following calcination process, they form thin layer of highly viscous molten salts around the particle, thus effectively preventing the fast growth of nanoparticles at elevated temperatures. This result is consistent with the molten salts synthesis reported by various groups [15-27], where large amount of molten salts were used to mediate the reaction and nanometric or submicrometric LiMO$_2$ particle were obtained. The growth of LiMO$_2$ crystals in molten salts will be discussed in detail in the next chapter.

3.2. Electrochemical tests

Electrochemical tests have been carried out with LiCoO$_2$, Li(Ni$_{1/2}$Mn$_{1/2}$)O$_2$ and Li(Ni$_{1/3}$Co$_{1/3}$Mn$_{1/3}$)O$_2$ samples. Fig. 2.8 shows the cycling capacity of LiCoO$_2$ sample calcined at 600^{o}C for 10 hours and, as a comparison, the cycling capacity of commercial LiCoO$_2$ (Sigma-Adrich) is also shown (for simplicity, the LiCoO$_2$ samples synthesized by using the co-precipitation method is denoted as nano-LiCoO$_2$ in the rest of this thesis). Nano-LiCoO$_2$ shows a 131 mAh/g capacity at the first discharge at a cycling rate of 7C

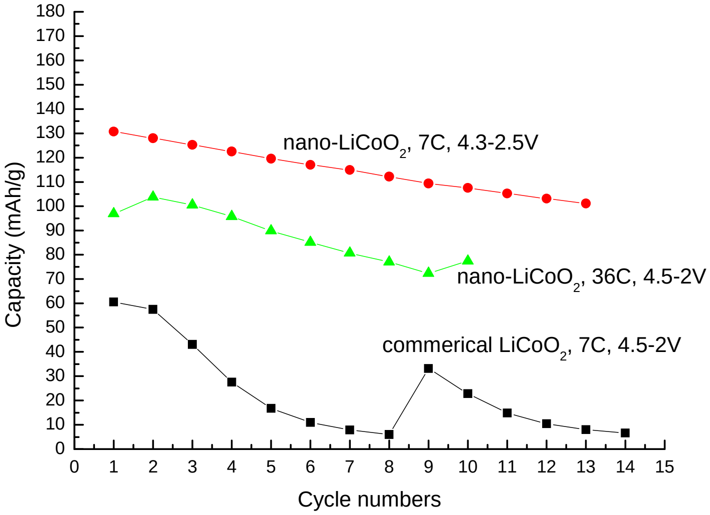

Figure 2.8. discharge capacity of nano-LiCoO$_2$ and commercial LiCoO$_2$ as function of cycle numbers. Cut off windows are: 4.3-2.5V for nano-LiCoO$_2$, 7C; 4.5V-2V for nano-LiCoO$_2$, 36C; 4.5V-2V for commercial LiCoO$_2$, 7C cycle 1-8; 5V-2V for commercial LiCoO$_2$, 7C, cycle 9-14.

between a voltage window of 4.2-2.5V (The practical capacity, 138 mAh/g, e.g. 50% of the theoretical capacity of $LiCoO_2$ is used to define the C-rate; nC=1/n hour charge or discharge). Although capacity fade is seen for continuous cycling (with no high voltage holding and no relaxation time between cycles), the retention is still good, at least at the first a few cycles. The rate performance of this $LiCoO_2$ sample is better than reported by Okubo et al.[4], where the used $LiCoO_2$ particle has an even smaller particle sizes (~17 nm) and, correspondingly, a much large surface area. This can be ascribed to the different morphology of our nano-$LiCoO_2$. In the work of Okubo et al., $LiCoO_2$ was synthesized from a CoOOH precursor and by ion-exchange under hydrothermal conditions. The particle morphology is most plate-like. But for our $LiCoO_2$, as shown in Fig. 2.5, the dominant morphology is rod/brick-like. As discussed in Chapter 1, a large active surface area of the cathode will facilitate the Li exchange between electrode and electrolyte. This morphology is presumably very good for the Li intercalation and deintercalation reactions, since large surface perpendicular to (003) planes are exposed. Capacity fade is observed both in Okubo el al.'s and our work. This is probably due to the side reactions of $LiCoO_2$, with electrolyte/organic solvents, which is not a significant problem for micrometer sized $LiCoO_2$ but is more pronounced for nanometer sized $LiCoO_2$.

Although as shown in Fig. 2.6, all $Li(Ni_{1/2}Mn_{1/2})O_2$ and $Li(Ni_{1/3}Co_{1/3}Mn_{1/3})O_2$ samples show XRD pattern of a single phase of a typical layered structure (R-3m), ^{6}Li NMR spectra show that the local structure of these samples are not homogenous. Fig. 2.9 shows the ^{6}Li MAS NMR of $Li(Ni_{1/2}Mn_{1/2})O_2$ and $Li(Ni_{1/3}Co_{1/3}Mn_{1/3})O_2$. They show

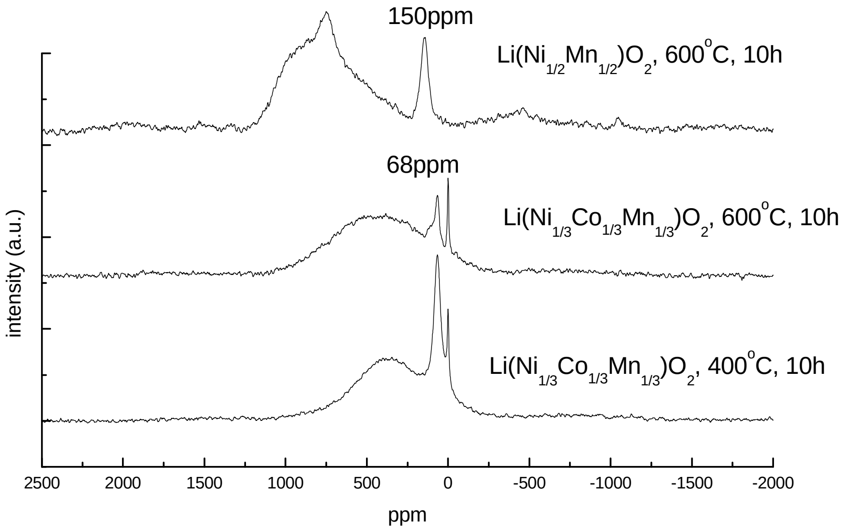

Figure 2.9. ^{6}Li MAS NMR of Li(Ni$_{1/2}$Mn$_{1/2}$)O$_2$ synthesized at 600°C, 10 hours and Li(Ni$_{1/3}$Co$_{1/3}$Mn$_{1/3}$)O$_2$ synthesized at 400°C and 600°C, 10 hours.

different resonances than that reported by Grey and coworkers for bulk $Li(Ni_{1/2}Mn_{1/2})O_2$ [28-32] and $Li(Ni_{1/3}Co_{1/3}Mn_{1/3})O_2$ [33-35]. For nano- $Li(Ni_{1/2}Mn_{1/2})O_2$, the broad resonance at around 750 ppm is assigned to the overlap of many resonances from Li in Li layers and the smaller resonances at about 1500 ppm are assigned to Li in transition metal layers and surrounded by 5 Mn and 1 Ni or 6 Mn based previous works by Grey and coworkers [31, 32]. The new resonance that was not seen in previous studies at 150 ppm is assigned to be Li in lithium layer in a layered $LiMnO_2$ (i.e. Mn^{3+}) like environment based on the work reported by Lee et al. [36-40] for $LiMnO_2$ and $LiMn_2O_4$ materials. For $Li(Ni_{1/3}Co_{1/3}Mn_{1/3})O_2$, beside the broad resonance at around 450 ppm representing Li in Li layers, which is consistent with that reported by Yoon et al [33-35] for micrometric $Li(Ni_{1/3}Co_{1/3}Mn_{1/3})O_2$, there are also a sharp resonance at 68 ppm and a weaker resonance at 0 ppm. The 68 ppm resonance is also similarly ascribed to the $LiMnO_2$-like environments based previous work by Lee et al.; while the 0 ppm resonance is ascribed to Li in diamagnetic $LiCoO_2$-like local environment since Co^{3+} is diamagnetic. These results imply a poor mixing of the transition metals at a local level in the transition metal layers, since for long range structure, no separate $LiCoO_2$ or $LiMnO_2$ phase is able to be distinguished by XRD. This also indicates the presence of Mn(III) and, correspondingly, as required by charge balance, Ni(III) in these nanometric $Li(Ni_{1/2}Mn_{1/2})O_2$ and $Li(Ni_{1/3}Co_{1/3}Mn_{1/3})O_2$ samples. This is different from those reported for bulk $Li(Ni_{1/2}Mn_{1/2})O_2$ and $Li(Ni_{1/3}Co_{1/3}Mn_{1/3})O_2$, in which Ni and Mn present as Ni(II) and Mn(IV) [41]. The presence of Mn(III) and Ni(III) is very likely due to the relatively low

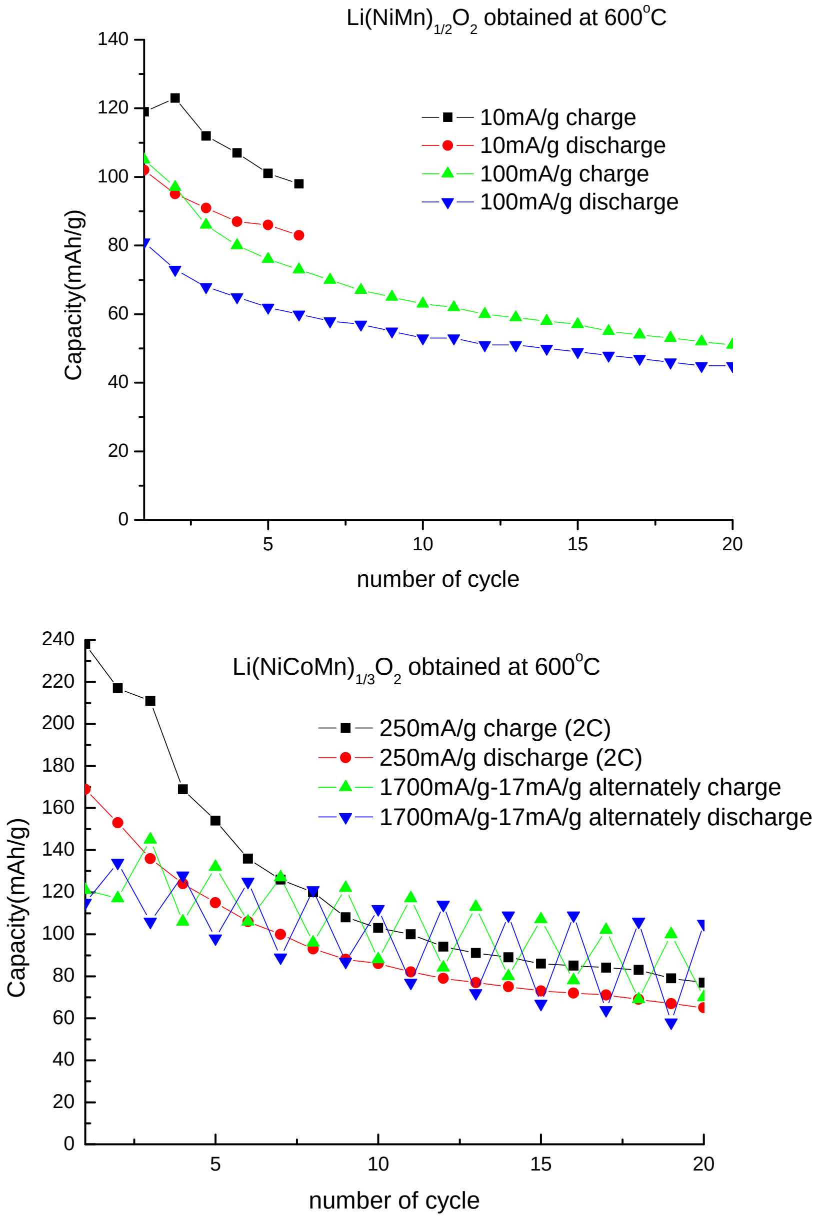

Figure 2.10. cycling capacity of (a) Li(Ni$_{1/2}$Mn$_{1/2}$)O$_2$ and (b) Li(Ni$_{1/3}$Co$_{1/3}$Mn$_{1/3}$)O$_2$ at various rates. The cycle windows are 4.3-2.5V. The procedure of an alternate cycling is: 1700mA charge and discharge→17mA charge and discharge→1700mA charge and discharge…and so on.

calcination temperatures. As a result, there may be less Ni-Mn clustering in these compounds. The ^{6}Li MAS NMR spectrum of a sample of $Li(Ni_{1/3}Co_{1/3}Mn_{1/3})O_2$ prepared at an even lower temperature, 400^{o}C, is shown in Fig.2.9c. Comparing it with the 600^{o}C sample, the resonances from $LiCoO_2$ and $LiMnO_2$ like environment are even more pronounced. These result implies that the reaction from mixed hydroxides precursors ($M(OH)_2$)to $LiMO_2$ is a complex process rather than a one-step oxidation reaction like what happens for $Co(OH)_2$ when oxidized to $LiCoO_2$. Phase segregations, caused by the thermal decomposition of the hydroxides, may occur and the corresponding oxides of the transition metals, such as NiO, Co_3O_4 and Mn_3O_4, may be formed as intermediate phases during the calcination. To have a random distribution of transition metals in the transition metal layers, high temperature calcination or annealing is needed. $Li(Ni_{1/2}Mn_{1/2})O_2$ showed a relative low capacity presumably due to the structural inhomogeneous discussed above. This also might be ascribed to the presence of some NiO impurity phase in the sample, whose characteristic XRD reflections largely overlap with the very broad $Li(Ni_xMn_y)O_2$ reflections and can not be readily distinguished. This impurity is present due to the incompletion of the reaction at low temperature. However, at high temperatures (above about 650^{o}C), normally $Li(Ni_{1/2}Mn_{1/2})O_2$ in nanometer size is not as stable as $LiCoO_2$ or $Li(Ni_{1/3}Co_{1/3}Mn_{1/3})O_2$. It tends to decompose, therefore forms NiO. The synthesis conditions for $Li(Ni_{1/2}Mn_{1/2})O_2$ by this method need further optimization. $Li(Ni_{1/3}Co_{1/3}Mn_{1/3})O_2$ shows good high rate capacities. As shown in Fig 2.10, it gives 165mAh/g discharge capacity at ~1C rate and 120 mAh/g capacity at ~5C in the cycling window of 2.5-4.3V. High-low rate alternately cycling capacity test shows that most of the capacity can be recovered by low rate cycling. The difference between $Li(Ni_{1/2}Mn_{1/2})O_2$ and $Li(Ni_{1/3}Co_{1/3}Mn_{1/3})O_2$ is that more Co can stabilize the layered structure and prevent the phase segregations of the mixed transition metal hydroxides upon heating. So that a perfect layered structure can be formed at relative low temperatures, therefore it gives better electrochemical performances. We believe that by further optimization of the synthetic conditions this nanometric $Li(Ni_{1/3}Co_{1/3}Mn_{1/3})O_2$ can be largely improved.

3.3. *In situ* XRD experiments

The phase evolution of $LiCoO_2$ upon charge has been reported by several groups and was largely consistent with each other, although different notations of the phases were used. Fig. 2.11 shows the phase diagram of Li_xCoO_2 upon charge reported by Ohzuku et al. [42]. Three phases with different lattice type are shown in the figure with the ranges in which they exist labeled by the black arrows. For clarity, the notations of the phases that we are going to use in this thesis work are also shown on top of this figure, where H stands for hexagonal phases, M stands for monoclinic phases and O3 and O1 indicate the stacking of the close packed O layers (ABCABC or ABABAB).

Amatucci et al. [43] firstly reported the full phase evolution of $LiCoO_2$ from the pristine phase to the end member, CoO_2, from their in situ XRD experiments as follows: H1 → H1+ H2→ H2→ M1 (at x~0.5 in Li_xCoO_2)→ H2→ M2→ M2 + H3→H3. Ohzuku

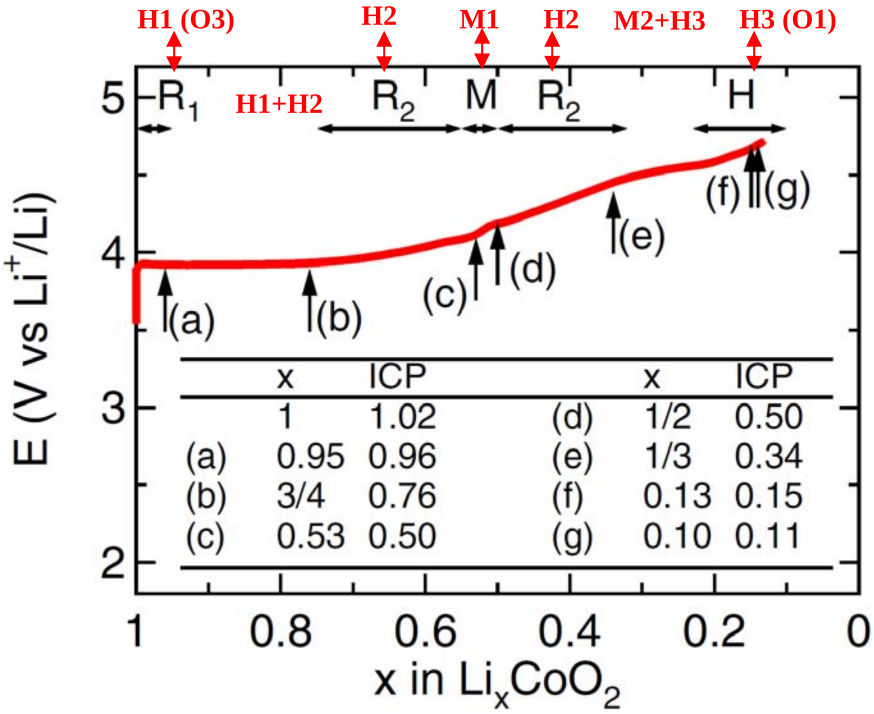

	x	ICP		x	ICP
	1	1.02	(d)	1/2	0.50
(a)	0.95	0.96	(e)	1/3	0.34
(b)	3/4	0.76	(f)	0.13	0.15
(c)	0.53	0.50	(g)	0.10	0.11

Figure 2.11 The phase diagram of Li_xCoO_2 as function of x and OCV (open circuit voltage) in the cell, reproduced from reference [42].

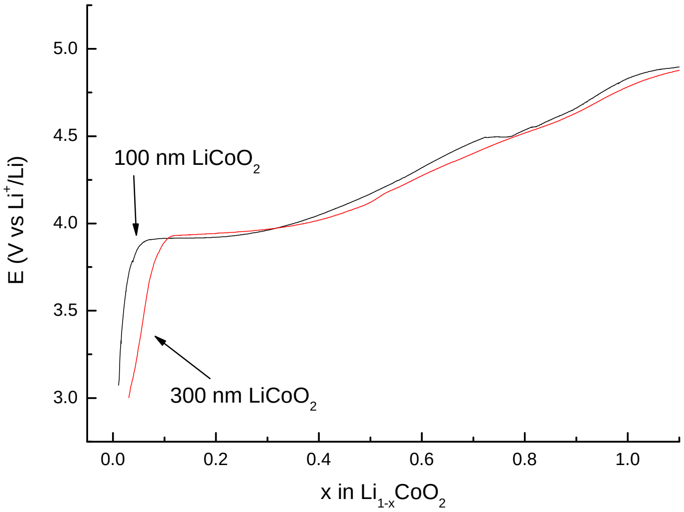

Figure 2.12. The charge curve of sample A (100 nm particle size) and B (300 nm particle size). The capacity beyond the theoretical capacity of $LiCoO_2$ is considered to be due to the decomposition of electrolyte at high voltages.

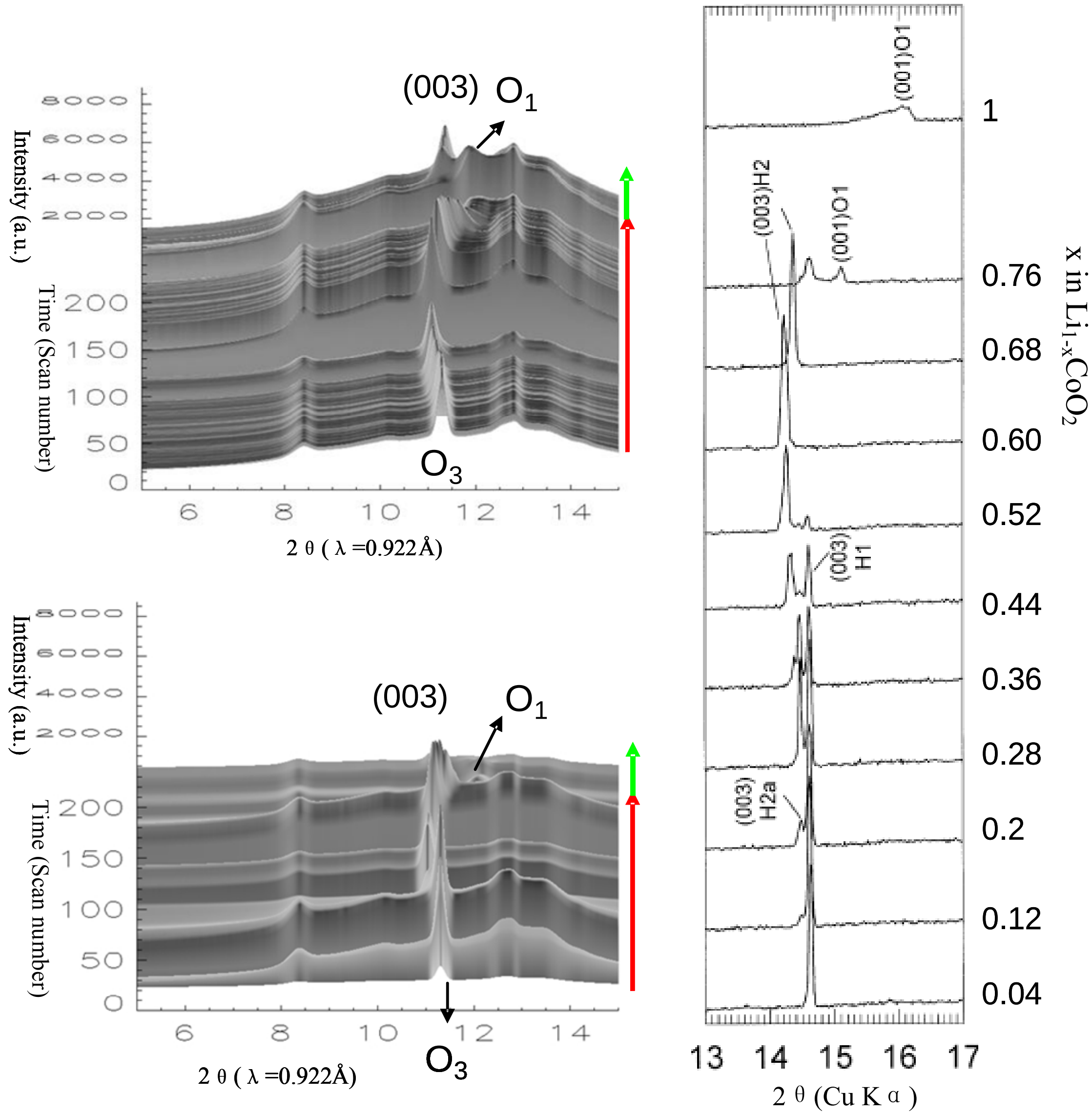

Figure 2.13. *In situ* XRD pattern of sample A (a) and B (b) at a 2θ range of 5-15^{o}. The red and green arrows indicate charge and discharge patterns respectively. The breaks of the patterns are due to the beam dumps. The cycling rate is C/20. Each scan takes 6 minutes. (c) is reproduced from reference [44]] by Yang et al.

et al. [45] reported a similar phase evolution route. Yang and McBreen reported another two intermediate phases H2a and O1a appearing in between the H1→H2 [44] transition and H2→O1 [46] transitions (M2 phase was not observed in this experiment). Ceder and Van der Ven et al. [47, 48] reported the phase evolution route for $0<x<0.4$ in Li_xCoO_2 suggested by first principle calculation: O3→O3+H1-3→H1-3→H1-3+O1, where H1-3 is an ordered phase adopting a ABABCACABCBC stacking sequence.

To study the possible particle size effect on the electrochemistry and phase evolution of the cathode materials, *in situ* XRD experiments were performed. Two samples were chosen to make the cathode film: sample A, $LiCoO_2$ prepared at 600^oC, 5 hours and annealed at 400^oC for 2 hours; and sample B, $LiCoO_2$ prepared at 600^oC, 5 hours and annealed at 800^oC for 10 minutes. The average particle size of sample A and B are about 100 and 300 nm respectively, based on the statistics from the TEM images. Fig 2.12 shows the charge curve of the two cells. The charge capacity was controlled to be a bit over the theoretical capacity of $LiCoO_2$ to compensate the capacity induced by decomposition of electrolyte at high voltages and to get as mush as possible Li extracted from $LiCoO_2$. Fig. 2.13 shows the in situ XRD patterns of sample A and B in 2θ range for 6-15° (wavelength used=0.922Å) , where the (003) reflection of the pristine $LiCoO_2$ hexagonal phase (O3) is located. The interruptions in the sequence of the patterns are due to beam dumps. The beam is unavailable at these times because the synchrotron ring needs to be refilled with electrons (usually every 12 hours). Fig. 2.12c shows the in situ XRD pattern of bulk $LiCoO_2$ on charge reported by Yang et al. [44] as a comparison. For the nanometric $LiCoO_2$ samples prepared here, both of their (003) reflections show first a gradually shift to lower 2θ and then to high 2θ, indicating an expansion and then a shrinking of the unit cell along *c* direction. No obvious peak splitting was observed, suggesting that the typical H1→H2 transitions and the two-phase region do not occur. To further clarify this question, FWHM of the (003) reflection and cell parameter *c* were measured/calculated from the patterns and plotted in Fig 2.14. For sample B, there is obvious peak broadening in the range of $0.2 < x < 0.45$. This is exactly where the H1→H2 phase transition usually occurs. This implies the existence of H1→H2 phase transition but because the broadening of the XRD peaks due to the small particle size and strong overlap of the H1(003) and H2(003) peaks, the peak splitting was not resolved. However for sample B, the one with smaller particle size, only a very small increase of FWHM was seen at around $x = 0.2$. This indicates a more solid-solution-like behavior for this sample. The small bump at $x = 0.2$ may reflect the presence of small amount of larger particles in the sample. As more Li is extracted, the hexagonal phase remained and no M1 or M2 phase was could be distinguished. At the region near the end of charge, the hexagonal phase O1 was observed in both samples. A dramatic FWHM increase observed for both samples. This is possibly due to the domain orientation disorder and stacking faults, which will be discussed in detail in next section. These results imply that the phase evolution route of $LiCoO_2$ is indeed size-dependent. The smaller the particle size, the larger the solid solution range and the less the two phase region. For $LiCoO_2$ with intermediate particle sizes, such as sample B, although the M1 and M2 phase were not

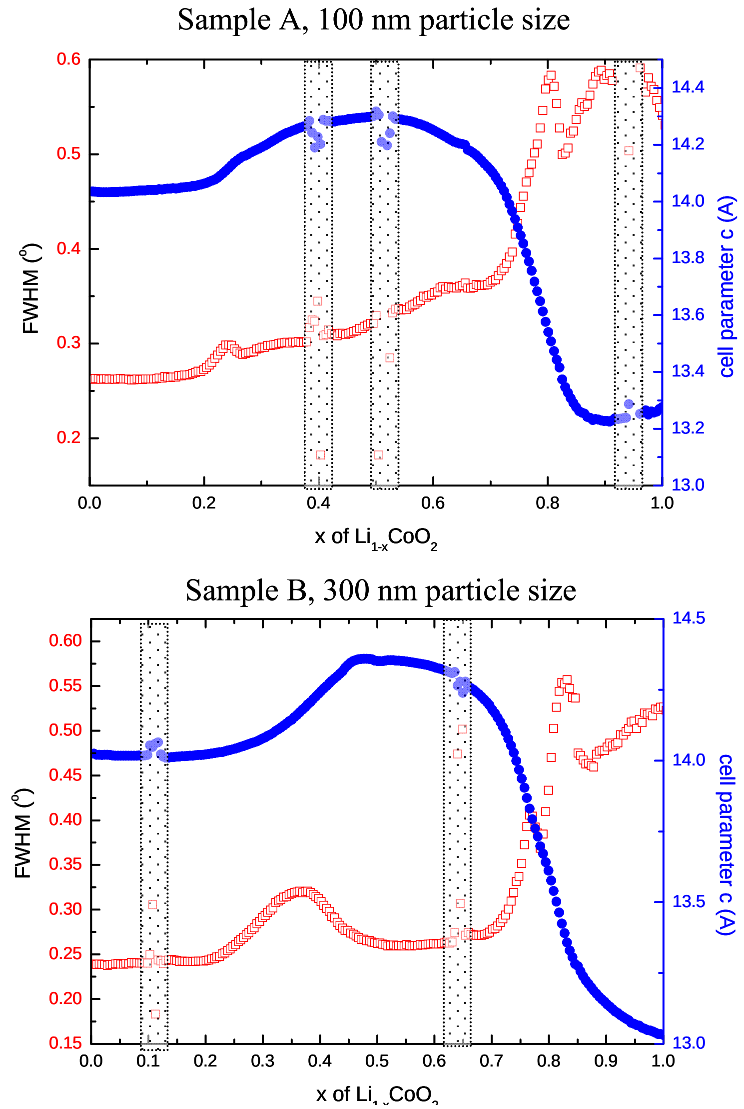

Sample A, 100 nm particle size

Sample B, 300 nm particle size

Figure 2.14 a FWHM of (003) peak and cell parameter *c* of sample A (top) and B (bottom). The blue solid circles represent c values; the red squares represent the FWHM. The shaded area corresponds to the time of beam dumps.

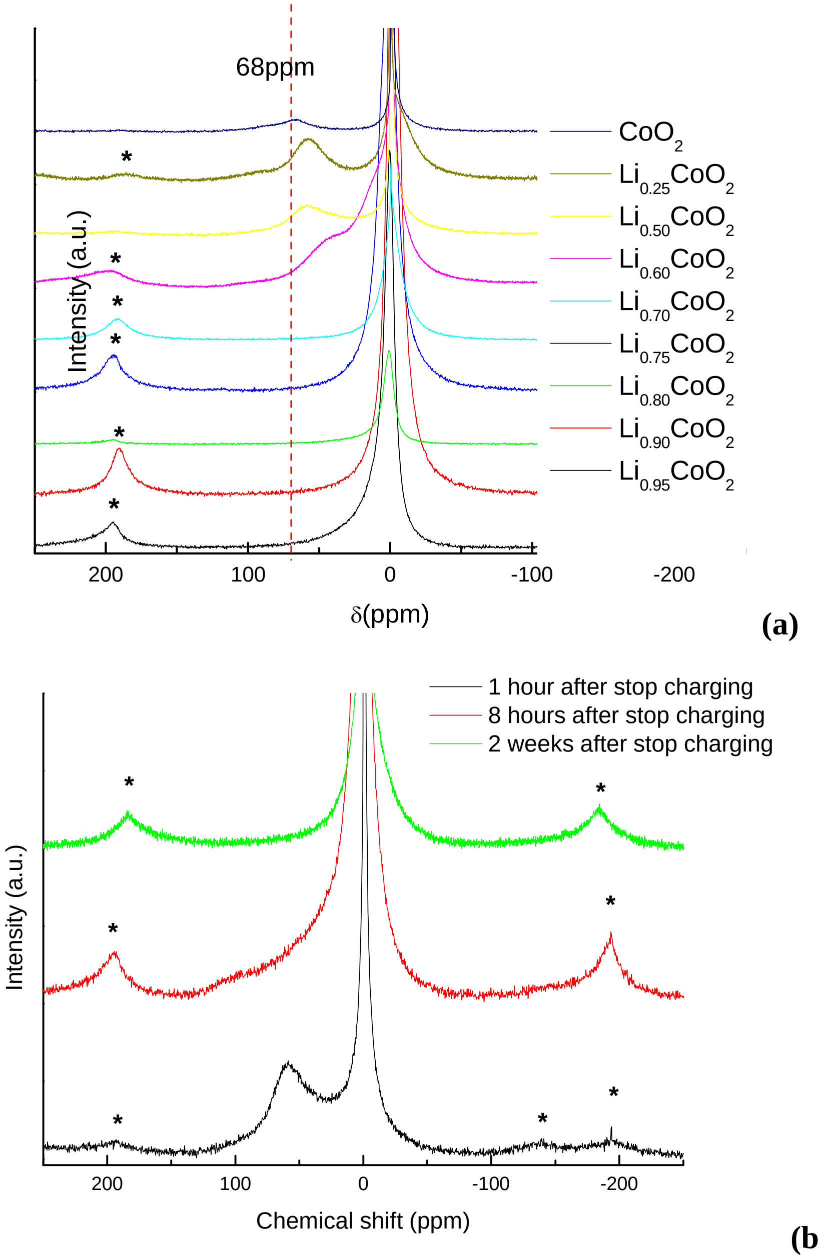

Figure 2.15. Ex situ ^{7}Li MAS NMR of charged LiCoO$_2$ nanoparticle. (a) Charged to different Li content; (b) Aged for different time after charged to Li$_{0.5}$CoO$_2$.

seen, the phase evolution mostly follows the route reported for bulk $LiCoO_2$, given that the ranges of M1 and M2 are very narrow and they are also sometime not seen for bulk $LiCoO_2$ [46]. The whole phase evolution for $LiCoO_2$ with a small particle size, such as sample A, is more solid-solution-like except for a short range of H1-O1 two phase region near the end of charge. This larger solid solution range of nanometric materials is also reported for other electrode materials such as $Li_4Ti_5O_{12}$ [49] and $LiFePO_4$ [50], suggesting that this phenomena maybe common for many cathode materials.

3.4. NMR experiments

Pristine and charged nano-$LiCoO_2$ were also studied by using *ex situ* ^{7}Li MAS and *in situ* static NMR. Fig 2.15a shows the spectra of *ex situ* ^{7}Li NMR of $LiCoO_2$ nanoparticles (synthesized at 500°C, 10 hours) charged to different SOD (State of Charge). Interestingly, the spectra of the charged samples are different from that reported by Menetrier et al. [8] for bulk HT-$LiCoO_2$, especially for the appearance of the "Knight shifted" peak. A "Knight shifted" resonance is an indicator of metallic behavior, implies in this system that an insulator to metal transition has occurred. For bulk Li_xCoO_2, it first shows up at $x = 0.94$ to 0.99 (the exact value depending on the stoichiometry of the sample [7]), and is associated with the H1→H2 phase transition. Then in the following two phase region, the 0 ppm diamagnetic resonance and the 60 ppm Knight-shifted resonance coexist. After $x = 0.6$, only the Knight shifted resonance is seen and this resonance gradually shifts to 100 ppm as more Li is deintercalated. However, for nano-$LiCoO_2$, the knight shift resonance was not seen until x = 0.6. One possible explanation for this inconsistency is the fast relaxation and self-discharge of the battery, so that the sample studied in the *ex situ* NMR experiment is reduced by reaction with the electrolyte before the NMR experiment can be performed. To prove this, a series of aging experiments were performed: 3 cells using nano-$LiCoO_2$ as cathodes were charged to x=0.5 with same current rate, and put into the glove box immediately after the charging was stopped. The powder were packed in the rotors after: A, no aging time, B, 8 hours of aging after the cell is disassembled, C, 2 weeks of aging after the cell is disassembled. Fig. 2.11b shows the ^{7}Li spectra of these samples. Sample A shows a Knight Shift peak at around 60 ppm and a relatively sharp resonance at 0 ppm, due to the existence of the diamagnetic species such as dry electrolyte and SEI. As the aging time increases, the Knight Shift peak gradually shifts towards 0 ppm and the 0 ppm resonance become broader, which indicates the possible presence of Li_xCoO_2 (x~1). The fact that the Knight-shifted peak is clearly present in the non-aged x = 0.5 sample but disappears after aging implies that the metal insulator transition might not be delayed in nano-$LiCoO_2$ system, and that the late appear of the Knight-shifted peak in Fig. 2.11a may be due to the side reaction of nano-$LiCoO_2$ and electrolyte, which result in some Li inserted back into the structure, e.g. the self-discharge behavior of nano-$LiCoO_2$. This is further proved by *in situ* static ^{7}Li NMR. The Knight-shifted peak appears at the very beginning of the charge in the *in situ* experiments. The detail of the results will be discussed in Chapter 5.

The self-discharge effect is closely related to the surface area of $LiCoO_2$ and it is not obvious for bulk $LiCoO_2$. In fact, recent study by Menetrier et al. [7] showed that for very stoichiometric bulk $LiCoO_2$, the insulator-metal transition also happens at the very beginning of the charge. The reason why it was observed before at $x = 0.94$ is because of both the off-stoichiometry of the sample and very slight self-discharge of bulk $LiCoO_2$. This self-discharge effect is obviously a drawback for the application of nanometric cathode materials in LIBs, but many studies have showed that the side reactions between the cathode materials and the electrolytes can be largely retarded by surface coating or modification, so it maybe possible to improve the cyclability of the nanometric cathode materials by surface modification or coating. An example of improving the cycling performance of $LiCoO_2$ by AlF_3 coating will be discussed in Chapter 3.

3.4. HRTEM experiments

Nano-$LiCoO_2$ samples charged to different capacities were studied by HRTEM and electron diffraction. As discussed before, due to the self-discharge of the battery, especially the self-discharge at high voltages, even the “fully” charged (charged to 5.3V and the charge capacity is controlled to be larger than the theoretical capacity of $LiCoO_2$) $LiCoO_2$ does not show a single O1 phase (CoO_2), instead, shows a mixture of O3 (Li_xCoO_2, $x < 0.2$) and O1 phase, sometimes even in one particle. Fig. 2.16a shows a HRTEM image of a particle of a “fully” charged $LiCoO_2$ sample. In comparison to the image of the pristine sample shown in Fig. 2.5d, a large numbers of defects were seen,

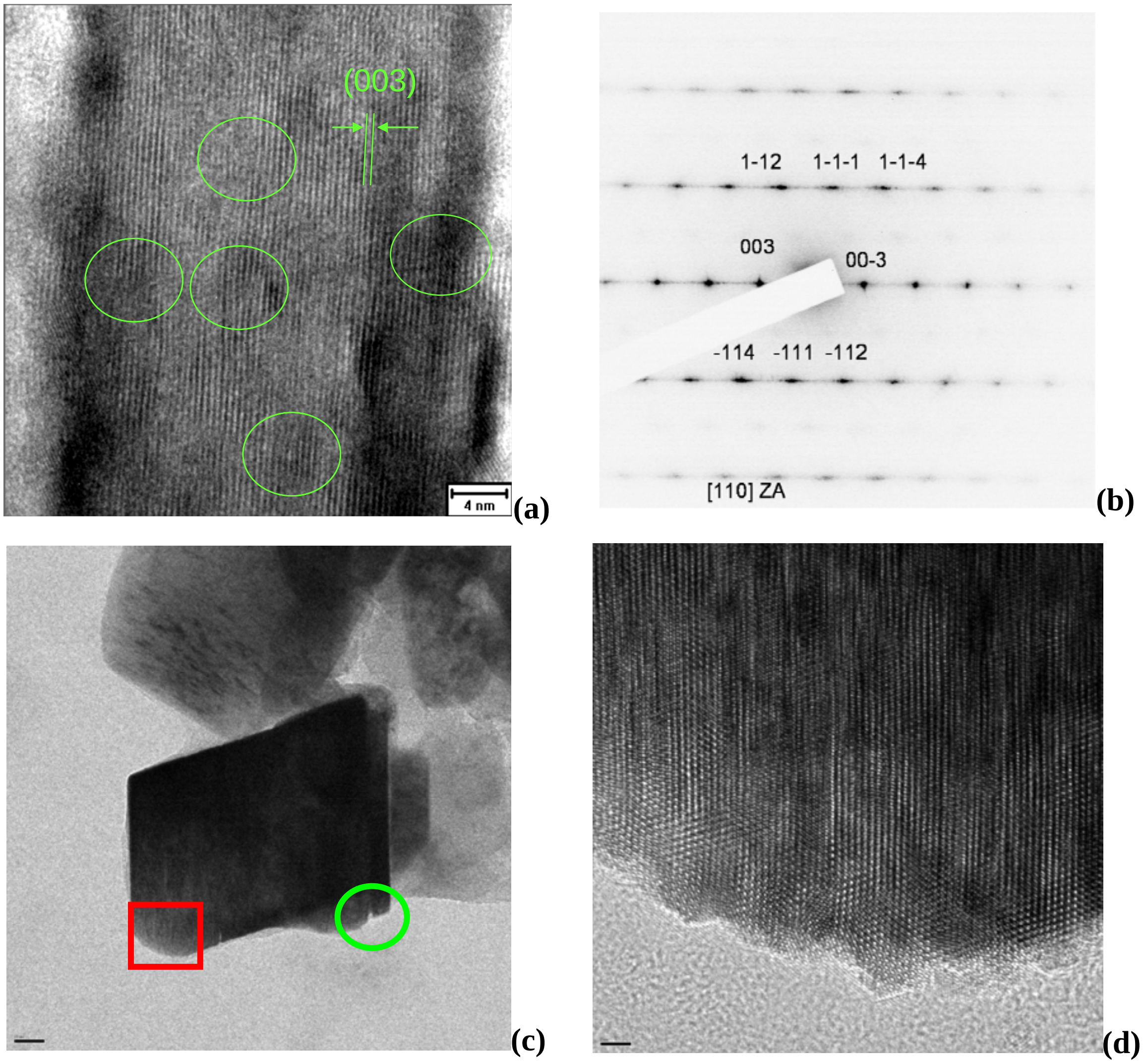

Figure 2.16. (a) HRTEM image of a fully charged $LiCoO_2$ particle. The green circles indicate dislocations; (b) the diffraction pattern of fully charged $LiCoO_2$ particle, indexed with [110] zone axis of a O3 structure; (c) the low magnification image of the particle and (d). The high resolution image of the particle on the square area indicated in (c). Scale bar in (d) is 2 nm.

such as the edge dislocations indicated by the circles. Fig .2.16c and b shows the low magnification image and the electron diffraction pattern of another particle along the zone axis [110]. Two small cracks are seen on the edge, which are probably due to the lattice distortion caused by charging. Fig. 2.16d shows the high resolution image of the area circled in Fig. 2.16c, where a nanodomain-like feature is seen: The *d*-spacing of the planes ((003) of O3 or (001) of O1) varies for each domain, from 4.2 ~ 4.4 Å, and in the domain boundaries, the lattice is obviously distorted. Some edge dislocations are also seen in this area.

These defects and distortions are ascribed to the structural changes of Li_xCoO_2 from O3 to O1 stacking, e.g. from a ABCABCAB stacking sequence to ABABABAB (or BCBCBCBC, or CACACACA) stacking sequence of the Co-O octahedrons. Ideally, this change requires shearing of four layers in every six layers as a repeating unit. Delmas and coworkers [51] showed that when $LiCoO_2$ with O2 stacking, which is thermodynamically unstable and can only be synthesized by using ion-exchange method, is heated at high temperatures so that it carries out a O2-O3 transition, shearing of the whole particle and the appearance the steps on the surface of the particle is seen. This is an example of accommodating the stacking changes by shearing the whole layers across a particle. However, under room temperature and during electrochemical cycling, this kind of shearing of whole particle is not likely to happen. The shearing of the layers is rather possibly to happen in smaller ranges, e.g. in nanodomains. Ceder et al. [47, 48] proposed a so-called H1-3 stacking as an intermediate stacking between O3 and O1, where the sequence is ABABCACABCBC. In this model, in one unit cell, which is 4 times larger than the original O3 unit cell along c axis, there are 12 Co-O layers. In one unit cell of this model, two ABC stacking units are maintained to minimize its structure and energy difference from the original O3 structure. However, to turn the O3 structure to this structure, 8 out of total 12 layers still need to be translated or sheared. In fact, for any transformation from O3 to O1, for example, from ABCABC to ABABAB or BCBCBC or CACACA or other larger repeating units, 4/6 of the layers always need to be translated and sheared. From an energy point of view, there are many degenerated configurations of stacking sequence as the intermediate phase between O3 and O1. For the (110) surface as shown in Fig 2.16, since Li can be extracted from any part of the surface simultaneously, and Li can not diffuse through the (003) planes, e.g. through the Co-O octahedrons, each small domain on the (110) surface can take different pathways to carry out the O3→O1 transition independently. For example, in one domain, the stacking sequence can be ABABAB with its neighboring domain being BCBCBC or ACACAC, or it can remain as O3 stacking. This will lead to mismatches of the domain boundaries. Fig 2.17 shows the schematics of transformation from O3 to O1 and the relaxation of the lattice on the domain boundaries to minimize the distortion. When a repeating unit of ABCABC (O3) turns to ABABAB (O1) while its neighbor unit remains ABCABC, the first two layers remain the same, but rest four layers need to translate their O atoms from the original places to carry out the stacking change. Fig 2.17a and b shows the translation of O atoms on the *ab* planes. In the figure, the O atoms in the O3 domain take A positions. In the

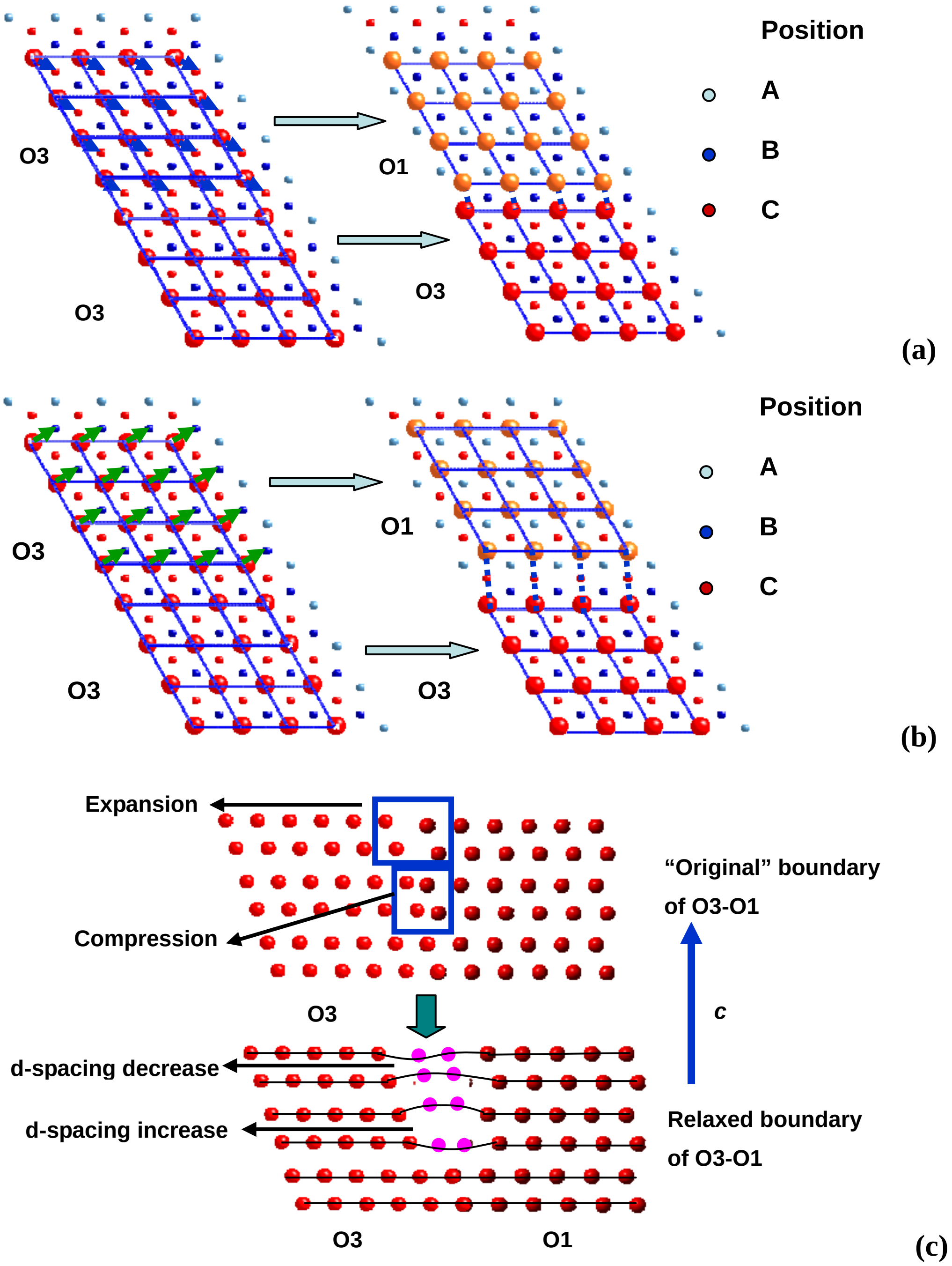

Figure 2.17. Schematics of a model of relaxation and defects on O3-O1 domain boundary. (a) On the *ab* plane, O atoms translate from A to C positions, resulting in compression on domain boundary; (b) On the *ab* plane, O atoms translate from A to B positions, resulting in expansion on domain boundary; (c) View on (110) plane, the O atoms on the boundary are moved off the *ab* planes to relax the strain. Expansion shown in the top two rows correspond to the ab plane translation shown in (b); Compression shown in the middle two rows correspond to the *ab* plane translation shown in (a).

domain on top of it, the O atoms can be translated to either B position (Fig. 2.17 b) or C (Fig. 2.17a) positions to form O1 stacking. These two kinds of translation result in compression (a) and expansion (b) of the lattice in the boundary respectively. To relax the compression, one possible scenario is to push the O atoms on the boundary a bit off the *ab* plane, like shown in the middle rows in Fig. 2.17c. Thus the "local" *d*-spacing of (003) plane is increased. Here we define this type of defect as a "-" defect. Similarly, in the case of lattice expansion is formed, the relaxation of the O atoms on the domain boundary will cause the decrease of *d*-spacing of (003) plane. It is defined as a "+" defect. For simplicity, in the schematics only 4 O atoms, e.g. two Co-O octahedra near the boundary for each layer are shown with distortion, but in real case, the relaxation can happen through several octahedra with slighter distortion for each octahedron. This kind of lattice mismatch and relaxation appear not only between O3 and O1 domain, but also appear between the O1 domains with different stacking sequences. For example, this can between an O1 domain with ABABAB stacking and another O1 domain with ACACAC stacking. This model may explain the random variation of the d-spacing of (003) plane shown in Fig. 2.16a and d.

As more Li is extracted, the O1 domains grow and the O3 domains vanish. Also, Li diffusion over the domain boundaries can cause the movement of the boundary and the defects. These "+" and "-" defects can move and may meet at some point. The distortions can accumulate and, in some extreme cases, when the accumulated distortion is too large to be accommodated by local *d*-spacing change, the layers can be broken to release the strain. Thus an edge dislocation, as shown in Fig.2.16a is formed. The other possible route is that the defects move to the surface and accumulate to form microcracks, as the ones shown by the circle in Fig. 2.16b.

The experiments on the discharged $LiCoO_2$ samples showed that most of the defects disappear as Li is inserted back to the lattice, but there still some defects, dislocations remaining. The cracks, of course, are not reversible either. As the number of cycles increase, the microcracks on the edge of the particles can grow towards middle of the particle and eventually break the particle in pieces. The cracking of the particle can result in the particle being isolated from the conductive carbon and the increasing dislocations can block the Li diffusion in the 2-D channels. For long term, this could be one of the most important origins of the battery fail for the LIBs using $LiCoO_2$ as cathode materials, when cycled to high voltages.

4. CONCLUSIONS AND IMPLICATIONS

In this work we developed a new synthetic method for lithium transition metal oxides, the co-precipitation in non-aqueous systems. By using this method, nanoparticle of $LiCoO_2$, $Li(Ni_{1/2}Mn_{1/2})O_2$ and $Li(Ni_{1/3}Co_{1/3}Mn_{1/3})O_2$ with uncommon morphology were obtained. $LiCoO_2$ and $Li(Ni_{1/3}Co_{1/3}Mn_{1/3})O_2$ nanoparticles showed excellent rate performances when used as cathodes for LIBs. Although in situ XRD and ex situ NMR experiments revealed that the self-discharge and the increased side reactions for these nanoparticles would be problematic for their application in batteries, they are still promising cathode materials for high rate LIBs since the self-discharge and side reactions are possibly to be overcome or largely retarded by optimization of heat treatment and surface modifications [52-56]. The O3-O1 phase transition is shown to be one of the reasons that cause the capacity loss of $LiCoO_2$ when charged to high voltages. This may be also true for other layered compounds, such as $Li(Ni_{0.5}Mn_{0.5})O_2$ and $Li(Ni_{1/3}Co_{1/3}Mn_{1/3})O_2$, that have O3-O1 phase transition. Therefore it is important to limit the state of charge of these compounds in the O3 range during cycling to improve the capacity retention.

REFERENCES

1. Ohzuku, T.; Makimura, Y., *Chem. Lett.* **2001**, (7), 642-643.
2. Chen, H. L.; Qiu, X. P.; Zhu, W. T.; Hagenmuller, P., *Electrochem. Commun.* **2002,** 4, (6), 488-491.
3. Thurston, T. R.; Jisrawi, N. M.; Mukerjee, S.; Yang, X. Q.; McBreen, J.; Daroux, M. L.; Xing, X. K., *Appl. Phys. Lett.* **1996,** 69, (2), 194-196.
4. Okubo, M.; Hosono, E.; Kim, J.; Enomoto, M.; Kojima, N.; Kudo, T.; Zhou, H. S.; Honma, I., *J. Am. Chem. Soc.* **2007,** 129, (23), 7444-7452.
5. Levasseur, S.; Menetrier, M.; Delmas, C., *Chem. Mater.* **2002,** 14, (8), 3584-3590.
6. Levasseur, S.; Menetrier, M.; Suard, E.; Delmas, C., *Solid State Ionics* **2000,** 128, (1-4), 11-24.
7. Menetrier, M.; Carlier, D.; Blangero, M.; Delmas, C., *Electrochem. Solid State Lett.* **2008,** 11, (11), A179-A182.
8. Menetrier, M.; Saadoune, I.; Levasseur, S.; Delmas, C., *J. Mater. Chem.* **1999,** 9, (5), 1135-1140.
9. Menetrier, M.; Shao-Horn, Y.; Wattiaux, A.; Fournes, L.; Delmas, C., *Chem. Mater.* **2005,** 17, (18), 4653-4659.
10. Amatucci, G. G.; Tarascon, J. M.; Larcher, D.; Klein, L. C., *Solid State Ionics* **1996,** 84, (3-4), 169-180.
11. Larcher, D.; Palacin, M. R.; Amatucci, G. G.; Tarascon, J. M., *J. Electrochem. Soc.*

1997, 144, (2), 408-417.

12. Aurbach, D.; Markovsky, B.; Rodkin, A.; Cojocaru, M.; Levi, E.; Kim, H. J., *Electrochim. Acta* **2002,** 47, (12), 1899-1911.

13. Wang, Z. X.; Liu, L. J.; Chen, L. Q.; Huang, X. J., *Solid State Ionics* **2002**, 148, 335-342.

14. Casas-Cabanas, M.; Rodriguez-Carvajal, J.; Canales-Vazquez, J.; Palacin, M. R., *J. Mater. Chem.* **2006,** 16, (28), 2925-2939.

15. Du, K.; Yang, Y. N.; Hu, G. R.; Peng, Z. D.; Qi, L., *Chin. J. Inorg. Chem.* **2008,** 24, (4), 615-620.

16. Chang, Z. R.; Chen, Z. J.; Wu, F.; Tang, H. W.; Zhu, Z. H., *Acta Phys.-Chim. Sin.* **2008,** 24, (3), 513-519.

17. Reddy, M. V.; Rao, G. V. S.; Chowdari, B. V. R., *J. Phys. Chem. C* **2007,** 111, (31), 11712-11720.

18. Ni, J. F.; Zhou, H. H.; Chen, J. T.; Zhang, X. X., *Mater. Lett.* **2007,** 61, (4-5), 1260-1264.

19. Reddy, M. V.; Rao, G. V. S.; Chowdari, B. V. R., *J. Power Sources* **2006,** 159, (1), 263-267.

20. Wen, L.; Lu, Q.; Xu, G. X., *Electrochim. Acta* **2005,** 51, (21), 4388-4392.

21. Du, K.; Qi, L.; Hu, G. R.; Peng, Z. D., *Chin. J. Inorg. Chem.* **2006,** 22, (5), 867-871.

22. Tan, K. S.; Reddy, M. V.; Rao, G. V. S.; Chowdari, B., *J. Power Sources* **2005,** 147,

(1-2), 241-248.

23. Kim, J. H.; Myung, S. T.; Sun, Y. K., *Electrochim. Acta* **2004,** 49, (2), 219-227.

24. Han, C. H.; Hong, Y. S.; Kim, K., *Solid State Ionics* **2003,** 159, (3-4), 241-247.

25. Han, C. H.; Hong, Y. S.; Park, C. M.; Kim, K., *J. Power Sources* **2001,** 92, (1-2), 95-101.

26. Liang, H. Y.; Qiu, X. P.; Chen, H. L.; He, Z. Q.; Zhu, W. T.; Chen, L. Q., *Electrochem. Commun.* **2004,** 6, (8), 789-794.

27. Liang, H. Y.; Qiu, X. P.; Zhang, S. C.; He, Z. Q.; Zhu, W. T.; Chen, L. Q., *Electrochem. Commun.* **2004,** 6, (5), 505-509.

28. Breger, J.; Meng, Y. S.; Hinuma, Y.; Kumar, S.; Kang, K.; Shao-Horn, Y.; Ceder, G.; Grey, C. P., *Chem. Mater.* **2006,** 18, (20), 4768-4781.

29. Breger, J.; Dupre, N.; Chupas, P. J.; Lee, P. L.; Proffen, T.; Parise, J. B.; Grey, C. P., *J. Am. Chem. Soc.* **2005,** 127, (20), 7529-7537.

30. Meng, Y. S.; Ceder, G.; Grey, C. P.; Yoon, W. S.; Shao-Horn, Y., *Electrochem. Solid State Lett.* **2004,** 7, (6), A155-A158.

31. Yoon, W. S.; Grey, C. P.; Balasubramanian, M.; Yang, X. Q.; McBreen, J., *Chem. Mater.* **2003,** 15, (16), 3161-3169.

32. Yoon, W. S.; Paik, Y.; Yang, X. Q.; Balasubramanian, M.; McBreen, J.; Grey, C. P., *Electrochem. Solid State Lett.* **2002,** 5, (11), A263-A266.

33. Chemova, N. A.; Ma, M.; Xiao, J.; Whittingham, M. S.; Breger, J.; Grey, C. P., *Chem. Mater.* **2007,** 19, (19), 4682-4693.

34. Yoon, W. S.; Balasubramanian, M.; Chung, K. Y.; Yang, X. Q.; McBreen, J.; Grey, C. P.; Fischer, D. A., *J. Am. Chem. Soc.* **2005,** 127, (49), 17479-17487.

35. Yoon, W. S.; Grey, C. P.; Balasubramanian, M.; Yang, X. Q.; Fischer, D. A.; McBreen, J., *Electrochem. Solid State Lett.* **2004,** 7, (3), A53-A55.

36. Lee, Y. J.; Grey, C. P., *J. Electrochem. Soc.* **2002,** 149, (2), A103-A114.

37. Lee, Y. J.; Park, S. H.; Eng, C.; Parise, J. B.; Grey, C. P., *Chem. Mater.* **2002,** 14, (1), 194-205.

38. Lee, Y. J.; Grey, C. P., *Chem. Mater.* **2000,** 12, (12), 3871-3878.

39. Lee, Y. J.; Wang, F.; Mukerjee, S.; McBreen, J.; Grey, C. P., *J. Electrochem. Soc.* **2000,** 147, (3), 803-812.

40. Lee, Y. J.; Wang, F.; Grey, C. P., *J. Am. Chem. Soc.* **1998,** 120, (48), 12601-12613.

41. Zeng, D. L.; Cabana, J.; Breger, J. L.; Yoon, W. S.; Grey, C. P., *Chem. Mater.* **2007,** 19, (25), 6277-6289.

42. Mukai, K.; Ikedo, Y.; Nozaki, H.; Sugiyama, J.; Nishiyama, K.; Andreica, D.; Amato, A.; Russo, P. L.; Ansaldo, E. J.; Brewer, J. H.; Chow, K. H.; Ariyoshi, K.; Ohzuku, T., *Phys. Rev. Lett.* **2007,** 99, (8).

43. Amatucci, G. G.; Tarascon, J. M.; Klein, L. C., *J. Electrochem. Soc.* **1996,** 143, (3), 1114-1123.

44. Yang, X. Q.; Sun, X.; McBreen, J., *Electrochem. Commun.* **2000,** 2, (2), 100-103.

45. Ohzuku, T.; Ueda, A.; Yamamoto, N., *J. Electrochem. Soc.* **1995,** 142, (5), 1431-1435.

46. Sun, X.; Yang, X. Q.; McBreen, J.; Gao, Y.; Yakovleva, M. V.; Xing, X. K.; Daroux, M. L., *J. Power Sources* **2001,** 97-8, 274-276.

47. Van der Ven, A.; Aydinol, M. K.; Ceder, G.; Kresse, G.; Hafner, J., *Phys. Rev. B* **1998,** 58, (6), 2975-2987.

48. Van der Ven, A.; Aydinol, M. K.; Ceder, G., *J. Electrochem. Soc.* **1998,** 145, (6), 2149-2155.

49. Kavan, L.; Prochazka, J.; Spitler, T. M.; Kalbac, M.; Zukalova, M. T.; Drezen, T.; Gratzel, M., *J. Electrochem. Soc.* **2003,** 150, (7), A1000-A1007.

50. Gibot, P.; Casas-Cabanas, M.; Laffont, L.; Levasseur, S.; Carlach, P.; Hamelet, S.; Tarascon, J. M.; Masquelier, C., *Nat. Mater.* **2008,** 7, (9), 741-747.

51. Carlier, D.; Saadoune, I.; Croguennec, L.; Menetrier, M.; Suard, E.; Delmas, C., *Solid State Ionics* **2001,** 144, (3-4), 263-276.

52. Pereira, N.; Al-Sharab, J. F.; Cosandey, F.; Badway, F.; Amatucci, G. G., *J. Electrochem. Soc.* **2008,** 155, (11), A831-A838.

53. Sun, Y. K.; Cho, S. W.; Lee, S. W.; Yoon, C. S.; Amine, K., *J. Electrochem. Soc.* **2007,** 154, (3), A168-A172.

54. Sun, Y. K.; Han, J. M.; Myung, S. T.; Lee, S. W.; Amine, K., *Electrochem. Commun.* **2006,** 8, (5), 821-826.

55. Woo, S. U.; Yoon, C. S.; Amine, K.; Belharouak, I.; Sun, Y. K., *J. Electrochem. Soc.* **2007,** 154, (11), A1005-A1009.

56. Park, B. C.; Kim, H. B.; Myung, S. T.; Amine, K.; Belharouak, I.; Lee, S. M.; Sun,

Y. K. *J. Power Sources* **2008**, 178, 826-831.

CHAPTER 3

Molten Salt Synthesis and High Rate Performance of the “Desert-Rose” Form of $LiCoO_2$

Hailong Chen, Clare P. Grey

Department of Chemistry, Stony Brook University, Stony Brook, NY 11794-3400

Adv. Mater. **2008**, 20 (11), 2206-2211

ABSTRACT

A novel nanostructure of $LiCoO_2$, so called a “desert rose” structure, which resembles the morphology of natural minerals such as Gypsum, is synthesized by a new synthetic method, the low temperature molten salt method. The reactions in the molt flux are monitored by *ex situ* XRD and electron microscopy. A dissolution-reprecipitation mechanism is proposed to explain the formation of this unusual morphology. Lithium ion battery using this $LiCoO_2$ material as cathode shows excellent rate performances.

1. INTRODUCTION

Lithium ion batteries (LIBs) represent the most popular rechargeable batteries for use in portable electronic devices such as cell phones and laptops, due to their long cycle life and high capacity. However, their relatively low charge/discharge rates and safety concerns have limited their use in applications that require both high power and high capacity, such as Electric and Hybrid Electric Vehicles. Rate limitations result from a number of factors including low ionic (Li^+) and electronic conductivity of the electrode materials and slow insertion/extraction of Li^+ into the cathode, at the cathode-electrolyte interface. Here we report the synthesis of a new lithium transition metal oxide nanostructure for the cathode material $LiCoO_2$, by using a molten salts/hydroxides flux method. Although high temperature (700–900 °C) molten salt syntheses have previously been used to synthesize LIB cathodes [1-13], a much lower temperature flux system was used here, resulting in a nanostructure with good electrochemical performance at high rates.

Recent studies of layered cathode materials have shown that both the charge on the transition metal layers and the interlayer spacing are important in reducing the activation energies for Li^+ ion diffusion, resulting in high rate performances [14-17]. A second approach to high rates involves the synthesis of materials with larger cathode-electrolyte interfaces, for example, via the synthesis of nanoparticles, nanowires, thin films, and porous structures [18-22]. This approach is not always straightforward for oxides, and is often associated with high costs: Generally, high temperatures are required to achieve phase purity and good crystallinity, while the synthesis of nanostructures and porous structures is typically achieved at much lower temperatures. Furthermore, both the stoichiometry and local structure must be carefully controlled to optimize electrochemical performance. For example, $LiCoO_2$, the most popular cathode material for lower-power LIBs, is usually made by solid state reaction at 800–1000°C. Attempts to synthesize this material at low temperatures via hydrothermal methods generally result in the growth of particles larger than several micrometers [23, 24]. Thus, until now, there are very few reports of LIB systems that show good capacity retention at high rates [15, 21, 25]. Here we use a molten hydroxide mixed alkali metal salt flux as the reaction solvent, the much larger viscosity and dielectric of the eutectic system resulting in particles that are much finer than those prepared by solid state reactions [26, 27].

2. EXPERIMENTAL

A representative procedure used to prepare the “desert rose” $LiCoO_2$ is as follows. $CsOH.H_2O$ (2 g), KOH (6 g), LiOH (1 g), and $Co(NO_3)_2$ (0.58 g) were put in a Teflon container and heated up to 200^oC either statically in a muffle furnace or in a oil bath with vigorous stirring for 5 minutes to 48 hours. After cooling in air, the dark black products were separated from the eutectic mixture by washing with large mount of deionized water and filtration. The product was dried at 80^oC overnight. The commercial sample of $LiCoO_2$ was obtained from Sigma/Aldrich. The XRD patterns of the samples were acquired with a bench-top X-ray diffractometer (Rigaku MiniFlex) and by using synchrotron radiation X-Ray diffraction at the Beamline X7B at the National Synchrotron Light Source (NSLS) located at Brookhaven National Laboratory (BNL). Cell parameters of $a = b = 2.8182$, and $c = 14.0821$ Å, ($W_{Rp} = 2.21\%$) were obtained by Rietveld refinement, which are slightly larger than those reported for micrometer-sized $LiCoO_2$, (typically $a = b = 2.812–2.816$ and $c = 14.03–14.06$ Å), but consistent with cell parameters reported previously for $LiCoO_2$ nanoparticles [25]. SEM and TEM were performed by using LEO-1550 field-emission and JOEL–4000 high resolution microscopes, respectively. TEM was use to obtain the 2-D lattice image and single crystal electron diffraction patterns of the samples. EDAX measurements showed only peaks due to Co and O; Li is not observable with our detector window on the SEM. Electrochemical experiments were performed with $LiCoO_2$ samples mixed with poly-vinylidene fluoride binder and acetylene black (6:1:3 wt %) in N-methyl pyrrolidone (NMP) to make a thick slurry. The slurry was deposited on an aluminum foil by the doctor-blade method and dried at 80°C overnight. Coin cells (CR2032, Hohsen Corp.) were assembled in an argon-filled glove box. Each cell typically contained 6–8 mg of active material, separated from the Li foil anode by a piece of Celgard separator (Celgard, Inc., U.S.A.). A 1 M solution of $LiPF_6$ in ethylene carbonate/dimethyl carbonate (1:1) was used as the electrolyte. Galvostatic electrochemical experiments were carried out with an Arbin Instruments (College Station, TX) battery cycler at various rates.

3. RESULTS AND DISCUSSION

By using $CsOH.H_2O$ (2 g), KOH (6 g), LiOH (1 g), and $Co(NO_3)_2$ (0.58 g) as the starting materials, phase pure $LiCoO_2$ can be obtained after at least 16 hours of reaction at 200°C. To understand the reactions occurring in the molten flux, systematical ex situ XRD and SEM/TEM experiment were performed. Fig. 3.1 and 3.2 show the ex-situ XRD and SEM micrographs obtained from particles extracted as a function of reaction time at 200 °C from the flux comprising a 3:6:1 molar ratio of LiOH, KOH and $CsOH.H_2O$ with a melting point of approx. 180°C and the precursor $Co(NO_3)_2$.

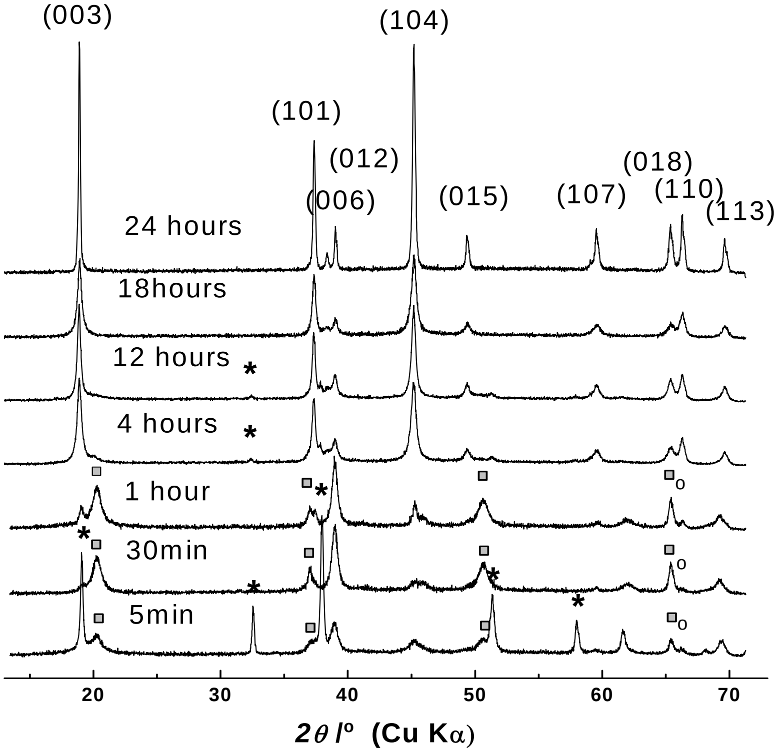

Figure 3.1. XRD of samples obtained in the molten hydroxides flux as a function of heat treatment time at 200 °C: A, 5 minutes; B, 30 minutes; C, 1 hour; D, 4 hours; E, 12 hours; F, 18 hours and G, 24 hours. Reflections due to $Co(OH)_2$ and CoOOH are indicated by asterisk and solid squares, respectively. Although the major, strong reflections of $LiCoO_2$ overlap with those of $Co(OH)_2$ and CoOOH, the weaker $LiCoO_2$ (110) reflection at approximately 60°, (marked with a circle) is well resolved in all the patterns. The $LiCoO_2$ reflections are indexed in G..

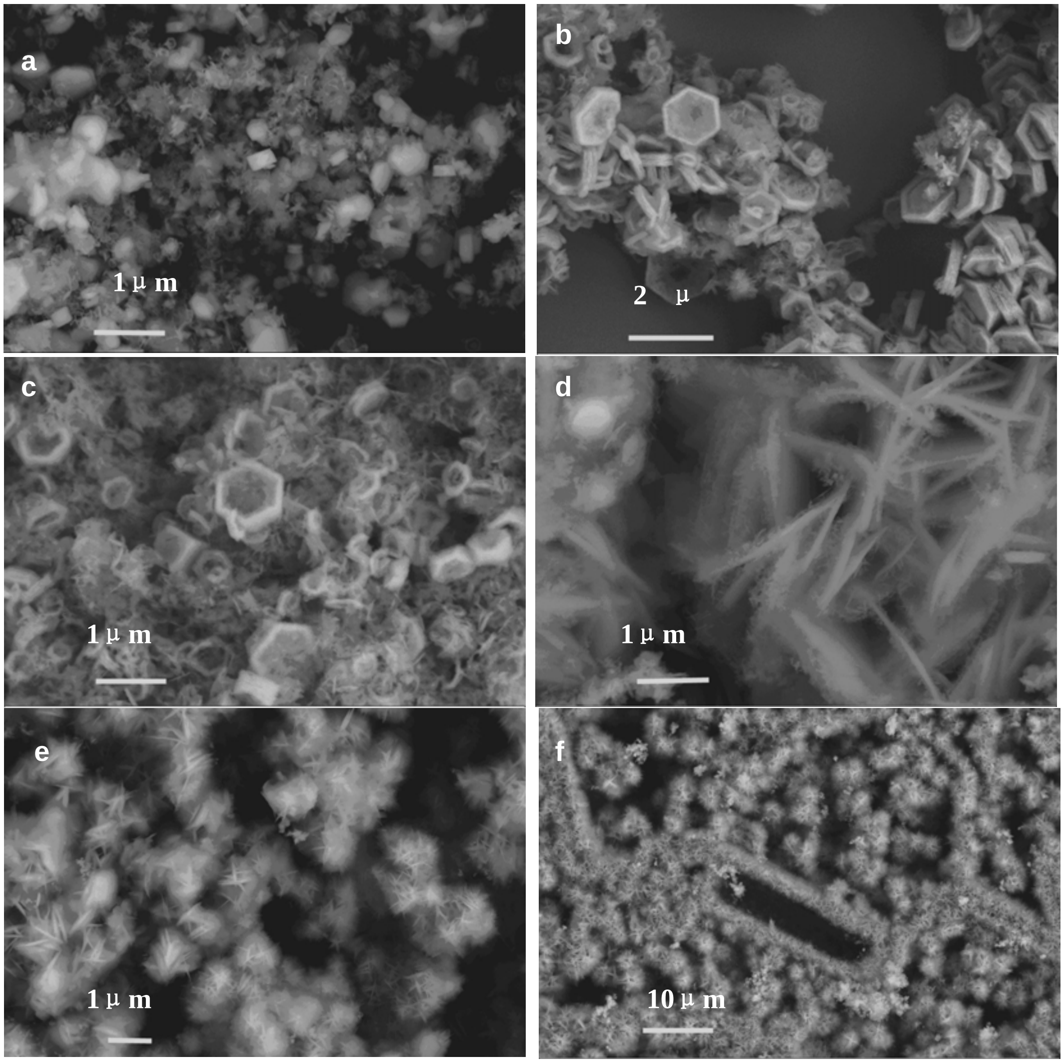

Figure 3.2. SEM images of the samples as a function of heat treatment time in the molten hydroxide flux: a, 5 minutes, b, 1 hour, c, 4 hours, d, 4 hours (different region), e, 18 hours, and f, 18 hours (different region). The scale bars are 2, 2, 1, 1, 1, and 10μm respectively.

Based on this data a series of reactions are proposed:

$$Co(NO_3)_2 + 4OH^- \rightarrow Co(OH)_4^{2-} + 2NO_3^- \qquad (1)$$

$$Co(OH)_4^{2-} \leftrightarrow Co(OH)_2 + 2OH^- \qquad (2)$$

$$2Co(OH)_2 + 0.5O_2 \rightarrow 2CoOOH + H_2O \qquad (3)$$

$$CoOOH + 7H_2O \leftrightarrow Co(OH_2)_6^{3+} + 3OH^- \qquad (4)$$

$$Co(OH_2)_6^{3+} + Li^+ \rightarrow LiCoO_2 + 4H_2O + 4H^+ \qquad (5)$$

Cobalt (II) oxides and hydroxides are amphoteric and dissolve in basic solutions to form the (blue) $Co(OH)_4^{2-}$ ion, the blue color being clearly visible in the initial washings of the solid product. After 5 minutes (sample A), $Co(OH)_2$ is observed as the major phase, (reaction (2)), and based on the sharp, intense reflections of $Co(OH)_2$ seen in the XRD pattern, the larger hexagonal-shaped plates in the SEM micrograph of Figure 3.2a are also assigned to this phase. Oxidation of Co^{2+} to Co^{3+} has commenced already and CoOOH is present as the secondary, less-crystalline phase. Some $LiCoO_2$ is formed even after 5 minutes of heating. Most of the $Co(OH)_2$ phase has been oxidized to CoOOH following 0.5–1 hour of heating (Figure 3.1b and c). A new morphology is observed, the large hexagonal plates, originally due to $Co(OH)_2$, leaching or dissolving from the center, the edges remaining intact. Fig 3.3 shows the electron diffraction pattern of the edges of the rings. This is consistent with a mixture or intergrowth of a layered CoOOH phase and a cubic, low-temperature $LiCoO_2$ phase.

Oxidation of the $Co(OH)_2$ particles (and Li^+/H^+ exchange) apparently occurs from the edges of the hexagonal plates, stabilizing the edges of the crystals and slowing down the

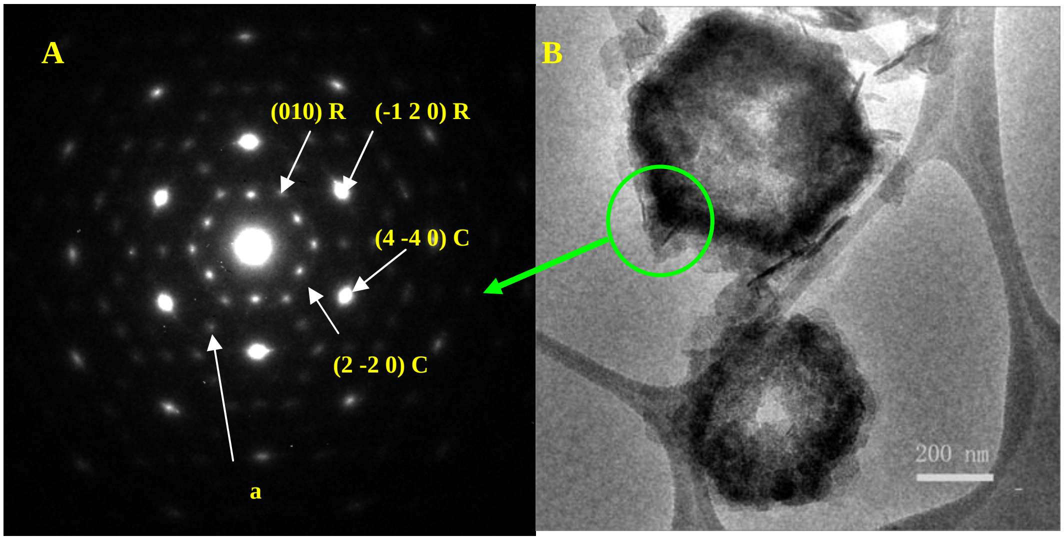

Figure 3.3. The electron diffraction pattern of the intermediate product of the reactions in the molten hydroxides flux (A) and the corresponding bright field image (B). The scale bar in (B) is 200 nm.

Co^{2+} dissolution. Exfoliation of the plates is also seen, consistent with ion-exchange between the layers and the layer shearing that is required for the transformation of $Co(OH)_2$ to CoOOH and $LiCoO_2$. At the same time, finer (rod-like) crystals of $LiCoO_2$ begin to nucleate and grow on the faces of the hexagonal plates; this phenomenon is much clearer in the SEM micrographs taken after heating for 4 hours (Figure 3.2d). At this stage, CoOOH and $Co(OH)_2$ are present only as minor phases and the small $LiCoO_2$ particles appear to act as new nucleation centers for $LiCoO_2$ growth. The growth directions can be more clearly seen following more extended heating, as shown in Fig. 3.4.

The morphology of the crystal assembly is similar to the “hyperbranched” growth seen, for example, for PbSe and PbS [28, 29]. These latter materials are cubic and hence a cubic 3D network is formed. In contrast, the layered material $LiCoO_2$, tends to form finely spaced plates or rods, the growth occurring on the *(001)* face forming rods dominated by *(00l)* faces. This growth mechanism is readily rationalized because the *(001)* surface is charged, as it is terminated by either O, Co, or Li. In contrast, growth in a perpendicular direction maintains charge neutrality. The high dielectric constant of these fluxes presumably helps in the termination of non-charge balanced *(001)* faces that form during growth. Finally, in the fourth stage, (12 to 24 hours), single phase $LiCoO_2$ is observed (Fig.3.1 G and Fig 3.2e); all the hexagonal rings have dissolved and the nucleation and growth of the $LiCoO_2$ smaller particles has resulted in spherical balls of branched, rod-like crystals. This morphology resembles the “desert rose” form of the

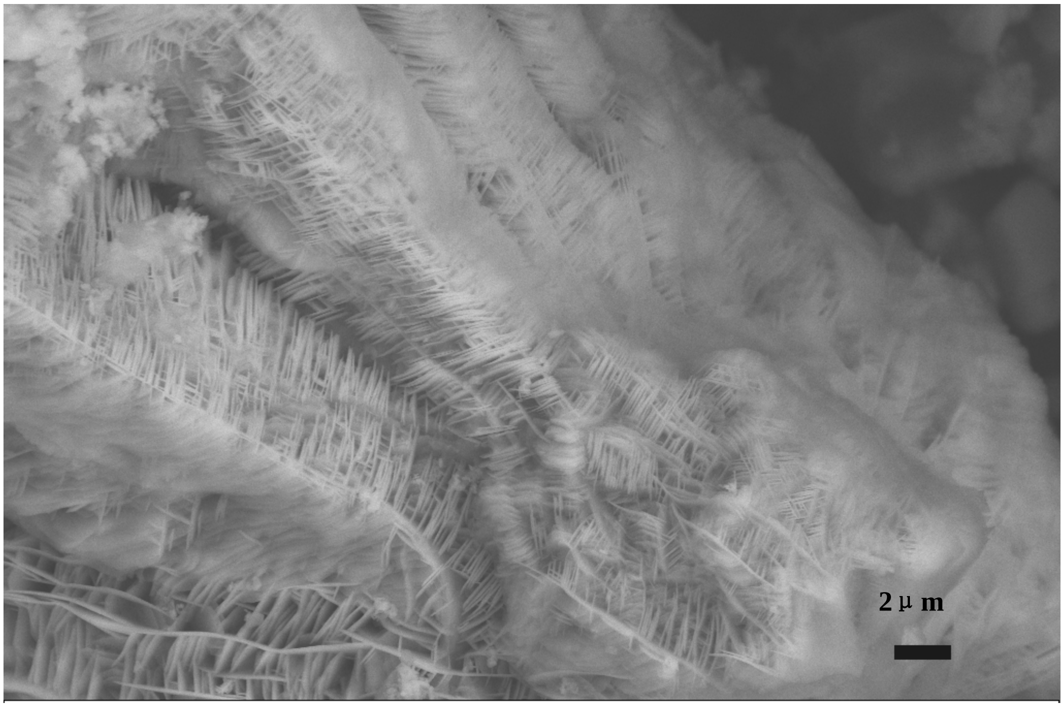

Figure 3.4. SEM image of 16 hour heat treated sample. The morphology is due to hyperbranched growth of $LiCoO_2$ in the molten hydroxide fluxes. The relative orientation relationship between the mother $LiCoO_2$ sheet and the branches can be clearly seen.

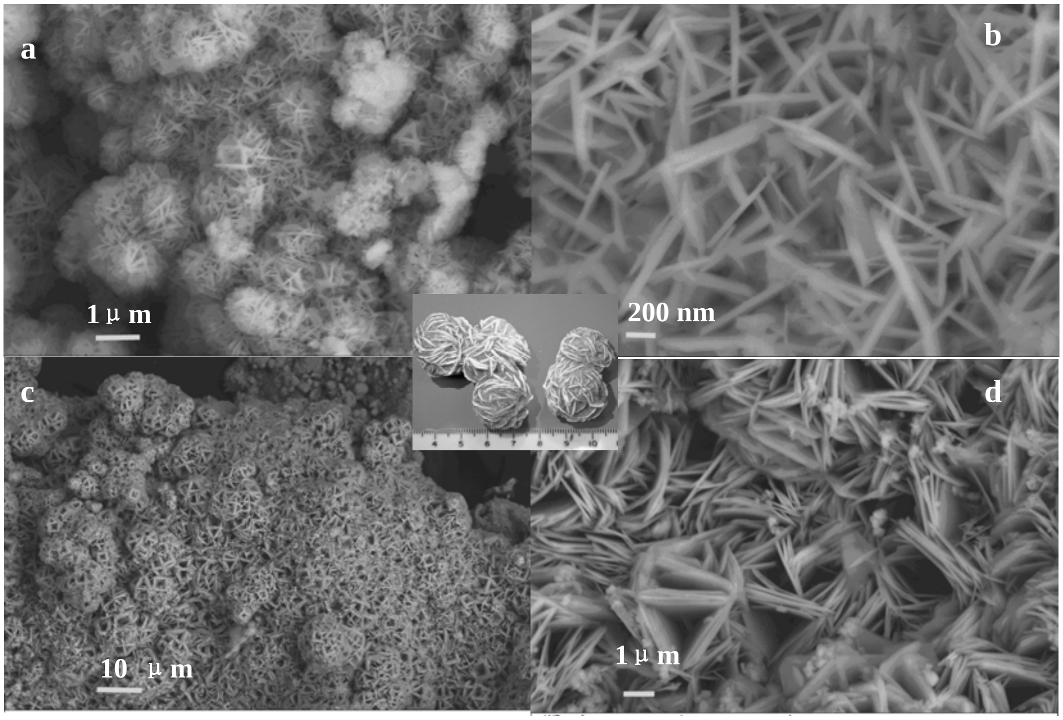

Figure 3.5. SEM image of $LiCoO_2$ samples obtained by heating in molten hydroxides for 24 (a,b) and 48 hours (c,d) at different magnifications. The scale bars are 1 μm, 200 nm, 10 μm and 1μm respectively. The inset shows a natural desert rose.

mineral gypsum (inset of Fig. 4.4). Bigger assemblies of the desert-rose balls are seen in Fig. 3.2 (F), this figure also illustrating how the larger plate-like $Co(OH)_2$ crystals, which served originally as nucleation sites, have slowly dissolved away to provide more cobalt for the growing desert-rose structures. The balls grow larger and the thin plates/rods of the ball grow thicker and begin to split into bundles on more extended heating (48 hours), and the crystallinity of the samples increase, as shown in Fig. 3.5

The growth mechanism is quite different from that seen by Tarascon et al. and Chiang et. al. for the conversion of $Co(OH)_2$ to CoOOH [30] and $LiCoO_2$ [31] via hydrothermal and solid state reaction syntheses. The final products in these studies were derived via a solid state reaction involving the original hexagonal shaped $Co(OH)_2$ crystals, CoOOH/$LiCoO_2$ particles with the same shape as the mother $Co(OH)_2$ crystal being formed [30, 31]. This mechanism is presumably similar to that responsible for the formation of the lithiated hexagonal rings, but is not responsible for the formation of final $LiCoO_2$ phase. In our case, solubility of $Co(OH)_2$ (and Co^{3+}) in the highly basic (and oxidizing) flux allows for the slow dissolution of the $Co(OH)_2$ phase, oxidation to form Co^{3+} and the growth of $LiCoO_2$ from nuclei on both the original $Co(OH)_2$ phase, and later on, on the $LiCoO_2$ rods.

Synchrotron radiation X-ray diffraction of the 48 hour material indicates that the material is phase-pure. The experimental data and the refinement is shown in Fig. 3.6. No Li/Co interchange was allowed during the refinement based on the results of ^{7}Li MAS NMR spectroscopy. Isotropic strain and shape factors were used since the particles have a

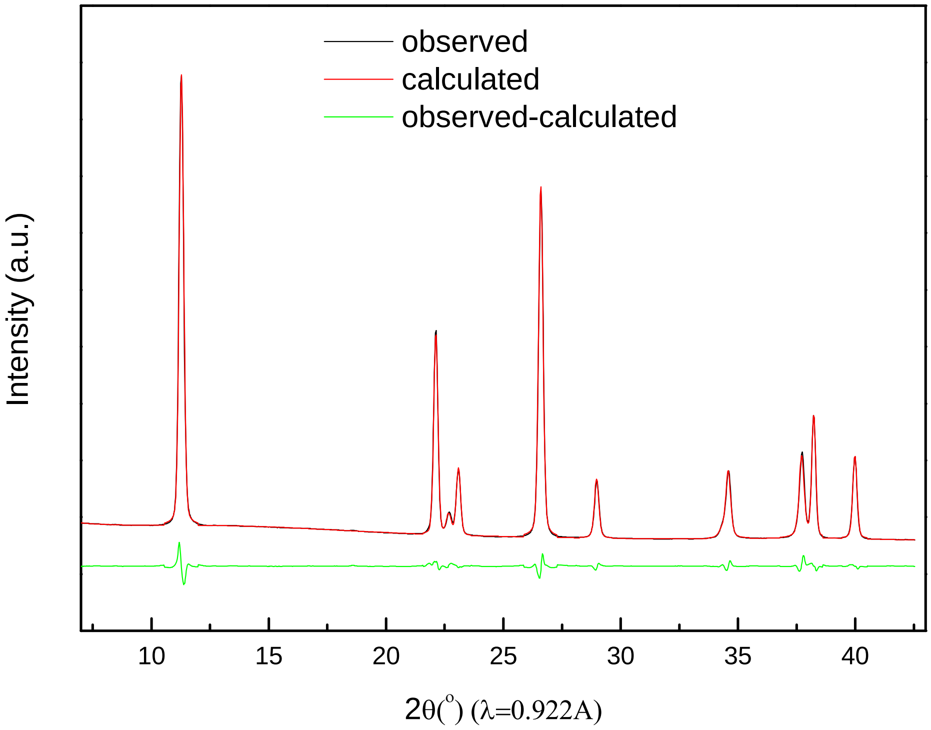

Figure 3.6. Synchrotron X-ray diffraction pattern and Rietveld refinement of the structure of desert-rose $LiCoO_2$ heated for 48 hours. The black, red and green lines correspond to the observed pattern, calculated peak positions and the difference of two patterns, respectively.

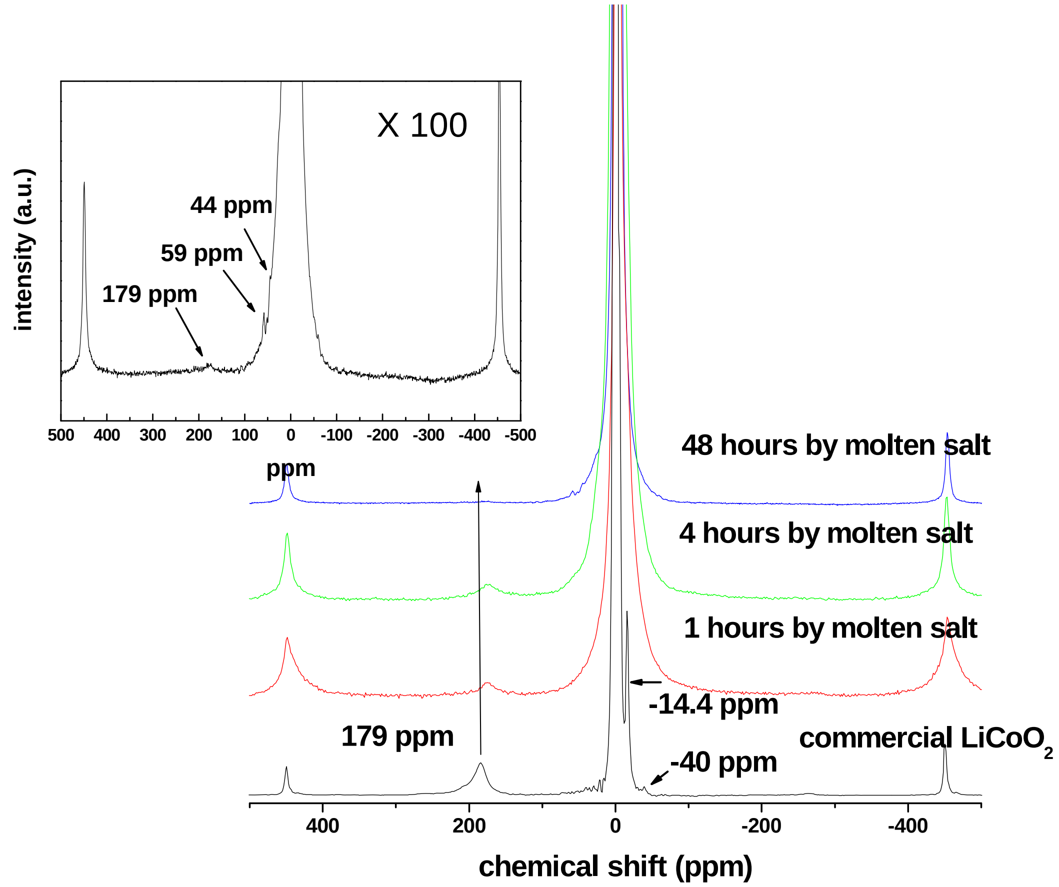

Figure 3.7. ^{7}Li MAS NMR results for commercial $LiCoO_2$ (Sigma-Aldrich) and products extracted following 1 hour, 4 hours and 48 hours heating in the molten salts system at 200°C. The ^{7}Li MAS NMR experiments were performed with a double-resonance 1.8 mm probe, built by Samoson and co-workers, on a CMX-200 spectrometer using a magnetic field of 4.7 T. The spectra were collected at an operating frequency of 29.46 MHz at a spinning frequency of 35kHz with a rotor-synchronized spin-echo sequence ($\pi/2-\tau-\pi-\tau-$acq.). $\pi/2$ pulses of 3.5 μs were used, with recycle delay times of 0.5 s. All the NMR spectra were referenced to a 1 M ^{7}LiCl solution, at 0 ppm.The inset shows a 100-fold enlargement on intensities of the spectrum of the 48 hours sample.

large aspect ratio as shown in SEM and TEM pictures, which led to a better fit. Cell parameters of c = 14.0803(3) Å, a = b = 2.81818(3) Å, with Rp = 1.38%, wRp = 2.21% were obtained. These cell parameters are slightly larger than those reported for micrometer-sized $LiCoO_2$, (typically a = b = 2.812–2.816 and c = 14.03–14.06 Å), but consistent with cell parameters reported previously for $LiCoO_2$ nanoparticles [25].

Significant incorporation of K^+ (or Cs^+) is excluded since K (or Cs) was not detected by EDAX. ^{7}Li MAS NMR spectroscopy, which is extremely sensitive to small variations in the stoichiometry of $Li_{1\pm x}CoO_2$ materials [32-36] also indicates that these materials are more ordered than a typical sample of commercial $LiCoO_2$ prepared by high temperature route. Fig 3.7 shows ^{7}Li MAS NMR spectra of a commercial $LiCoO_2$ and the samples obtained after 1 hour, 4 hours and 48 hours reaction in the molten flux. The spectra of all the samples are dominated by the signal at 0 ppm due to the stoichiometric regions of sample, where only Co^{3+} (low-spin d^6) ions are present. The peaks shown in the spectrum of commercial $LiCoO_2$ at 179, -14.4 and -40 ppm are the typical resonances for Li-excess $LiCoO_2$. [32-36] Although present in molten flux samples following 1 and 4 hours of heating, these peaks are not seen in the 48 hour desert-rose sample unless the spectrum of this sample is enlarged 100-fold times. Thus, based on a comparison of the relative intensity of the different peaks, the 48 hour molten salt sample is very close to stoichiometric $LiCoO_2$, and is more stoichiometric and ordered than the commercial sample prepared by a solid state reaction.

TEM of the 24 hour sample confirms that the desert-rose structure is formed from rod-like crystals, with the (001) faces representing the major surfaces of these rods, and the surfaces of the desert-rose balls being terminated by rounded faces perpendicular to (001) planes. As shown in Fig. 3.8, the (003) planes, with d-spacings of 4.68 Å, corresponding to the spacing between the Co layers are clearly observed, parallel to length of the rod. Furthermore, since many of the rods are thin enough to be imaged perpendicular to the [001] direction, this indicates that the surface perpendicular to this direction is also large. The surfaces perpendicular to the (001) face are electrochemically active for Li^+ deintercalation/insertion.

Electrochemical tests on desert-rose $LiCoO_2$ and a commercial sample were performed at rates of 1000 and 5000mAh/g, (7 and 36C if the practical capacity is assumed to correspond to removal of 50% of Li) (Fig 3.9). Desert rose $LiCoO_2$ showed a large discharge capacity of 155mAh/g at a 7C rate (between 2.5-4.5V), and the same capacity at 36C (2–4.8V). The overpotential during high rate cycling is also much lower than that seen for the commercial micron-sized material. The excellent high rate performance is ascribed to the desert rose morphology, where the the surfaces of the balls are covered by the Li-insertion active surfaces. This morphology also appears to have an advantage over $LiCoO_2$ cathode materials (e.g. [25]) comprising individual nanoparticles, since the individual particles within the ball are all electrically connected, [N.b., SEM studies of the cathode materials confirm that the desert rose morphology is maintained after grinding with carbon and pressing to form the battery cell.

Both the precursor salts and anions have a pronounced affect of the morphology of

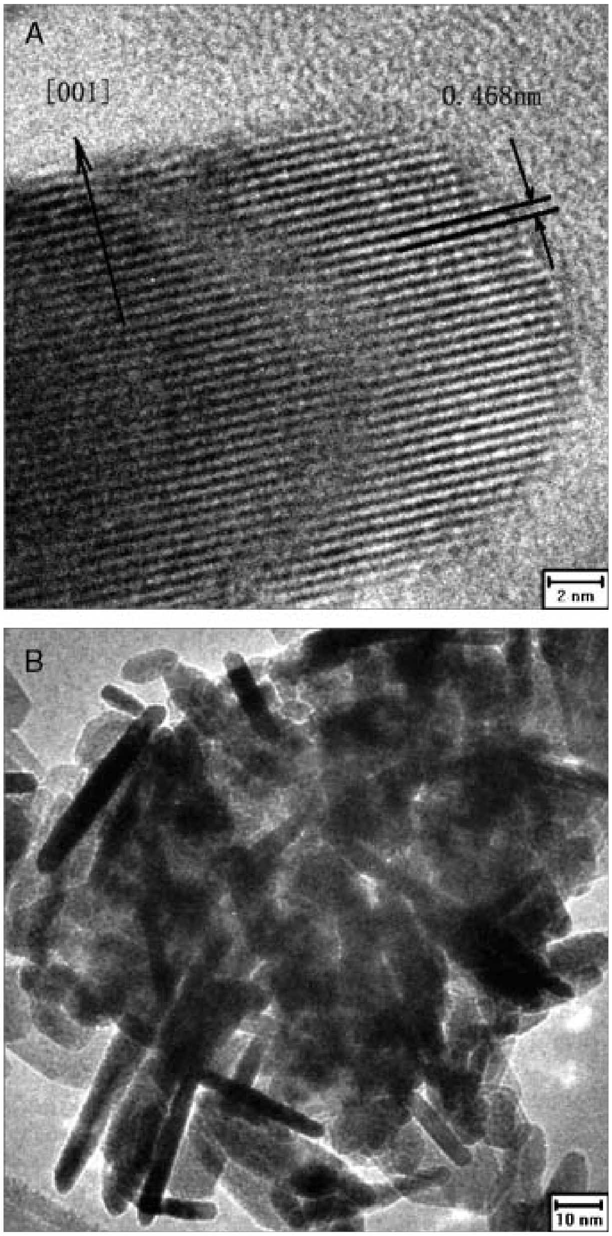

Figure 3.8. High resolution TEM image of desert rose $LiCoO_2$ formed after 24 hours of heating (A) and the corresponding low magnification image (B). The scale bars in (A) and (B) are 2 and 10 nm respectively.

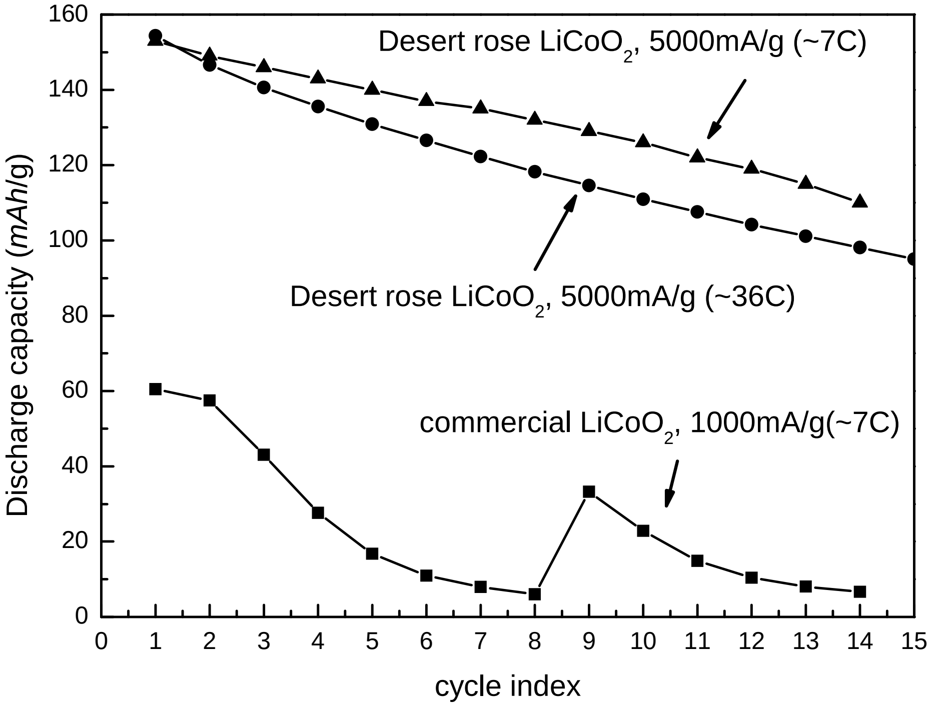

Figure 3.9. Discharge capacities as a function of cycle number and current density for desert-rose-like $LiCoO_2$ (2.5–4.5V; 1000 mAg^{-1} (triangles), 2.0–4.8V; 5000 mAg^{-1}; circles) and commercial $LiCoO_2$ (squares; 5000 mAg^{-1}). The cycling voltage windows were adjusted to account for the large overpotentials observed at high rate, which were particularly pronounced for the commercial $LiCoO_2$ sample. The voltage range for this sample was increased from 2.0–5.0 V to 2.0–5.3 V at the end of cycle 8.

the final product. For example, increasing the NO_3^- concentration in the low temperature molten salt systems, results in a progressively less well developed desert rose morphologies and the formation of finer, isolated hexagonal plates, with much poorer electrochemical performance. Fig 3.10 shows the SEM images of samples synthesized in the $LiNO_3$-KNO_3-LiOH-KOH-CsOH eutectic flux, with the (NO_3^-):(OH^-) ratios being different. $Co(NO_3)_2$ was used as the starting material and the mixtures were heated at 24 hours at 200 ºC. The results showed that as the concentration of NO_3^- increases, the final $LiCoO_2$ products show less desert rose morphology and less branched growth. More fine, isolated hexagonal plates are observed; this is the most clear in Fig. 3.10(d).

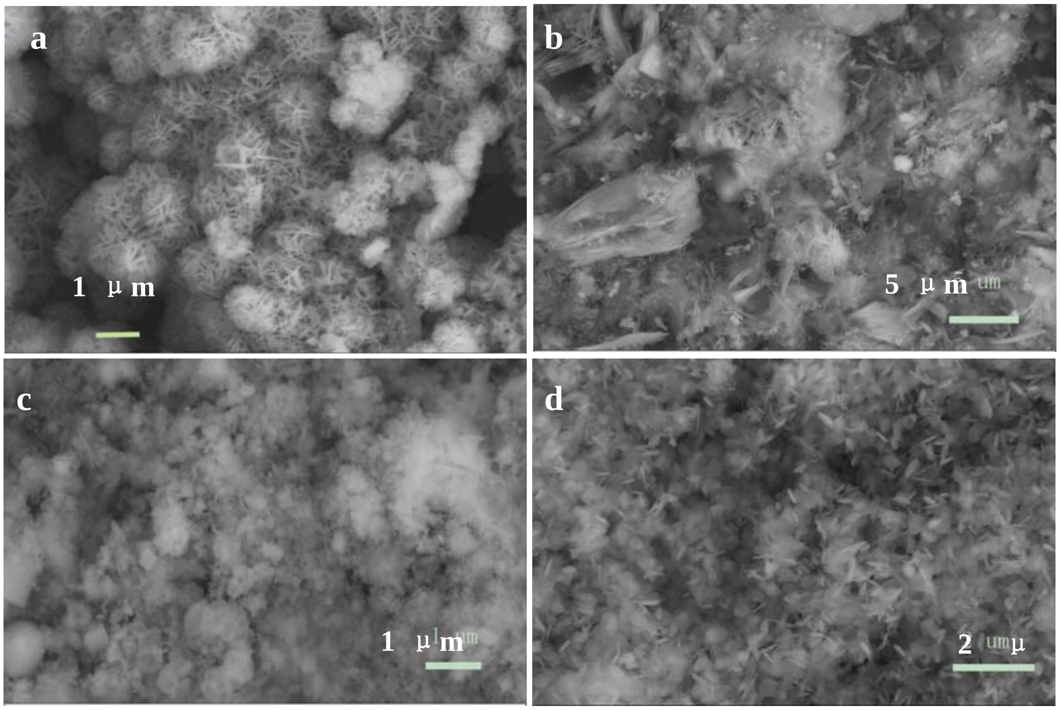

Figure 3.10. SEM images of $LiCoO_2$ samples made with various nitrates: hydroxide ratios. The $LiNO_3$-KNO_3-LiOH-KOH-CsOH eutectic system was used for all the samples with total (NO_3^-) : (OH^-) ratios of 2:1,(d) 1:1 (c) and 1:4 (b). An image of desert-rose $LiCoO_2$ ((NO_3^-) : (OH^-) ratio of 1:75) (a) is shown below for comparison. The scale bars are 1, 5, 1 and 2 μm, respectively.

4. CONCLUSIONS AND IMPLICATIONS

In conclusion, the molten hydroxide flux method opens up a new route to synthesize lithium transition metal oxides at very low temperatures. The approach yields crystalline products with excellent cation ordering between the Li and Co layers. The large flexibility in type and concentration of the anion provides an opportunity to control the morphology and preferred growth direction, providing the potential to design materials with controlled morphologies for future applications. Low concentrations of nitrates yield the so-called desert rose morphology via a dissolution-oxidation-precipitation mechanism, a morphology which lead to high rate electrochemical performance.

REFERENCES

1. Du, K.; Yang, Y. N.; Hu, G. R.; Peng, Z. D.; Qi, L., *Chin. J. Inorg. Chem.* **2008,** 24, (4), 615-620.
2. Chang, Z. R.; Chen, Z. J.; Wu, F.; Tang, H. W.; Zhu, Z. H., *Acta Phys.-Chim. Sin.* **2008,** 24, (3), 513-519.
3. Reddy, M. V.; Rao, G. V. S.; Chowdari, B. V. R., *J. Phys. Chem. C* **2007,** 111, (31), 11712-11720.
4. Ni, J. F.; Zhou, H. H.; Chen, J. T.; Zhang, X. X., *Mater. Lett.* **2007,** 61, (4-5), 1260-1264.
5. Reddy, M. V.; Rao, G. V. S.; Chowdari, B. V. R., *J. Power Sources* **2006,** 159, (1), 263-267.
6. Wen, L.; Lu, Q.; Xu, G. X., *Electrochim. Acta* **2005,** 51, (21), 4388-4392.
7. Du, K.; Qi, L.; Hu, G. R.; Peng, Z. D., *Chin. J. Inorg. Chem.* **2006,** 22, (5), 867-871.
8. Tan, K. S.; Reddy, M. V.; Rao, G. V. S.; Chowdari, B., *J. Power Sources* **2005,** 147, (1-2), 241-248.
9. Kim, J. H.; Myung, S. T.; Sun, Y. K., *Electrochim. Acta* **2004,** 49, (2), 219-227.
10. Han, C. H.; Hong, Y. S.; Kim, K., *Solid State Ionics* **2003,** 159, (3-4), 241-247.
11. Han, C. H.; Hong, Y. S.; Park, C. M.; Kim, K., *J. Power Sources* **2001,** 92, (1-2), 95-101.

12. Liang, H. Y.; Qiu, X. P.; Chen, H. L.; He, Z. Q.; Zhu, W. T.; Chen, L. Q., *Electrochem. Commun.* **2004,** 6, (8), 789-794.

13. Liang, H. Y.; Qiu, X. P.; Zhang, S. C.; He, Z. Q.; Zhu, W. T.; Chen, L. Q., *Electrochem. Commun.* **2004,** 6, (5), 505-509.

14. Breger, J.; Kang, K.; Cabana, J.; Ceder, G.; Grey, C. P., *J. Mater. Chem.* **2007,** 17, (30), 3167-3174.

15. Kang, K. S.; Meng, Y. S.; Breger, J.; Grey, C. P.; Ceder, G., *Science* **2006,** 311, (5763), 977-980.

16. Ohzuku, T.; Makimura, Y., *Chem. Lett.* **2001**, (8), 744-745.

17. Yabuuchi, N.; Ohzuku, T. *J. Power Sources* **2003**, 119, 171-174.

18. Chung, S. Y.; Bloking, J. T.; Chiang, Y. M., *Nat. Mater.* **2002,** 1, (2), 123-128.

19. Bao, S. J.; Liang, Y. Y.; Zhou, W. H.; He, B. L.; Li, H. L., *J. Power Sources* **2006,** 154, (1), 239-245.

20. Sun, Y. K.; Myung, S. T.; Kim, M. H.; Prakash, J.; Amine, K., *J. Am. Chem. Soc.* **2005,** 127, (38), 13411-13418.

21. Chen, H. L.; Qiu, X. P.; Zhu, W. T.; Hagenmuller, P., *Electrochem. Commun.* **2002,** 4, (6), 488-491.

22. Sides, C. R.; Martin, C. R., *Adv. Mater.* **2005,** 17, (1), 125-+.

23. Larcher, D.; Palacin, M. R.; Amatucci, G. G.; Tarascon, J. M., *J. Electrochem. Soc.* **1997,** 144, (2), 408-417.

24. Amatucci, G. G.; Tarascon, J. M.; Larcher, D.; Klein, L. C., *Solid State Ionics*

1996, 84, (3-4), 169-180.

25. Okubo, M.; Hosono, E.; Kim, J.; Enomoto, M.; Kojima, N.; Kudo, T.; Zhou, H. S.; Honma, I., *J. Am. Chem. Soc.* **2007,** 129, (23), 7444-7452.

26. Hu, C. G.; Liu, H.; Dong, W. T.; Zhang, Y. Y.; Bao, G.; Lao, C. S.; Wang, Z. L., *Adv. Mater.* **2007,** 19, (3), 470-+.

27. Liu, H.; Hu, C. G.; Wang, Z. L., *Nano Lett.* **2006,** 6, (7), 1535-1540.

28. Zhu, J.; Peng, H. L.; Chan, C. K.; Jarausch, K.; Zhang, X. F.; Cui, Y., *Nano Lett.* **2007,** 7, (4), 1095-1099.

29. Bierman, M. J.; Lau, Y. K. A.; Jin, S., *Nano Lett.* **2007,** 7, (9), 2907-2912.

30. Pralong, V.; Delahaye-Vidal, A.; Beaudoin, B.; Gerand, B.; Tarascon, J. M., *J. Mater. Chem.* **1999,** 9, (4), 955-960.

31. Chiang, Y. M.; Jang, Y. I.; Wang, H. F.; Huang, B. Y.; Sadoway, D. R.; Ye, P. X., *J. Electrochem. Soc.* **1998,** 145, (3), 887-891.

32. Levasseur, S.; Menetrier, M.; Suard, E.; Delmas, C., *Solid State Ionics* **2000,** 128, (1-4), 11-24.

33. Menetrier, M.; Saadoune, I.; Levasseur, S.; Delmas, C., *J. Mater. Chem.* **1999,** 9, (5), 1135-1140.

34. Levasseur, S.; Menetrier, M.; Delmas, C., *Chem. Mater.* **2002,** 14, (8), 3584-3590.

35. Menetrier, M.; Carlier, D.; Blangero, M.; Delmas, C., *Electrochem. Solid State Lett.* **2008,** 11, (11), A179-A182.

36. Menetrier, M.; Shao-Horn, Y.; Wattiaux, A.; Fournes, L.; Delmas, C., *Chem.*

Mater. **2005,** 17, (18), 4653-4659.

CHAPTER 4

Concaved Cuboctahedron $LiCoO_2$ as a Cathode Material for Lithium Ion Battery by Direct Lithiation from Cobalt Oxide

Hailong Chen, Lijun Wu, Lihua Zhang, Yimei Zhu, Clare P. Grey

Department of Chemistry

Stony Brook University, Stony Brook, NY 11794-3400

To be submitted

ABSTRACT

$LiCoO_2$, with a novel and unique morphology, the concaved cuboctahedron, was synthesized by using hydrothermal synthesis. Each cuboctahedron consists of four equivalent hexagonal plates, which penetrate each other with a 70.5^o angle. Electron diffraction shows that these comprise a 4-fold twin crystal of $LiCoO_2$. The growth mechanism of the twin crystal is proposed to involve selective leaching of CoO and Li-Co ion-exchange in the cubic precursor, CoO, followed by the isotropic growth of the $LiCoO_2$ plates.

1. INTRODUCTION

The moderate performance of most of the current LIB systems at high rates results from many factors. One rate limiting step in the electrochemical reaction of a LIB system is on the cathode side. Rate limitations can involve the Li^+ diffusion from bulk to the surface of the particle and from surface to the electrolyte. The diffusion of Li depends strongly on its diffusion path in the lattice of the cathode material. In an ideal case, high rate performance is easier to achieve if Li diffusion is through 3-D channels in the lattice and if the diffusion path is short. Spinel $LiMn_2O_4$ has been intensively studied since it has a cubic lattice and the Li diffusion occurs through 3-D channels. However, this material suffers from other problems such as the relatively low capacity and Mn dissolution in the electrolyte, especially at elevated temperatures[1, 2]. $LiCoO_2$ and the $LiMO_2$ (M= Ni, Fe, Mn, Co) type layered materials have 2-D channels. As discussed in Chapter 1, this implies that the Li ion exchange between the cathode and the electrolyte strongly depends on the morphology of the cathode particles and that not all the surface is active surface for Li insertion/extraction. The recently developed olivine type $LiFePO_4$ has very good high rate performance due to presumably the very small particle sizes and large surface area [3-5]. However, theoretical calculations [6] and high temperature neutron diffraction experiments [7] have both shown that $LiFePO_4$ typically has 1-D Li ion diffusion channels along *b* direction. The rate is similarly expected to have a dependence on the -morphology

In our earlier work discussed in Chapter 3, we have shown that by designing a high aspect ratio of primary particles and making 3-D assembled structure, the 2-D diffusion material $LiCoO_2$ can be turned into a pseudo-3-D diffusion material which can have excellent high-rate performance. Here we report another example where we change 2-D type diffusion to a pseudo-3-D type of Li diffusion in $LiCoO_2$ by crystal engineering. The synthesis and characterization of concaved cuboctahedron shaped $LiCoO_2$ by a hydrothermal method will be discussed.

In our previous work we used a basic, oxidizing and low melting hydroxide flux to synthesize $LiCoO_2$. $Co(OH)_2$ is first precipitated in this flux, the hydroxide slowly oxidizing to Co^{3+} first in form of CoOOH, and partially lithiated CoOOH, and finally as phase-pure $LiCoO_2$. This reaction is driven by the much lower solubility of Co(III) than Co(II) in the molten flux. Dissolution of the partially lithiated

$Co(OH)_2$/CoOOH also occurred, to produce unusual morphologies. Since the edges of the $Co(OH)_2$ plate-like hexagonal crystal were stabilized due to almost immediate Co^{2+} oxidation and Li^+/H^+ insertion, leaching occurred from the center of the dominant surfaces, the (001) planes, leading to the formation of hexagonal rings as an intermediate morphology. These rings, along with some non-leached $Co(OH)_2$ surfaces, serve as initial nucleation sites for $LiCoO_2$ growth, directly from the flux, or via dissolution of the lithiated CoOOH phase and then reprecipitation as $LiCoO_2$. The $LiCoO_2$ (001) faces then serve as new nucleation sites for further growth. New $LiCoO_2$ rods or sheets grow from these faces. Growth occurs along a direction perpendicular to the [001] direction, with a characteristic angle of 70.5^o between the original (001) face and the growth direction. The final product, which forms the so-called “desert rose” morphology found in natural minerals such as gypsum, is formed from hyperbranched growth, in which many thin rods and sheets form a 3-D assembly and each piece of the rod is physically and electrically connected. Fig. 4.1 shows a high magnification SEM image on the surface of a “desert rose” $LiCoO_2$ assembly, with some of these 70.5^oC angles labeled.

To further study the growth mechanism of $LiCoO_2$ and other $LiMO_2$ type cathode materials in highly basic solutions, hydrothermal methods were used instead of molten fluxes. Because in hydrothermal conditions, water is added as a solvent and the concentration of anions such as OH^- is lower, nucleation is slowed down and the growth process is accelerated at the same time due to the lower viscosity of the aqueous solution in comparison to the molten fluxes. The starting material

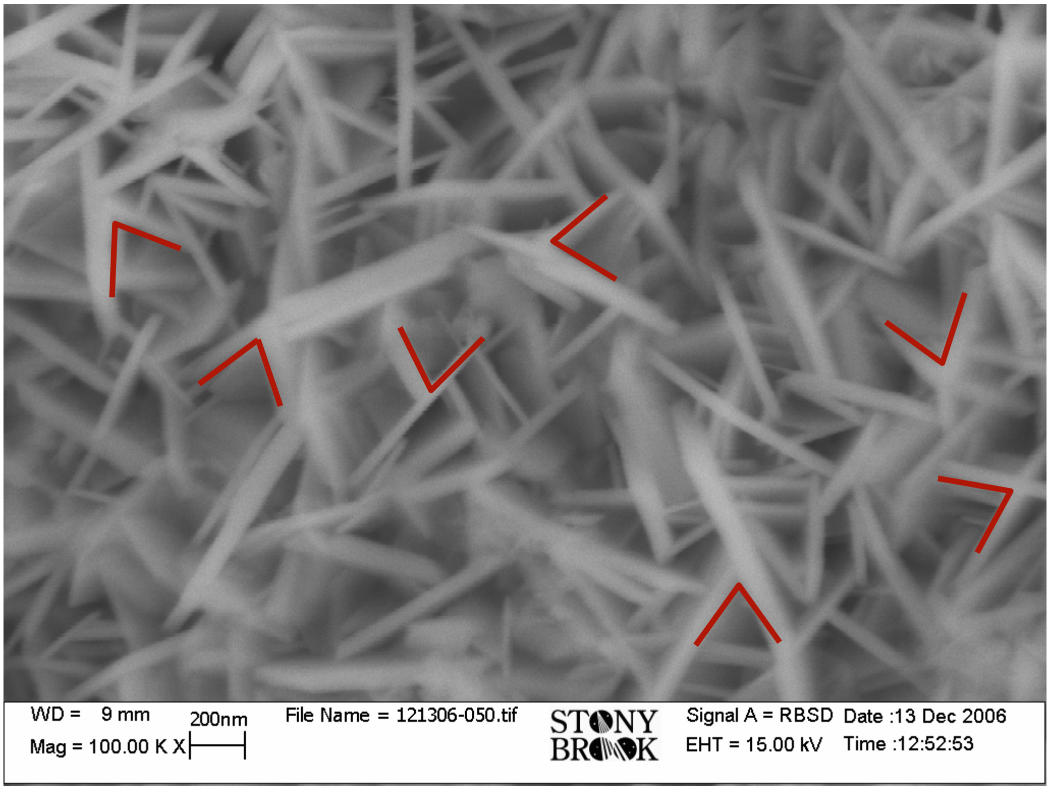

Figure 4.1. SEM image of the surface of the “desert rose” $LiCoO_2$. The angles indicated by the red lines are about 70.5°

combination used in our first hydrothermal synthesis is almost the same as used in previous molten flux method, except that CsOH was not used and water was used as solvent.

2. EXPERIMENTAL

2.1. Synthesis

Two synthetic procedures were used in this work to prepare the concaved cuboctahedron morphology. In the first procedure, 0.58 g $Co(NO_3)_2$ (Sigma-Aldrich, 98%) was dissolved in 5 ml distilled water to form a clear reddish solution. 7 g of KOH (Sigma-Aldrich, >85%) and 1 g of LiOH (Sigma-Aldrich, 99%) were dissolved in 10 ml distilled water. The $Co(NO_3)_2$ solution was then added slowly to the hydroxides solution while stirring. The resulting solution was transferred to a Teflon lined hydrothermal bomb and was heated statically in an oven at 200^oC for 24 to 48 hours. After the bomb was cooled down to room temperature, the product was washed with distilled water and centrifuged several times. Some of the samples were washed with 0.1M hydrochloric acid to remove the $Co(OH)_2$. The final washed products were dried overnight in an oven at 80^oC. Higher yields of the concaved cuboctahedron morphology were observed by using the second procedure, in which nanoparticles of CoO or $Co(OH)_2$ were used as the Co source instead of cobalt nitrate. The nanoparticles of CoO were prepared by dehydration of commercial $Co(OH)_2$ (Sigma-Aldrich) in a tube furnace under Ar atmosphere. Nanoparticles of $Co(OH)_2$

were prepared by a precipitation method: 0.1M $Co(NO_3)_2$ solution was added slowly into 0.1M LiOH (Co:Li ratio=1:2) solution while stirring. The products were filtered and then washed with distilled water and dried at 70^{o}C overnight.

2.2. Characterization

Powder X-ray diffraction patterns were collected either on a Rigaku MiniFlex diffractometer or at beamline X16C at Brookhaven National Laboratory. The SEM images were taken by using a LEO-1550 field emission scanning electron microscope. A JEOL 2100F high resolution transmission electron microscope was used to obtained atomic images and single particle select area electron diffraction (SAED) patterns.

2.3. Electrochemistry

The as prepared $LiCoO_2$ sample was mixed with poly-vinylidene fluoride binder and acetylene black (6:1:3 wt %) in N-methyl pyrrolidone (NMP) to make a thick slurry. The slurry was deposited on an aluminum foil by using a doctor-blade method and dried at 80^{o}C overnight. Coin cells (CR2032, Hohsen Corp.) were assembled in an argon-filled glove box. Each cell contains typically about 6-8 mg of active material, separated from the Li foil anode by a piece of Celgard separator (Celgard, Inc., U.S.A.). A 1 M solution of $LiPF_6$ in ethylene carbonate/dimethyl carbonate (1:1) was used as the electrolyte. Electrochemical experiments were carried out on a battery cycler (Arbin Instruments, College Station, TX) in galvanostatic mode at various rates.

3. RESULTS AND DISCUSSION

Although the starting material combination used in the first hydrothermal preparation method was very similar to that used in our previous molten flux method, except for the omission of the CsOH and the use of water as a solvent, very different morphologies were obtained. Surprisingly, in the final product of a 24 hours reaction at 200°C, many very regular, uniform and extremely unusual concaved cuboctahedron-shaped crystals are seen by SEM as shown in Fig. 4.2a. Figure 4.2b and c show two single particles in different orientations, and Fig. 4.2d shows a sketch drawing showing the perspective geometry. Each cuboctahedron particle consists of four equivalent hexagonal plates, and the angles between each two of these plats are all 70.5°, so as to maintain an overall cubic symmetry. To our best knowledge, this shape of crystal has only been reported once before for CuS by Wu et al.[8]. However, unlike some of the crystals of CuS found by Wu et al., our crystals are much more uniform and always comprise 4 hexagonal plates, while in the CuS system some particles contained 2 or 3 plates. Apart from the geometrical simplicity and beauty of these unique crystals, a number of questions are raised: what is this material and how and why does it form?

The XRD pattern of this product shows a mixture of $Co(OH)_2$, CoO and $LiCoO_2$. $Co(OH)_2$ is formed from the reaction of $Co(NO_3)_2$ and OH^- while CoO is formed from the decomposition of the unstable $Co(OH)_2$ phase. Presumably, $LiCoO_2$ forms from the lithiation of either $Co(OH)_2$ or CoO. The product was quickly washed

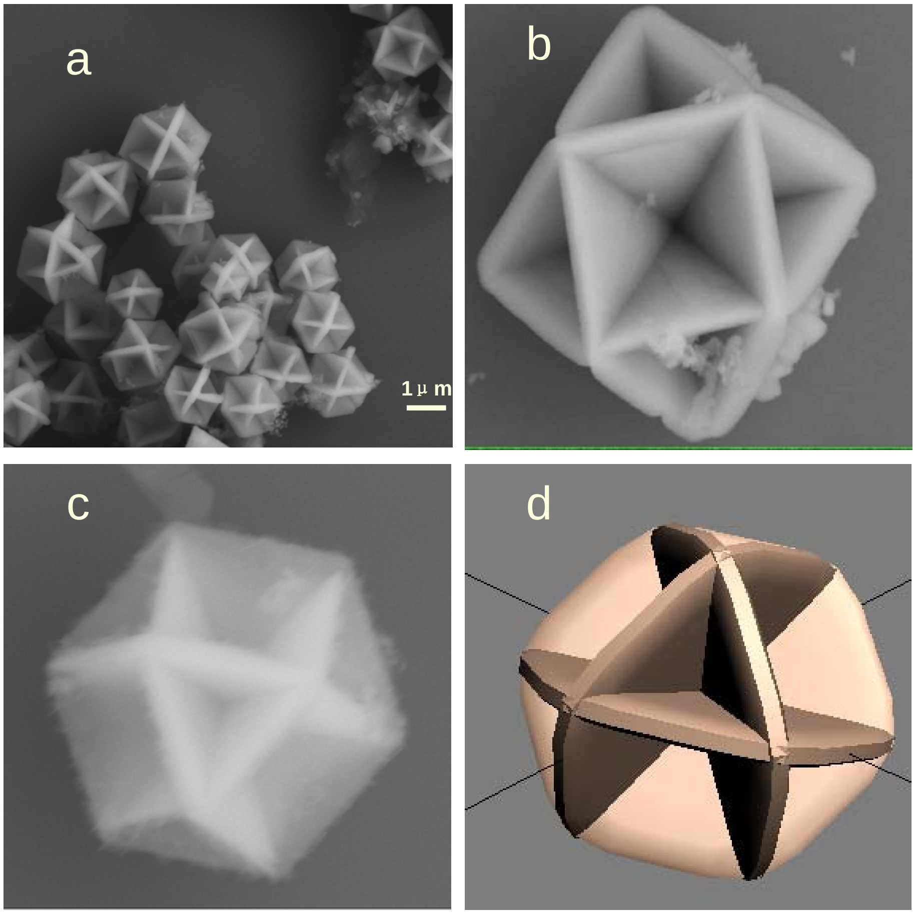

Figure 4.2. (a) SEM image of concaved cuboctahedron Li_xCoO_2 particles; (b) The "(100)" view of a single particle; (c) The "(111)" view of a single particle; (d) Schematic drawing of the particle.

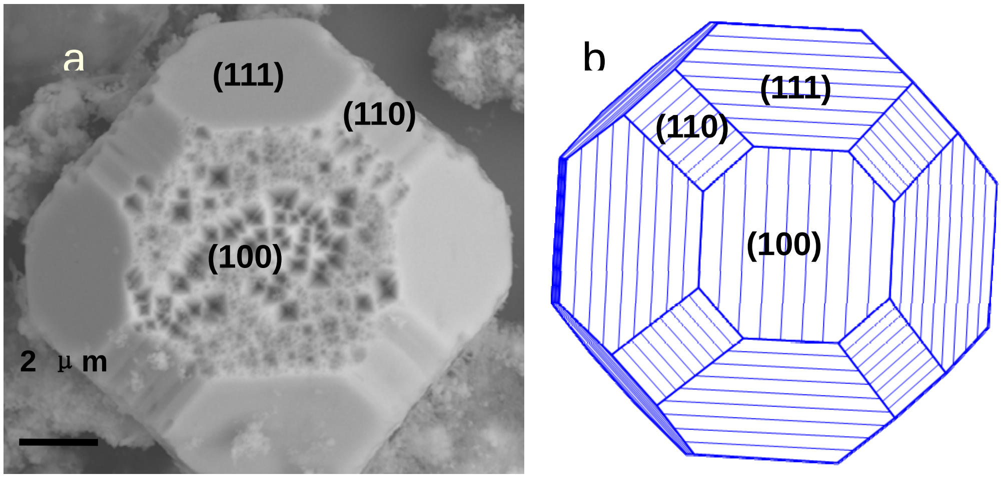

Figure 4.3. (a) A single particle with truncated cube shape. (b) Schematic drawing of a truncated cube.

with 0.1M HCl to dissolve the $Co(OH)_2$ phase. Only the CoO and $LiCoO_2$ phases were seen by XRD, the cuboctahedrons still being observed by SEM. The lattices of CoO and $LiCoO_2$ are similar, the lattice of $LiCoO_2$ being derived from CoO by replacing every other close paced layer of Co by Li so that the 3-fold symmetry along 3 out of 4 [111] directions is lost. Although the direct oxidation of CoO to $LiCoO_2$ has not been reported before as far as we know, from the crystallographic point of view, it is very possible that the concaved cuboctahedrons are derived from the lithiation of the CoO phase. This suggestion will now be explored below.

In addition to the cuboctahedrons, some large crystals are also seen in the sample before and after washing, as shown in Fig. 4.3a. These crystals are derived by truncating the edges and corners of a cube to expose the [9], {100} and {110} faces as shown in the schematics in Fig. 4.3b. These large cubic crystals are ascribed to CoO since CoO has a cubic lattice (space group Fm-3m, a=4.26 Å) and the reflections of CoO in the XRD patterns are very sharp and intense. They show obvious pitting on their {100}faces but the {111) faces remain intact. The nature of the pitting clearly shows that the dissolution of CoO in this basic solution and hydrothermal conditions is selective. This can be explained by that the {111} faces are charge polarized surface so that they are easy to be stabilized by electrical double layers, and it is more difficult to extract a ion from the surface; while the {100} faces are charge neutral surface so that Co(II) can be easily pulled out and diffuse into the solution [9]. On the other hand, since Co(II) tends to be oxidized to Co(III) under basic conditions, Li insertion along the {111} planes of CoO and a corresponding oxidation of Co(II) to

Co(III) are plausible. Given that the cuboctahedrons show an overall cubic symmetry, it is very possible that the concaved cuboctahedron grows off from a CoO mother crystal by selective pitting and preferred growth along a specific direction.

Although the results of XRD can not directly determine whether the concaved cuboctahedron crystal is $LiCoO_2$ or not, since it is in a mixture of two phases, a TEM and electron diffraction study on the first sample batch showed that this unique crystal is Li_xCoO_2. Fig. 4.4a shows the morphology of a concaved cubotahedron viewed along the normal direction of one hexagonal plate (labeled as V1, which shows a bright contrast). The selected-area diffraction pattern (SADP) taken of the V1 plate is shown in fig. 4.4b. The bright spots can be indexed as the $[001]_H$ pattern of Li_xCoO_2 (here subscript H denotes the index based on the hexagonal lattice of $LiCoO_2$). They can not be indexed as CoO as the lattice parameters of $LiCoO_2$ and CoO are different. Also, these patterns can not be indexed as Co_3O_4 as $LiCoO_2$ can be distinguished from Co_3O_4 based on differences in the extinctions. On this basis, it can be concluded that the concaved cubotahedron is Li_xCoO_2, rather than CoO or Co_3O_4. The normal of the hexagonal plate is $[001]_H$, while its side planes are $(100)_H$, $(010)_H$ and $(1\text{-}10)_H$, respectively. However, the ^7Li MAS NMR spectrum of this sample is rather like charged Li_xCoO2 than the stoichiometric $LiCoO_2$. At the same time, the capacity of this sample is low (~30-80 mAh/g between 2-4.8V)) . This implies that this sample may be Li_xCoO_2 with Li deficiency. Therefore there may be Li vacancies in the lattice.

The weak spots in Fig. 4.4b indicated by the black arrow suggest the presence

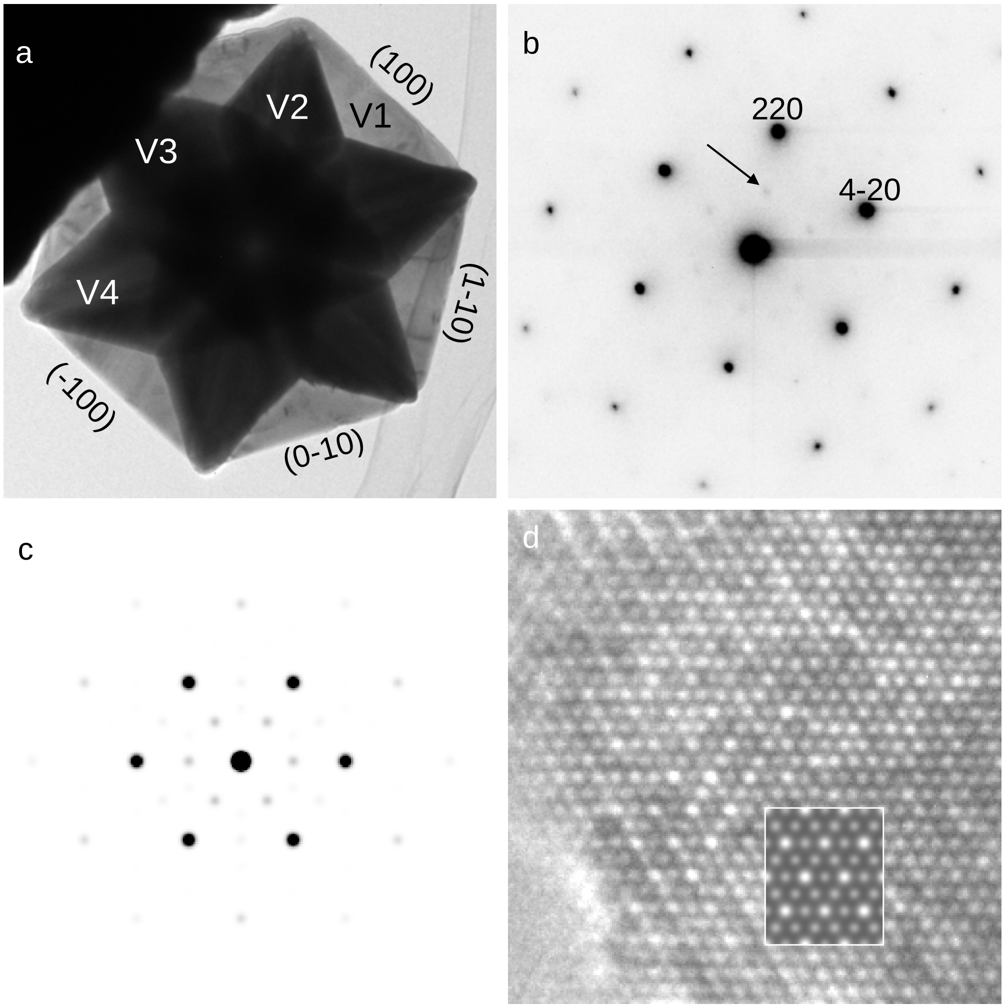

Figure 4.4. (a) Morphology a of concaved cuboctahedron viewed along the normal of V1 plate. (b) Selected-area diffraction pattern of V1. (c) Calculated diffraction pattern based on the ordered Li_xCoO_2 structure with the occupancy of Li1 being zero. (d) High resolution image from the edge of V1. The inset is the simulated image using the same model as used in calculation for diffraction.

Table1. The atomic position and occupancy of the cuboctahedron Li_xCoO_2

	x y z	Occupancy
Li1	0, 0, 0	<1, depending on x
Li2	0.5, 0, 0	1
Co1	0, 0, 0.5	1
Co2	0.5, 0, 0.5	1
O1	0, 0, 0.2402	1
O2	0.5, 0.5, 0.2402	1

of a 2*2 superstructure on the *ab* plane of Li_xCoO_2. Fig. 4.4d shows the high resolution image on the edge of the V1. The superlattice is not homogeneous, with some domains being random ordered. Based on the calculation of the diffraction intensity simulations and the high resolution images, the superlattice is tentatively ascribed to the vacancies of Li (or H on Li site) in Li_xCoO_2. This is caused probably either the incompletion of Li-Co exchange or the side reaction of H-Co exchange. The super structure of the Li_xCoO_2 is determined as rhombehedral with space group of R-3m and $a=2a_0$ and $c=c_0$, where a_0 and c_0 are the lattice parameters of $LiCoO_2$. The atomic positions are listed in Table 1. Fig 4.4c shows the simulated diffraction pattern along $[001]_H$ zone axis based on this model and the simulated atomic image is shown as the inset in Fig. 4.4d.

$LiCoO_2$ is known to have a layered, hexagonal lattice. However, the concaved cuboctahedrons show an overall cubic symmetry. How do the four hexagonal plates combine together to form a cubic symmetric crystal? A 4-fold twinning mechanism is proposed from the crystallographic point of view and proved by careful electron diffraction work discussed below.

CoO, which is proposed to be the parent phase, has a point group of m-3m, which has four 3-fold axes. In contrast, $LiCoO_2$ has a point group of -3m, which has only one 3-fold axis. The transformation of CoO to Li_xCoO_2 must result in the loss of three 3-fold axes, e.g. [11-1], [1-11] and [-111] 3-fold axes, only one 3-fold axis, e.g. the [111] 3-fold axis, remaining. $LiCoO_2$ has an equal probability of being generated with its unique 3-fold axis (the c axis in a hexagonal lattice) being along the [111], [11-1], [1-11] or [-111] axes of the parent phase (CoO). Thus, four twin variants can grow off the parent CoO crystal at the same time. The angles between any two of the *c*-axes of the four variants should all be 70.5º, which is the angle among {111} in a cubic lattice. In the morphology images of the concaved cuboctahedrons, the angles among the hexagonal plates have been measured to be 70.5º. This is not a visual coincidence. Rather it can be proved by following electron diffraction results.

The lattice of $LiCoO_2$ can also be described by a rhombohedral unit cell with a~8.00 Å and α~89.88º. This unit cell is only slightly different from a cubic unit cell with α being only 0.12º smaller, so that the subtle d-spacing or angle change or spot split expected for the twin variants may not be distinguishable in the SADP due to the limitation of the resolution of the TEM facility. However, based on the different extinctions between the SADPs along the real 3-fold and the pseudo-3-fold axes, we can verify the existence of the twins. Fig. 4.5 shows the image and SADPs of a cuboctahedron $LiCoO_2$ crystal. The SADP shown Fig. 4.5b, c and d are taken from different area indicated by the circles and arrows in Fig. 4.5a respectively, without changing the tilting. Pattern c and d can be indexed as a diffraction pattern of $LiCoO_2$ along zone axis [100] for plate V1 and [-100] for plate V2, respectively. Thus, c axes of V1 and V2 twin variants are determined, as labeled in the figure. The angle between the *c* axes of V1 and V2, which is also the angle between the *c** axes of their reciprocal lattice, is measured to be 70.5º. This is consistent with the angle among the {111} planes expected for a cubic system. Now it can be concluded that the concaved cuboctahedron consists of four hexagonal plates, with each plate being a twin variant.

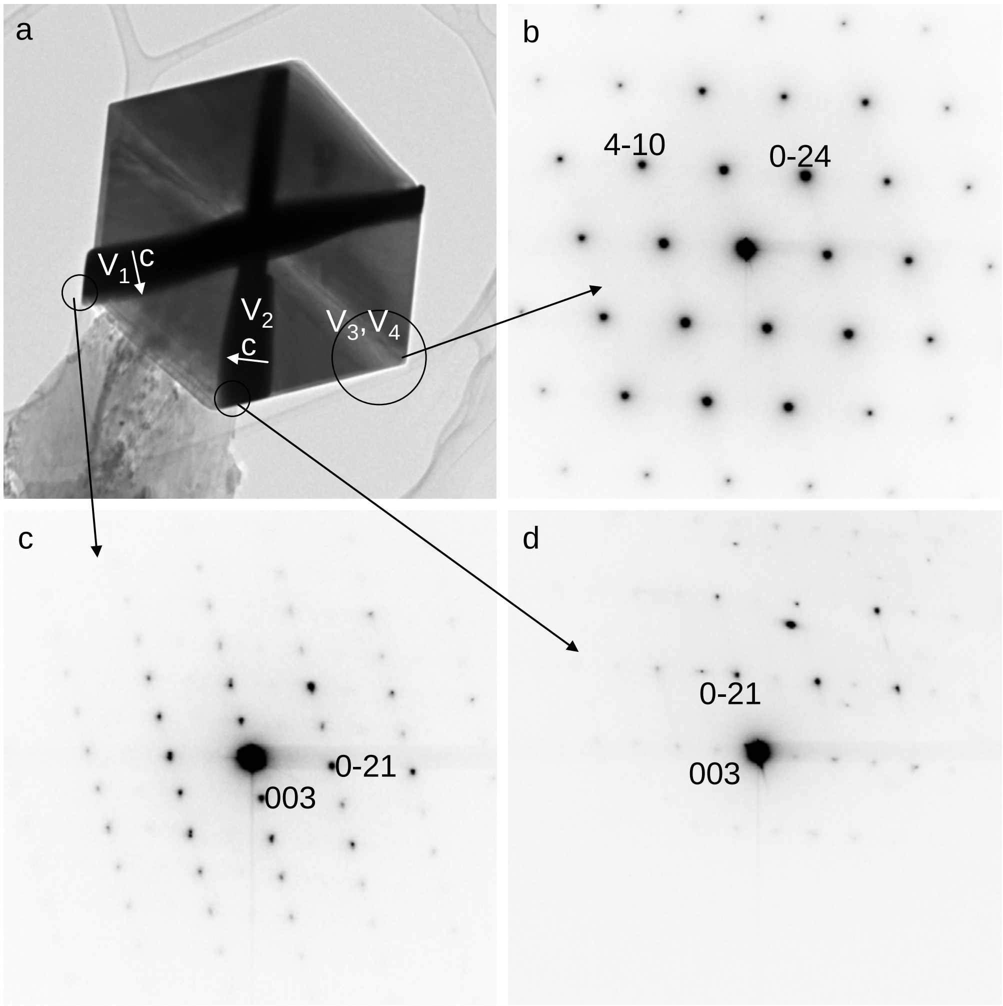

Figure 4.5. (a) Morphology of concaved cuboctahedron viewed along the [100]V1 (or equivalent [-100]V2, or [142]V3). (b-d) SADPs taken from the different twin variants of $LiCoO_2$, (b) [142]V3. (c) [100]V1 and (d) [-100]V2.

The plate normal is the c axis (the 3-fold axis) of the variant.

To further prove this proposed $CoO \rightarrow LiCoO_2$ scenario, nano-CoO prepared by decomposition of commercial $Co(OH)_2$ was used as starting material instead of $Co(NO_3)_2$ in the hydrothermal synthesis. The particle size of this nano-CoO is about 50 nm. After 48 hours reaction at 200°C and following washing and drying, the final products show a mixture of $LiCoO_2$ as the major phase with $Co(OH)_2$ and Co_3O_4 as minor phases. Many more cuboctahedrons are seen in this sample. The appearance of the Co_3O_4 phase is due to two possible oxidizing reactions of CoO competing under this condition, the final products of these two mechanisms being Co_3O_4 and $LiCoO_2$.

Systematic experiments were done to optimize the yield of $LiCoO_2$ and the cuboctahedrons by varying synthesis parameters such as temperature, heating time, concentration/amount/ratio of the starting materials, etc. The results show that the rate of the CoO to $LiCoO_2$ reaction strongly depends on concentration of Li^+. When the LiOH concentration is reduced, less $LiCoO_2$ phase is formed in the final products and much less or even no cuboctahedrons are seen. This is easy to be understood, as that the increased Li^+ concentration moves the equilibrium of $Co_3O_4 \leftrightarrow CoO \leftrightarrow LiCoO_2$ to the right side. The rate of the CoO to Co_3O_4 reaction, however, depends mostly on the amount of water. When less water is used as a solvent, less Co_3O_4 phase and more $LiCoO_2$ phase are formed, and correspondingly, more cuboctahedrons are seen. The reason of this dependency is not clear yet, but it may be due to the fact that water functions as the oxidizing reagent in the reaction of CoO to Co_3O_4 . Water is much more oxidizing under the 200°C hydrothermal conditions than at atmospheric pressure and at room temperature, especially at high pHs [10]. Thus the presence of more water will very likely move the equilibrium of $Co_3O_4 \leftrightarrow CoO \leftrightarrow LiCoO_2$ to the left side.

Many other Co sources were tested as the starting material of this synthesis, such as commercial CoO and $Co(OH)_2$, the particle size of which are about 5 μm and 20 μm respectively. However, very few cuboctahedrons are seen in the products from either one of these starting materials. This implies that the size of the CoO parent crystal is actually crucial in this reaction. Much higher yields of the cuboctahedrons were observed when a lab-synthesized nano-$Co(OH)_2$ was used instead of CoO as the cobalt source. The nano-$Co(OH)_2$ was prepared from a $Co(NO_3)_2$-LiOH titration and the average particle size is about 10 nm. When this nano-$Co(OH)_2$ was used as starting material and minimum amount of water (5 ml, Li:H_2O molar ratio~1:7) was used, phase-pure $LiCoO_2$ product was obtained after heating at 200°C for 48 hours, with the cuboctahedrons representing the overwhelming morphology, as shown in Fig. 4.6a. Fig 4.6b shows a large region of the same sample in a lower magnification, in which very uniform cuboctahedron crystals are seen. In this reaction, the real precursor is still CoO but with even smaller particle size and higher reactivity than the nano-CoO precursor previously used, since it is formed in situ by decomposition of the nano-$Co(OH)_2$. The XRD pattern of this sample is shown in Fig. 4.7 with the corresponding Rietveld refinement. Only trace amount of the Co_3O_4 phase is seen, as indicated by an arrow in the figure. Cell parameters of a=b=2.81465(2), c=14.04655(6) Å are extracted from the refinement, which are within the range expected for

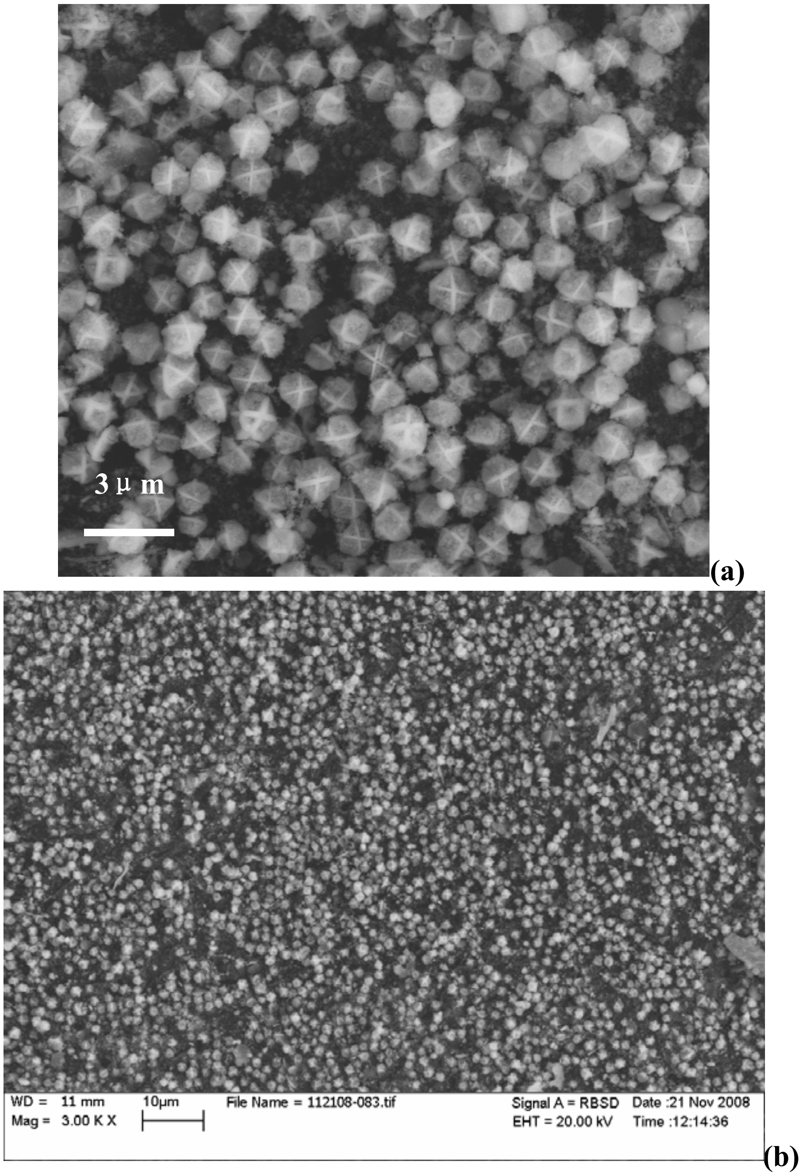

Figure 4.6. (a) Small scale and (b) large scale SEM image of pure-phased $LiCoO_2$ with cuboctahedron morphology.

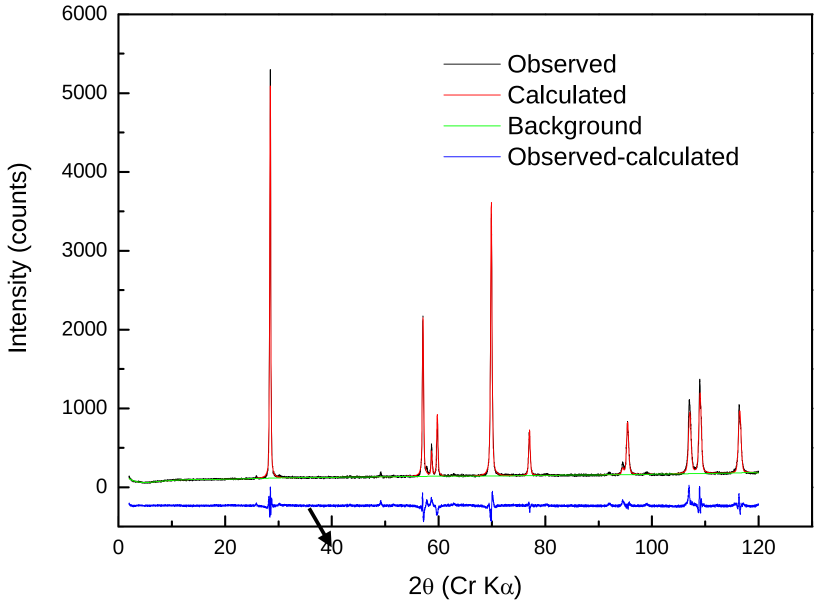

Figure 4.7. The XRD pattern and Rietveld refinement of the high yield cuboctahedron $LiCoO_2$. The black arrow indicates the characteristic reflection of Co_3O_4 impurity.

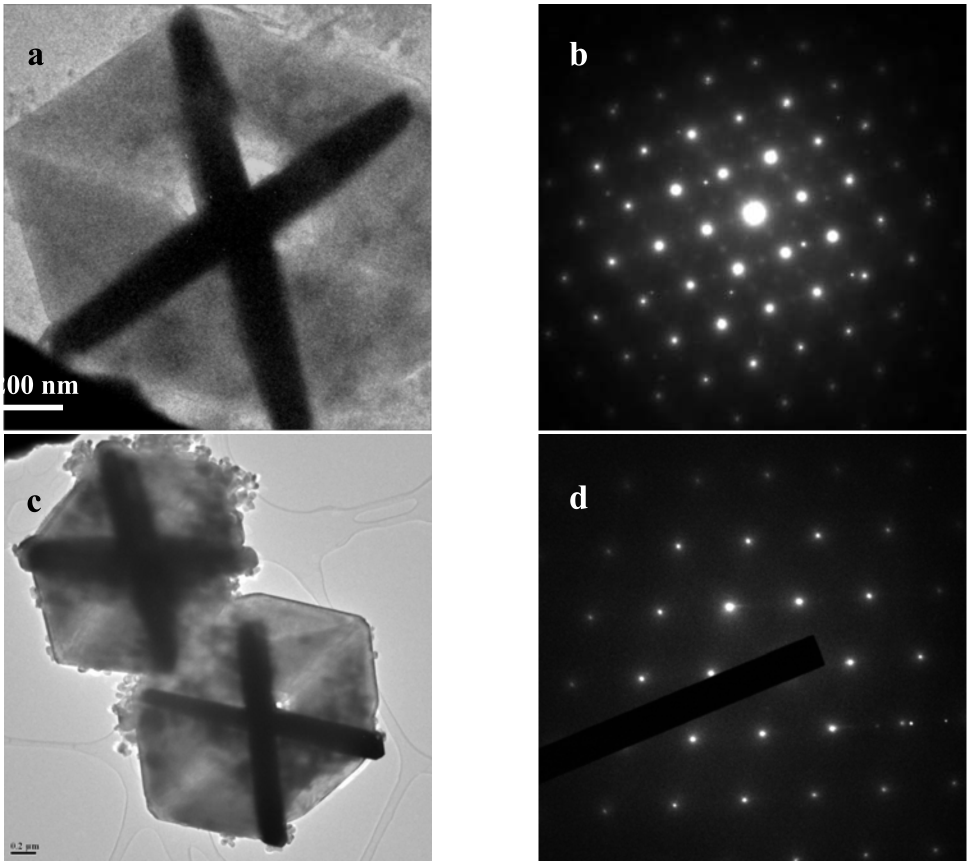

Figure 4.8. (a) Morphology of not fully ion-exchanged Li_xCoO_2 concaved cuboctahedra, and (c) stoichiometric $LiCoO_2$ concaved cuboctahedra. Scale bars in (a) and (c) are 200 nm. (b) and (d) are SAD patterns on the particle shown in (a) and (c) along the $[124]_H$ zone axis, respectively.

stoichiometric micrometric $LiCoO_2$ [11]. The result of direct coupled plasma (DCP) analysis shows that the Li:Co ratio in this sample is 1.05(±0.05):1. The ^{7}Li MAS NMR spectrum of this sample contains, besides the diamagnetic resonance at 0 ppm, no extra resonances due to Li-excess or Li-deficiency. All these results together suggest that this concaved cuboctahedron $LiCoO_2$ is very stoichiometric. Correspondingly, there should be no more superstructures due to Li-deficiency in this high yield sample. Fig 4.8 shows the SAD patterns of the samples from the first route ($Co(NO_3)_2$ as the starting material) and the high yield route (nano-$Co(OH)_2$ as starting material). The weak spots that appear in Fig. 4.8 b indicating the presence of the superstructure is not seen in Fig 4.8d. The presence of the superstructure in the first route synthesized sample is possibly due to higher water content in the system, which may induce H-Li or H-Co exchange in the $LiCoO_2$ like regions.

The mechanism for growth then can be summarized as follows: a mother crystal of CoO, no matter what shape it is in, is pitted from all 6 [100] directions equivalently. At the same time, due to high concentration of Li^+ in the aqueous phase, Li^+ starts inserting into the CoO lattice along all {111} planes by exchanging with Co^{2+}. Correspondingly, upon one Li^+ insertion/exchange, one Co in the neighboring layer is oxidized to Co(III) to maintain charge neutrality. Since Co(III) is much more stable and less soluble in the basic solution, the Co(III) layer is then stabilized by the Li insertion. This creates a 2-D channel between two Co(III) layers, where Li can keep exchanging with Co(II) until it reaches the center of the mother CoO crystal. This is not a simple ion-exchange mechanism but must involve a simultaneous oxidation reaction. It can be called an oxidizing-ion-exchange reaction. After all the {100} faces been pitted, other faces, such as the {110} and {111} faces, will also be pitted to form a fully concaved cuboctahedron shape. At the same time, Co(II) in the solution, largely in form of $Co(OH)_4^{2-}$ will also be oxidized to Co(III) and re-precipitate together with Li^+ and OH^- on the surface of new formed $LiCoO_2$-like region, growing along the $[001]_H$, $[010]_H$ and $[110]_H$ directions, as observed in our previous study. Finally the combination of pitting and growth occurring together, a mother CoO crystal gradually adopts a concaved cuboctahedron shape. Fig. 4.9 shows the proposed pitting and growth of the cuboctahedrons.

In fact, the real growth process is much more complicated than this: The parent CoO crystals do not have to be in a regular shape like shown in Fig. 4.9 and the pitting and growth process occurs in parallel (for simplicity, Fig. 4.9 shows these process in series with pitting occurring first). Irregular intermediate morphologies are expected before the particles finally grow into the regular concaved cuboctahedron shape. Fig. 4.10 shows two examples of the intermediate morphologies, where the crystals are heavily leached but not yet in a concaved cuboctahedron shape.

The fact that all the cuboctahedrons are perfectly symmetrical regardless of the shape of the mother CoO nanocrystals is ascribed to the very small size of the mother CoO particle and the high surface energy on its edges. If one of the 4 pieces of $LiCoO_2$ plates, V2, as schematically drawn in Fig. 4.10 (for clarity, only two plates are shown) is smaller than the other plate V1, then on the region where the edges of these plates penetrate each other, as indicated by a black arrow in the figure, a

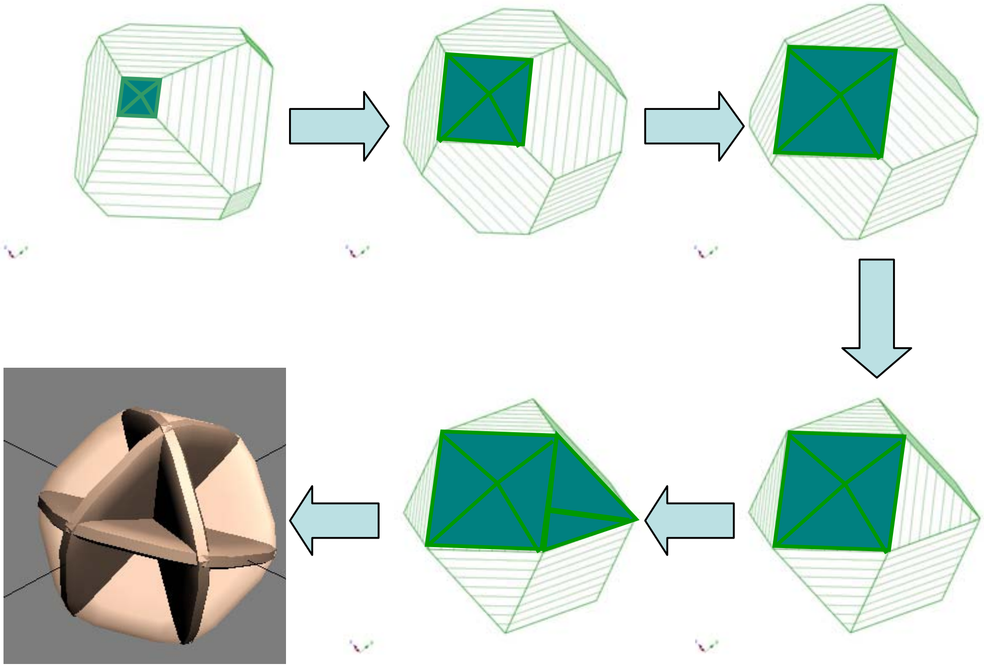

Figure 4.9. Growth mechanism of the concaved cuboctahedron. The parts shown in darker color represents the leached planes. For clarity, only one plane for each type is shown.

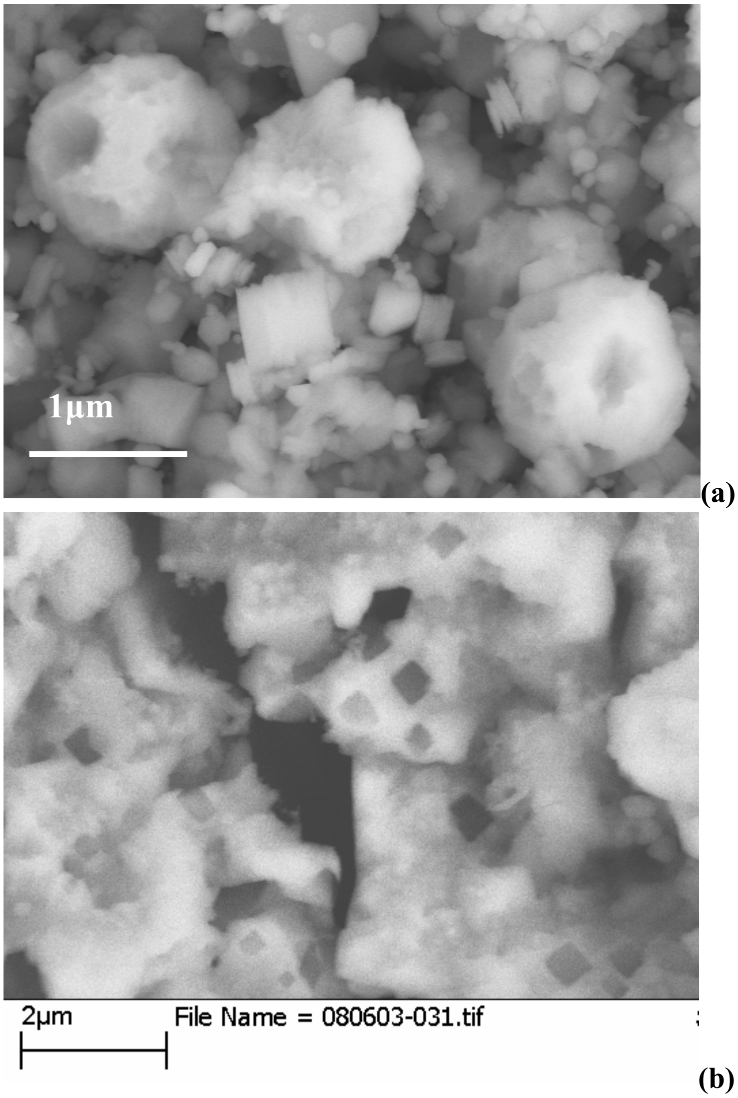

Figure 4.10. SEM images of particles in intermediate morphologies between the cubic precursor and the concaved cuboctahedron product.

concaved “V” shape is formed. This will cause quick growth at the bottom of the “V” which is followed by fast growth of other parts on the edge of V2, until eventually V2 becomes the the same size as V1 (and other two plates). Thus the “V” vanishes and the out surface of the particle is rounded, and correspondingly, the four plates are exactly the same size.

Although this concaved shape is not ideal for creating a high density compact of the cathode and will be not good for the volumetric power density. However, its unique morphology may benefit to the performance of LIBs. For example, the twinned crystal makes $LiCoO_2$, a layered 2-D Li conductor, a pseudo 3-D conductor with all the twinning plates are physically and electrically connected inside. It could efficiently improve the high rate performance of $LiCoO_2$. This effect has been shown by the desert rose form of $LiCoO_{2,}$, as discussed in Chapter 3.

The electrochemical performance of the phase-pure concaved coboctahedron $LiCoO_2$ was tested in coin cells. Fig 4.12 shows its charge-discharges curves at ~ 1C rate between 2.5-4.3 V of the first three cycles. The first discharge capacity is about 108 mAh/g, lower than the practical capacity of $LiCoO_{2.}$ However, many reasons can cause the low capacity, for example, high over-potential was observed in cycling of the cells, which may be one reason for the low capacity. This indicates high resistance of the cell, possibly related to the surface status of the sample. High temperature annealing or surface modification may be required for this sample to show good rate performance possibly expected for this morphology. Optimization of the electrochemical performance of this cuboctahedron $LiCoO_2$ is still in study.

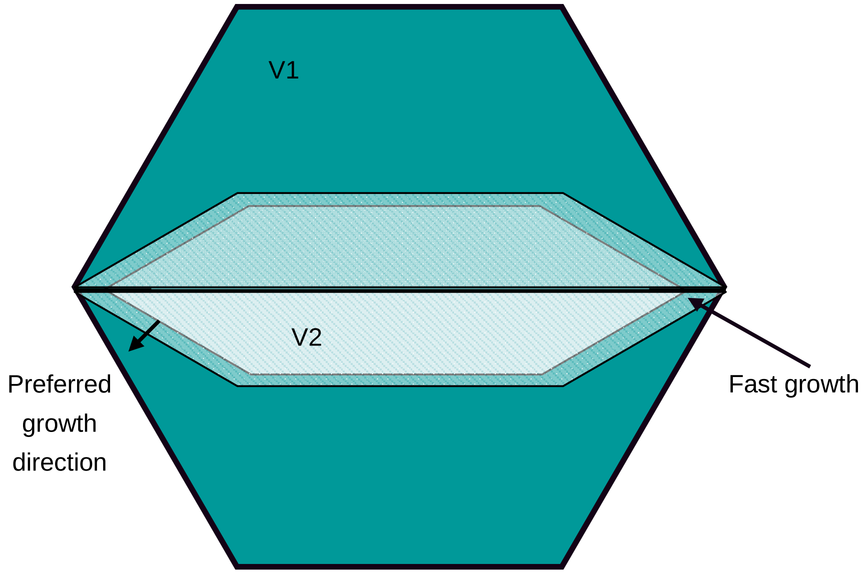

Figure 4.11. The schematics showing the isotropic growth of the concaved cuboctahedrons.

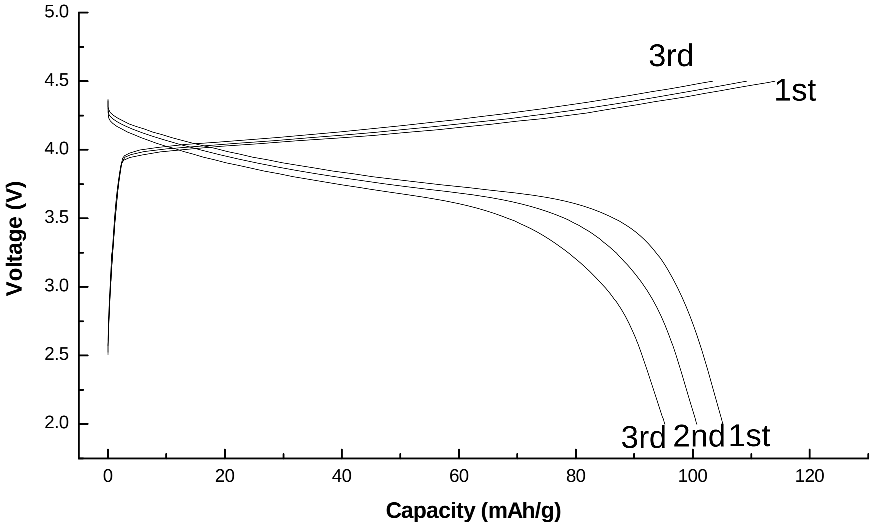

Figure 4.12. Charge and discharge of the cuboctahedron $LiCoO_2$.

The synthesis of this unique $LiCoO_2$ reveals a very interesting topological reaction basically due to the lattice similarity of bivalent transition metal oxide and their trivalent, lithiated form. It is very possible that this kind of reaction is not limited to $LiCoO_2$ only. Similar concaved cuboctahedrons have been observed in the products from using Fe, Mn and Ni doped $CoO/Co(OH)_2$ as starting materials, but the yield is much lower, since this kind of reaction is sensitive to many factors and optimization work is required for each specific starting material combination. Fig. 4.13 shows image of concaved cuboctahedrons in the products and their corresponding energy dispersive X-ray spectroscopy (EDX) results (the scanning beam was focused on the particle) when $MnCo(OH)_4$ and $NiCoMn(OH)_6$ are used as starting materials. Although due to that the Mn and Ni solubility in this kind of twinned $LiCoO_2$ may be not as large as those shown in $LiMn_{0.5}Co_{0.5}O_2$ and $Li(Ni_{1/3}Co_{1/3}Mn_{1/3})O_2$ compounds synthesized by other methods, it is not impossible to have some Mn and Ni doping in this concaved cuboctahedron morphology.

Moreover, this twinning mechanism is not limited to cubic to rhombohedral transition either. For example, nanometer sized FeO was used as starting material. The final product is shown by XRD to be $LiFeO_2$, which has a tetragonal lattice. Fig 4.14a shows the typical morphology of this sample. It is different from the cuboctahedrons but also appears to contain twin crystals. As shown in Fig. 4.14b, the angle of 70.5° is seen again between the primary particles. Although in future more TEM and electron diffraction work needs to be done to confirm the twin structure in this sample, it is plausible that this morphology is ascribed to similar oxidizing-ion-exchange mechanism and the transformation of cubic FeO to twinned tetragonal $LiFeO_2$. These results open new possibilities of tuning the morphology of crystals by systematic crystal engineering work.

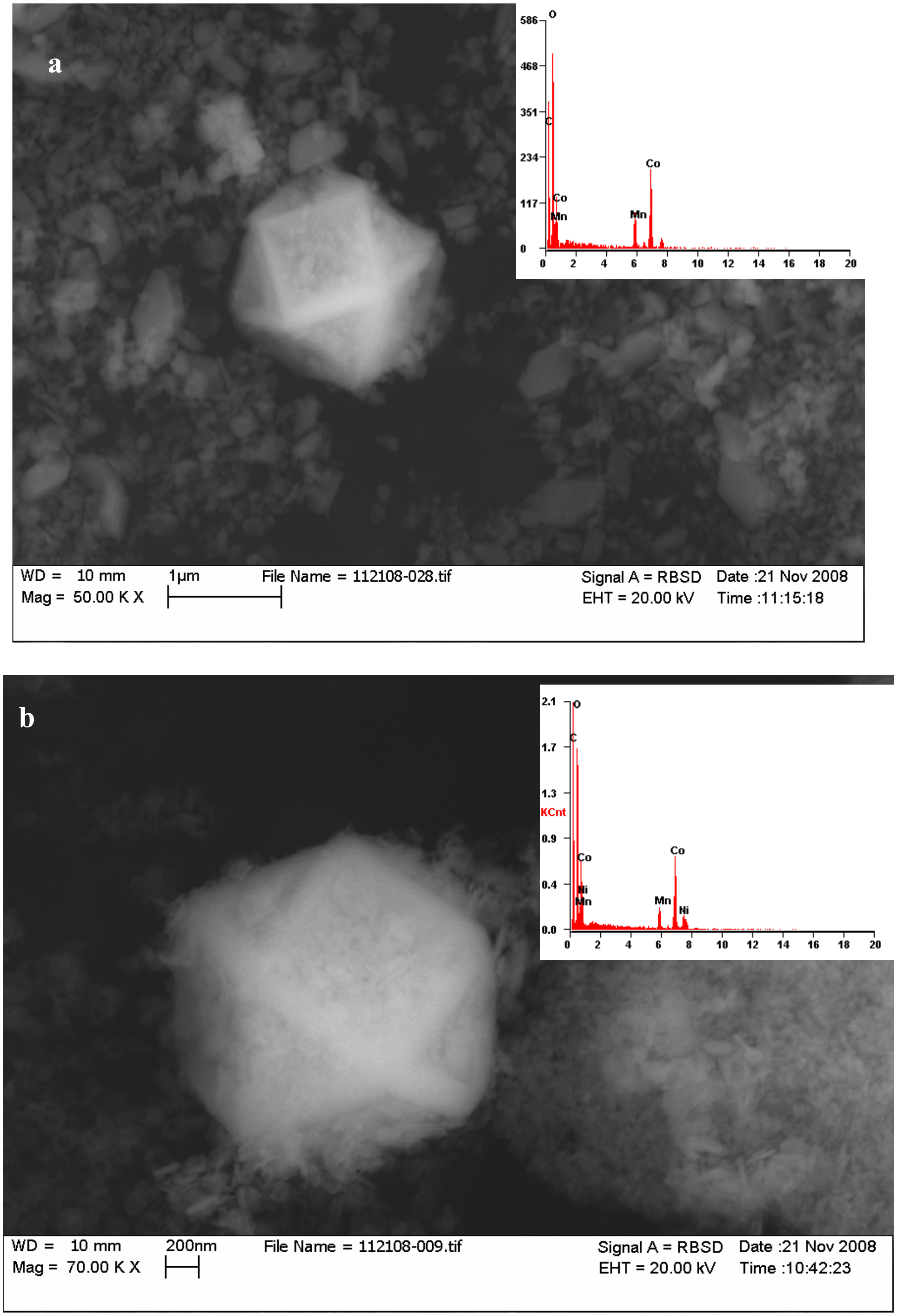

Figure 4.13. SEM image of concaved cuboctahedra found in the products of the hydrothermal synthesis when (a) $CoMn(OH)_2$, (b) $NiCoMn(OH)_6$ are used as starting material and the corresponding EDX results. Both samples were synthesized at 200°C for 24 hours.

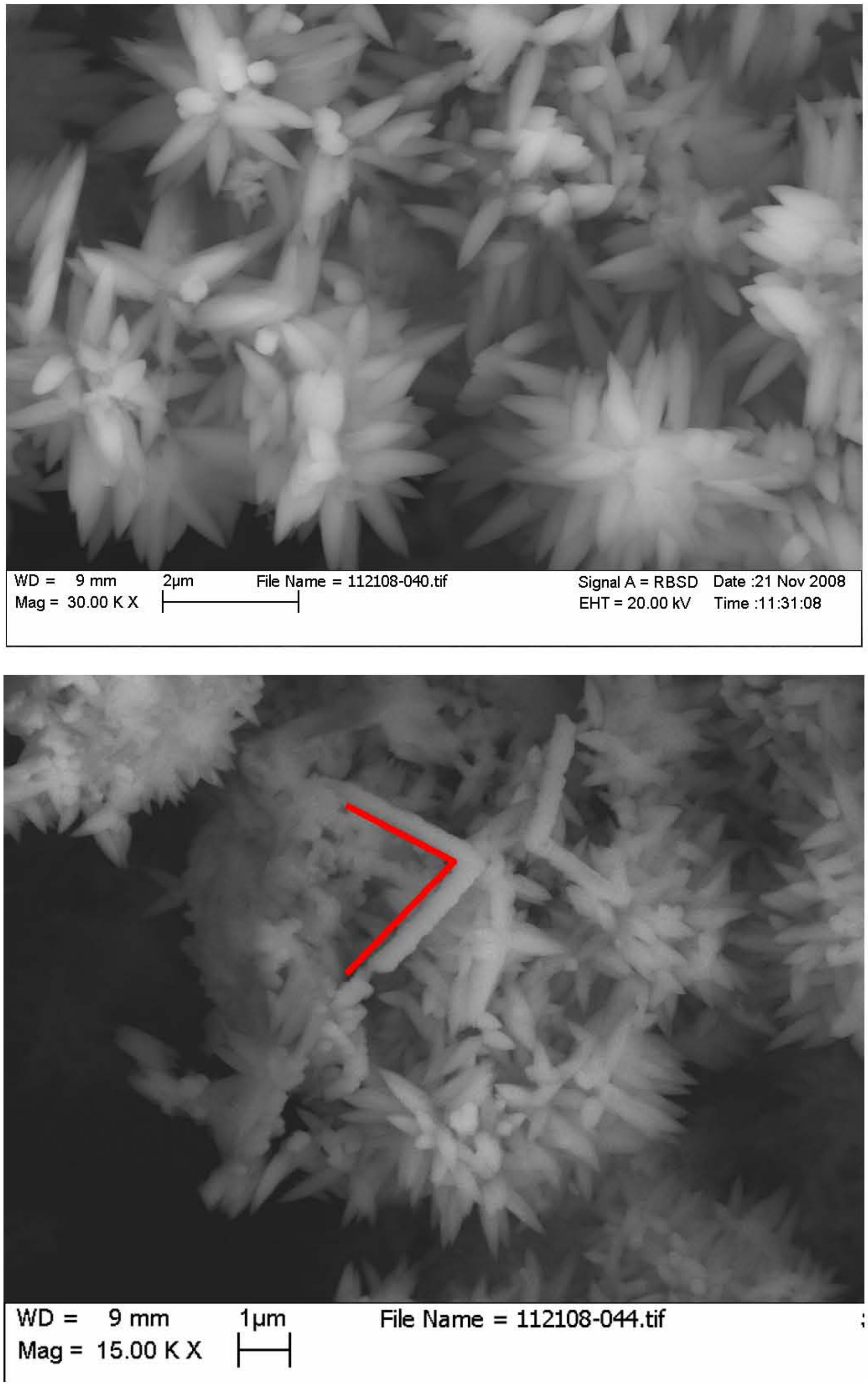

Figure 4.14. SEM images of LiFeO$_2$ synthesized by hydrothermal method. The angle labeled in (b) is about 71º.

4. CONCLUSIONS

In the work discussed above, an extremely unique and beautiful morphology, the concaved cuboctahedrons, is obtained for the first time for a layered compound, $LiCoO_2$. This morphology is also only reported for the second time other than CuS. However, in the work of CuS [8], in which this morphology was the first time reported, the growth mechanism was not explained with any supporting experimental evidence. Here an oxidizing-ion-exchange and isotropic growth mechanism is proposed for the first time based on chemical and crystallographic possibilities to explain the formation of the morphology for $LiCoO_2$ and is proved by using a series of analytical techniques. Near 100% yield was archived by optimizing the starting materials and synthesis conditions following this growth mechanism. This result not only reveals a new topological reaction, but also opens new possibilities of designing the morphology of crystals by utilizing the difference of symmetry between the precursor and the products.

REFERENCES

1. Jang, D. H.; Shin, Y. J.; Oh, S. M. *J. Electrochem. Soc.* **1996,** *143*, (7), 2204-2211.
2. Xia, Y. Y.; Zhou, Y. H.; Yoshio, M. *J. Electrochem. Soc.* **1997,** *144,* 2593-2600.
3. Chung, S. Y.; Bloking, J. T.; Chiang, Y. M. *Nat. Mater.* **2002,** *1*, (2), 123-128.
4. Huang, H.; Yin, S. C.; Nazar, L. F. *Electrochem. Solid State Lett.* **2001,** *4*, (10), A170-A172.
5. Yamada, A.; Chung, S. C.; Hinokuma, K. *J. Electrochem. Soc.* **2001,** *148*, (3), A224-A229.
6. Islam, M. S.; Driscoll, D. J.; Fisher, C. A. J.; Slater, P. R. *Chem. Mater.* **2005,** *17*, (20), 5085-5092.
7. Nishimura, S.; Kobayashi, G.; Ohoyama, K.; Kanno, R.; Yashima, M.; Yamada, A. *Nat. Mater.* **2008,** *7*, (9), 707-711.
8. Wu, C. Y.; Yu, S. H.; Antonietti, M. *Chem. Mater.* **2006,** *18*, (16), 3599-3601.
9. Vayssieres, L.; Keis, K.; Hagfeldt, A.; Lindquist, S. E. *Chem. Mater.* **2001,** *13*, (12), 4395.
10. Lobachev, A. N. Crystallization processes under hydrothermal conditions. **1973**.
11. Okubo, M.; Hosono, E.; Kim, J.; Enomoto, M.; Kojima, N.; Kudo, T.; Zhou, H. S.; Honma, I. *J. Am. Chem. Soc.* **2007,** *129*, (23), 7444-7452.

CHAPTER 5

Li Transport in the Battery – an *In Situ* ^{7}Li Static NMR Study

Hailong Chen, Rangeet Bhattacharyya, Baris Key, Clare P. Grey

Department of Chemistry

Stony Brook University, Stony Brook, NY 11794-3400

ABSTRACT

^{7}Li MAS NMR spectroscopy as a powerful analytical tool to study the local structure of cathode and anode materials has been demonstrated and discussed in previous chapters. However, since many of the reactions occurring in the batteries are too quick to be captured by *ex situ* experiments, it is desired to monitor *in situ* and in real time the structural changes of the electrodes during the electrochemical cycling. This chapter describes the use of a solid state NMR experiment system that allows *in situ* observation of the resonances of each component of the battery (the cathode, the anode, and the electrolyte) and its application to $LiCoO_2$. Static ^{7}Li NMR spectroscopy, combined with deconvolutional fitting, is used to provide information on the local structure of the electrodes. Commercial (micrometer sized) $LiCoO_2$, laboratory-synthesized $LiCoO_2$ nanoparticle, and the "desert rose" $LiCoO_2$ are studied, and their rate capabilities are compared.

1. INTRODUCTION

The Li diffusion in a battery system is considered a very important issue and has been studied intensively. Commonly used methods include potential intermittent titration technique (PITT) and galvanostatic intermittent titration technique (GITT) [1-4]. However, these methods are indirect measurements and depend largely on the construction of the cell and the equivalent circuit used in the analysis of the data.

NMR has been proved to be a powerful tool for detecting ion mobility in solids and solutions. The Li self-diffusion coefficient (D_s) in various organic solvent-based liquid electrolyte systems has been studied by field gradient NMR. For example, the D_s of Li in $LiPF_6$-PC electrolyte varies from 1.32×10^{-10} m^2/s to 2.04×10^{-10} m^2/s, depending on different concentrations [5]. The D_s of Li in $LiPF_6$-EC/DMC (2:8) system was reported to be in the order of 10^{-10} m^2/s [6]. Mulder and Wademaker et al. also demonstrated that the diffusion coefficient and site activation energy of Li in Li_xTiO_2 system could be directly measured and calculated by using 2D-exchange NMR [7, 8].

However, a real LIB system is very complicated. The rate of the electrochemical reactions are controlled not only by the diffusivity of Li in each component, but are also affected by many other factors, such as the Li exchange on the interface between the electrodes and the electrolyte, the Li concentration induced polarizations, and the over potentials. To understand the Li transport property and the kinetics of electrochemical reactions in a battery, it is necessary and important to monitor the battery system *in situ* and in real time. Letellier and coworkers have shown that it is possible to collect NMR signal while the cell is functioning for Li-carbon cells [9, 10]. This method has been applied to Si [11]. As the first step of the attempts to apply this technique to more electrode materials and battery systems other than the Li-silicon system, a Li-$LiCoO_2$ system is chosen as a model system for investigation. Some of the preliminary results of this system will be discussed.

2. EXPERIMENTAL

2.1. Preparation of the *in situ* pouch-cell

Due to the fact that the presence of large amount of metal in the bore of the magnet can change the homogeneity of the magnetic field, for an *in situ* cell, as few as possible metal components should be used. In an *in situ* cell, a plastic bag is used to seal the battery and make it airtight, a copper mesh (for the anode) and a aluminum mesh (for the cathode) are used as the current collectors instead of copper and aluminum foil. Correspondingly, the assembly of the cathode is not by using usual doctor-blade method. Instead, the cathode is made by pressing a solid mixture of active material, carbon black (or carbon super P, as conductive additive) and powder of polytetrafluoroethylene (PTFE) on the aluminum mesh. Similarly, a thin Li foil is pressed on the copper mesh as the anode. A glass fiber, instead of normally used Celgard membrane, is used as the separator as it can hold more liquid electrolyte in between the electrodes. Fig 5.1 shows the schematics of an *in situ* pouch-cell where Si is used as the other electrode against Li [11]. The typical size of the main part (excluding the extending out meshes) of an *in situ* cell is about 12mm*5mm*3mm (length*width*thickness).

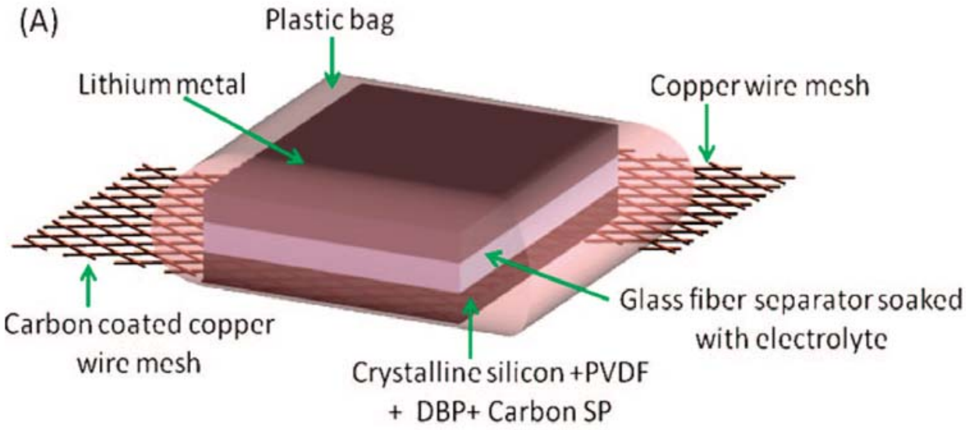

Figure 5.1. The schematics of an in situ pouch-cell. Reproduced from reference [11].

2.2. Setup of the *in situ* static NMR system

The as-prepared *in situ* pouch-cell was first inserted into the coil of a 5 mm CMX static NMR probe. Then the two current collectors, the Cu mesh and the Al mesh were connected to an Arbin electrochemical cycler through well shielded BNC cables and the probe was carefully loaded up into the bore of a 4.7 T magnet, with the connection to the cycler remaining. Fig. 5.2 shows the schematics of the in situ NMR system. To get a good signal/noise ratio, good grounding of the probe is required. To avoid the noise in the radio frequency RF range from the cycler going into the probe and disturbing the NMR signal, a low pass filter is used between the cell and the cycler. In the first several experiments, the electrochemical cycling and NMR pulsing and signal collecting were started and synchronized manually. In an upgraded system, the synchronization of the electrochemical cycler and the NMR console can be controlled by program through the hardware communications between the two facilities.

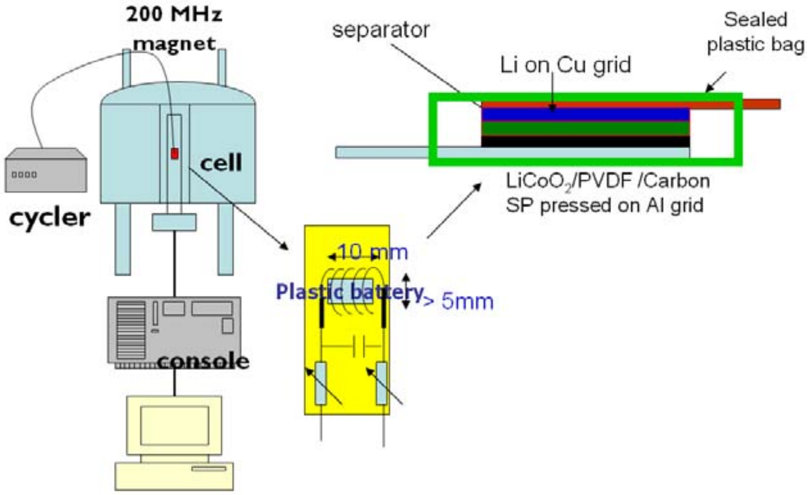

Figure 5.2. The schematics of the used *in situ* NMR-electrochemical cycling system.

3. RESULTS AND DISCUSSION

As many of the Li-containing cathode materials of LIBs are paramagnetic compounds, not all of them are readily observed in static ^{7}Li NMR, as the signal may be too broad to be detectable. The feasibility of the cathode materials to this experiment depends on many factors, such as the T_1 (spin-lattice relaxation) and T_2 (spin-spin relaxation) relaxation times of their resonances. $LiCoO_2$ is one the cathode materials that gives relative narrow and strong signals in static mode. Moreover, based the results of *ex situ* ^{7}Li magic angle spinning (MAS) NMR, which was discussed in Chapter 1, the intensity and position of characteristic “Knight-shifted” resonance of charged Li_xCoO_2 can be used as quite good variables to monitor not only the structural changes but also the state of charge of Li_xCoO_2. By studying a Li-$LiCoO_2$ battery in the *in situ* NMR system, some useful information can be obtained to help answer some important questions including when the “Knight-shifted” peak first occurring and how the battery self discharges, etc.

In the *in situ* cells we used, two $LiCoO_2$ materials were used, the commercial, micrometer sized $LiCoO_2$ and the lab-synthesized, “desert rose” form $LiCoO_2$, which is expected to have higher specific surface area and more capable for high rate cycling than the commercial $LiCoO_2$ (Chapter 3). Fig. 5.3a shows the ^{7}Li static NMR spectra of a Li-“desert rose” $LiCoO_2$ cell upon the first electrochemical cycle at a C/14 rate. The cell was charged to 4.8 V and then discharged to 2V. Single pulse method was used to excite and collect the NMR signals, with a pulse delay of 0.2 s. The spectra were collected every 360 scans, about 2 minutes.

In Fig. 5.3a, three major resonances are seen. The sharp and intense resonance at about 250 ppm is the “Knight-shifted” resonance of Li metal (anode), which is consistent with what reported before. The even sharper resonance at around 0 ppm is ascribed to Li^+ in the liquid phase (the electrolyte) and possibly the diamagnetic Li salts formed from the side reactions, such as LiF, Li_2O, Li_2CO_3, etc, which are mostly located in the solid-electrolyte-interphase (SEI) layers. The broad resonance, centered also at 0 ppm in the first spectrum and shifting to higher ppm during charge, is assigned to be Li in Li_xCoO_2. The gradual shift of the Li_xCoO_2 resonance can be viewed more clearly in Fig. 5.3b.

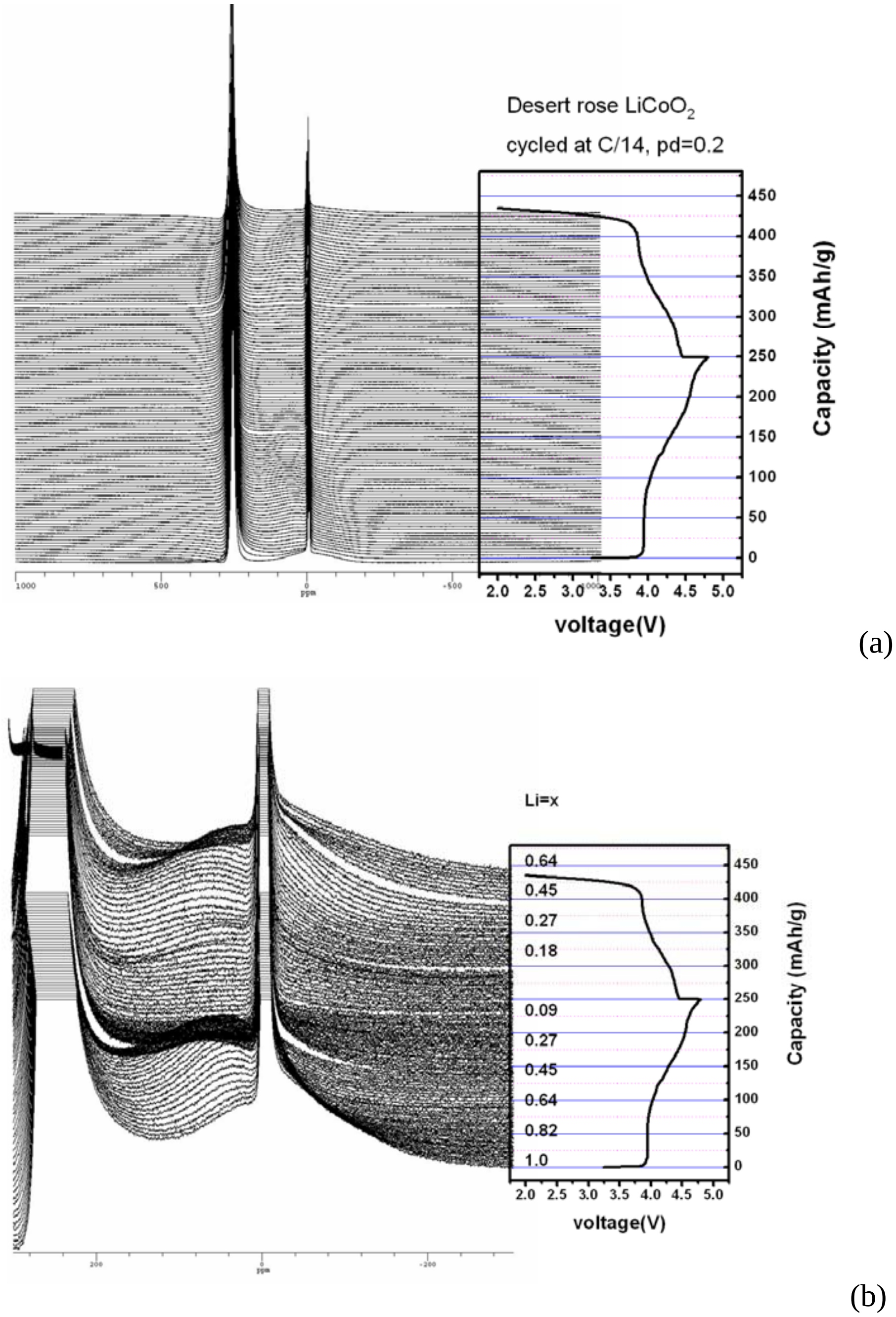

Figure 5.3. (a) The in situ ^{7}Li static NMR spectra of “desert rose” $LiCoO_2$ on the first cycle. (b) The in situ ^{7}Li static NMR spectra of “desert rose” $LiCoO_2$ on the first cycle, zoomed in between 250 to -100 ppm.

As a comparison, the spectra of charged “desert rose” Li_xCoO_2, signals collected *ex situ* after about one hour after stop charging, are shown Fig. 5.4 and the *in situ* static ^{7}Li NMR spectra of commercial $LiCoO_2$ upon cycling at a C/2 rate are shown in Fig. 5.5.

The results of the *ex situ* experiments for “desert rose” Li_xCoO_2 are different from either that reported by Menetrier et al. [] for micrometer sized Li_xCoO_2 and that discussed in Chapter 1 for Li_xCoO_2 nanoparticles. When x>0.7, no Knight-shifted resonance is observed. However, in the *in situ* experiment (Fig 5.3b), the resonance of Li_xCoO_2 starts shifting at the very beginning of the charge. Similarly, the Knight-shifted resonance for commercial Li_xCoO_2 also appears early in the beginning of the charge (Fig. 5.4). The above results imply that the metal insulator transition occurs at the very beginning of the charge for both samples. The reason why the Knight-shifted peak was not seen at the very beginning of the charge in the *ex situ* experiments but visually appeared in the *in situ* experiment may be due to two possible reasons: 1. The self discharge of the batteries during the time after the cell stopped charging and before it was disassembled in the glove box and washed with DMC, which is more pronounced for $LiCoO_2$ with nanoparticle/nanostructures. 2. The inhomogeneity of the cathode material upon charging. It is to say, during charging, especially high rate charging, some of the particles may became metallic and result in the Knight-shifted peak at 60 ppm, while other particles remain pristine, but the overall gravity of the broad peak visually move to higher ppm.

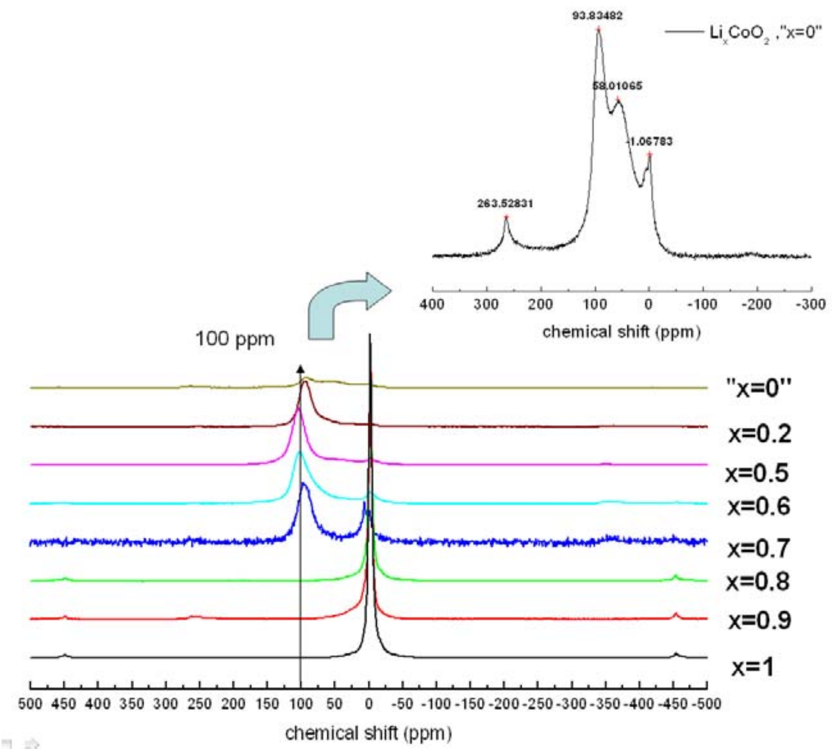

Figure 5.4. The ex situ ^{7}Li MAS NMR spectra of “desert rose” Li_xCoO_2 as function of x. The inset is the zoom-in of the spectrum of “CoO_2” (“x=0”), where nominally all the Li is extracted from $LiCoO_2$, however, still a very small amount of Li left in the lattice due to either the self discharge or the fact that the coulombic efficiency of this system is not 100%.

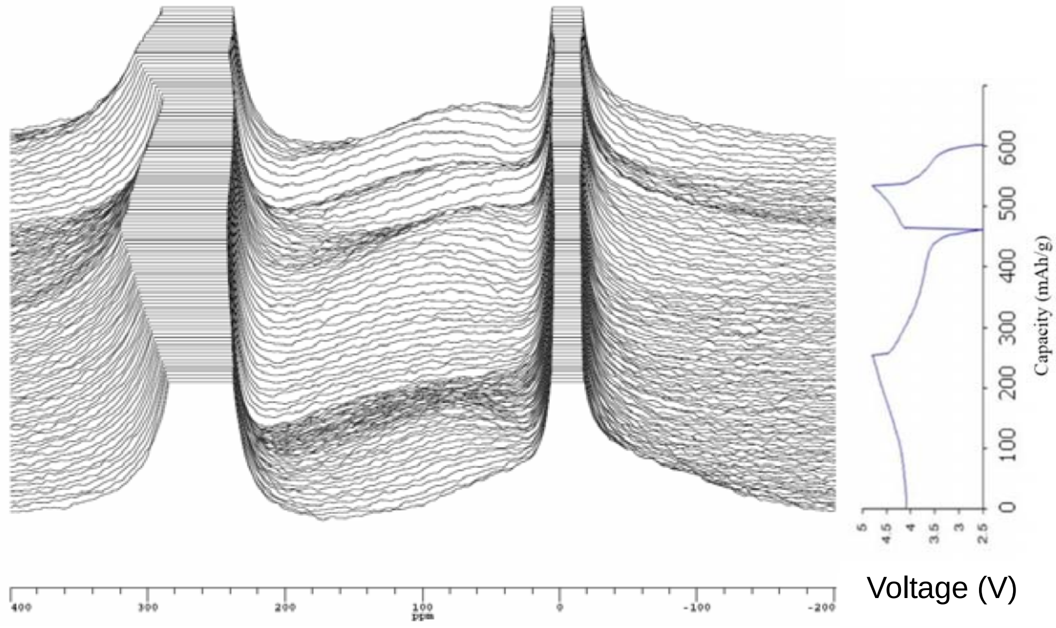

Figure 5.5. The in situ ^{7}Li static NMR spectra of “desert rose” $LiCoO_2$ on the first two cycles at C/2 rate.

As desert rose Li_xCoO_2 is *ex situ* charged to x=0.5, the Knight shifted peak reaches the maximum ppm around 100, which is consistent with the work of Menetrie et al. on micrometer sized $LiCoO_2$. As more Li is extracted, this resonance shifts back towards 0 ppm, and correspondingly, the intensity drops as less Li remains in the structure. The same trend was observed for both commercial and desert rose $LiCoO_2$ in the *in situ* experiments. At the point where nominally all the Li is extracted from desert rose Li_xCoO_2, i.e. x = 0, there are still small amount of Li remaining in the structure and resulting in three resonances at 94, 58 and 0 ppm. The presence of these Li in the lattice is due to either the self discharge or the fact that the columbic efficiency of this system is not 100% (the decomposition/electrochemical oxidation of the solvents in the electrolyte at high voltages). These three resonances were not seen in our *ex situ* experiments for commercial Li_xCoO_2 sample when charged to the same state (x = 0) but was seen for Li_xCoO_2 nanoparticles samples at the same state of charge. This may be due to the different metastable local ordering for nano- and bulk-$LiCoO_2$ at high voltages, but more experiments are required to explain the difference more clearly.

Based on both *ex situ* and *in situ* experiment results, the change of the ^{7}Li resonances of both commercial and desert rose $LiCoO_2$ can be briefly summarized in Table 1.

By using these constrain, the *in situ* NMR spectra for both samples were fitted by using deconvolution method. The intensity of all the resonances, including the resonance from the liquid electrolyte, SEI and Li metal are corrected/adjusted to reduce the error induced by the fact that their T_1 time are longer than the experimental pulse delay. Fig 5.6 shows two examples of the fitting of the spectra. The intensity, broadening and position of the resonances suggested by the results of *ex situ* experiments are adjusted by a program to get the best fit to the experimental data. The fitting results for the first two continuous cycles of a Li-desert rose $LiCoO_2$ *in situ* cell are shown synchronized with the electrochemical curve in Fig. 5.7. The intensity of the Li metal resonance is plotted in blue line. It clearly increases during charge and drops during discharge both linearly, apparently, because the current is constant. The intensity changes of the electrolyte (red line) in within 1% of the total intensity and is considered to be in the range of errors. More complex, but very clearly, the intensity of Li_xCoO_2 resonances follow the charge and discharge current nicely, with the 60 ppm Knight shifted peak intensity increasing at the beginning of the charge and dropping after $x < 0.5$, and correspondingly, the 0 ppm diamagnetic peak ($LiCoO_2$) gradually disappearing at the beginning of the charge and coming back a little bit at the end of the charge. The fact that the changes of the Li_xCoO_2 resonance is not linear as the Li metal signals is due to that the intensity of these resonances does not simply reflect the changes of the population of the Li ions, but also largely affected by how paramagnetic the compounds is. During the discharge the change of the intensity of the $LiCoO_2$ resonances is the reverse of that during the charge but also follows the current well. These results show that it is possible to monitor the *in situ* battery systems not only qualitatively but also quantitatively, although this is just a preliminary attempt and many experimental parameters and the fitting protocols need to be further optimized and improved.

Table 1. $LiCoO_2$ resonances at different state of charge/discharge

State of charge/discharge	Resonances
x>0.75	60ppm (Knight-shifted) and 0 ppm (diamagnetic)
0.75>x>0.5	60-100ppm (Knight shifted)
X<0.5	100-0 ppm (Knight shifted) and 0 ppm

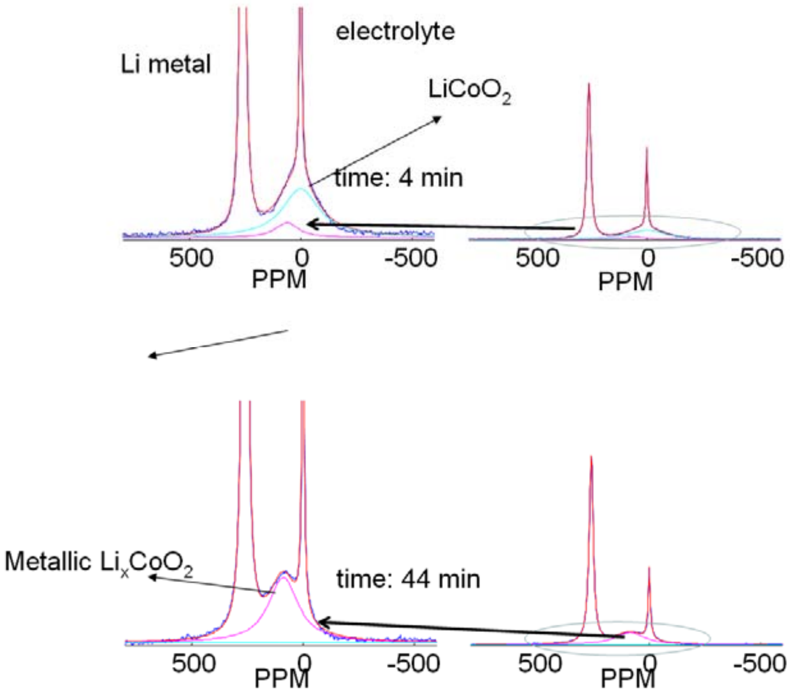

Figure 5.6 Two examples showing the deconvolutional Fitting on the *in situ* spectra

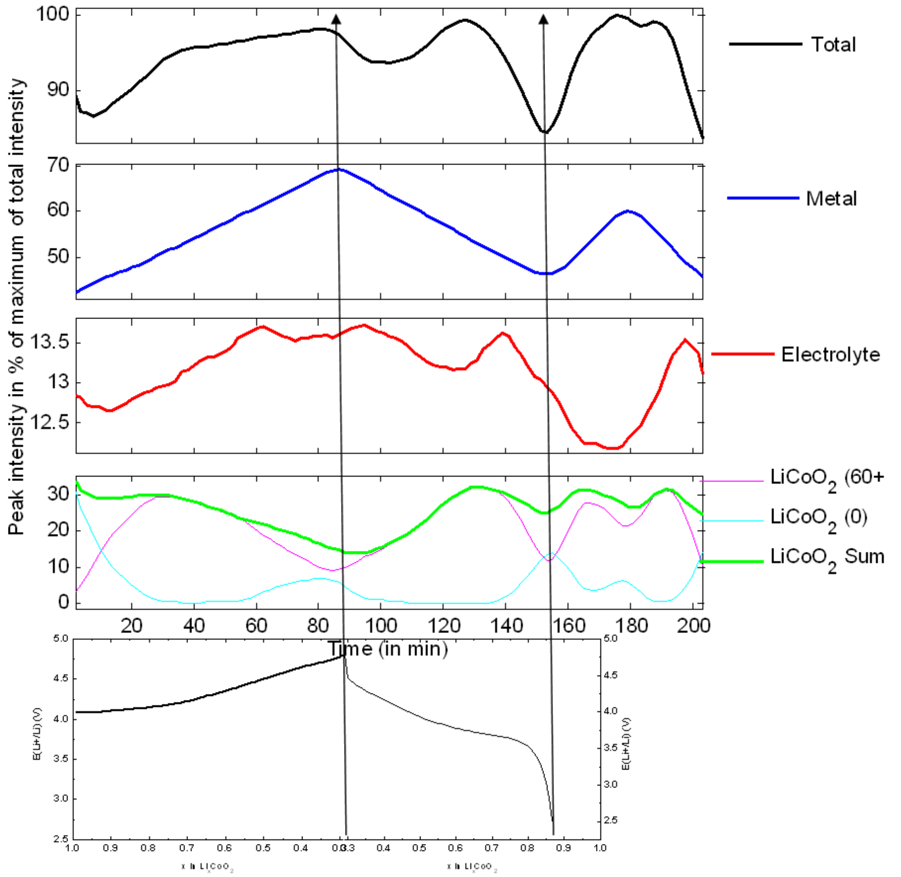

Figure 5.7. The fitted intensity of different resonances in a Li-desert rose LiCoO$_2$ *in situ* battery system upon two electrochemical cycles at a 1/2 C rate.

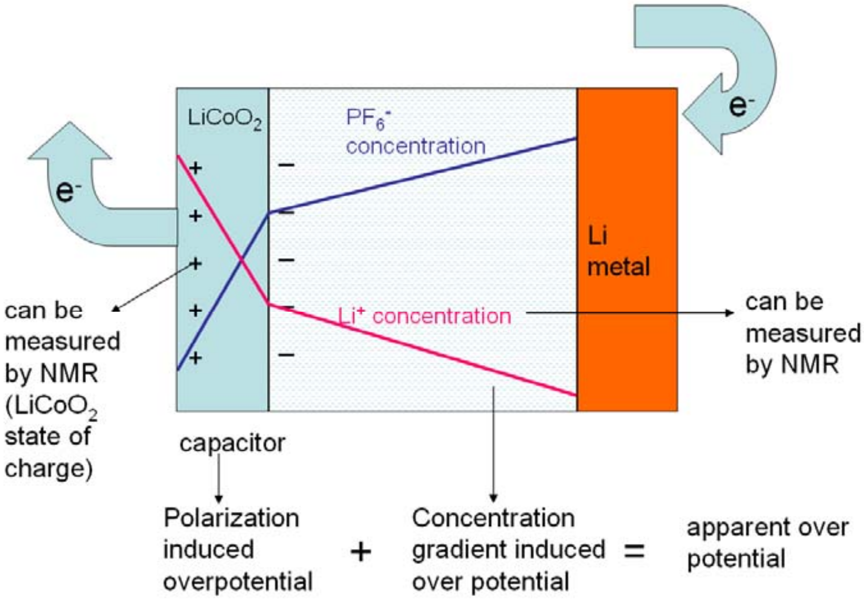

Figure 5.8. A tentative model for over potential fitting.

.

4. CONCLUSIONS AND IMPLICATIONS

The work discussed above demonstrated that the *in situ* ^{7}Li static NMR can be applied to a new system: Li-$LiCoO_2$, other than the first reported Li-carbon system and recently reported Li-Si system. More than just observation of the changes of the in situ spectra qualitatively, the intensity changes of different resonances, which are reasonably corresponding to the changes of the amount of different Li containing species in the *in situ* battery systems, can be extracted from the experimental spectra by fitting. Therefore it becomes possible to follow the Li ion transport in the battery quantitatively. For example, Fig. 5.8 shows a tentative model which may be used to calculate some kinetics parameters, such as the Li ion exchange rate from $LiCoO_2$ to the electrolyte, by fitting the apparent over potential of the system. Although, obviously a lot of necessary optimization and improvement on the experimental methods, the models and the NMR fitting protocols are required, this study still is still thought to be very possible and promising.

REFERENCES

1. Aurbach, D.; Levi, M. D.; Levi, E.; Teller, H.; Markovsky, B.; Salitra, G.; Heider, U.; Heider, L., *J. Electrochem. Soc.* **1998,** 145, (9), 3024-3034.
2. Jang, Y. I.; Neudecker, B. J.; Dudney, N. J., *Electrochem. Solid State Lett.* **2001,** 4, (6), A74-A77.
3. Levi, M. D.; Aurbach, D., *J. Phys. Chem. B* **1997,** 101, (23), 4641-4647.
4. Yu, P.; Popov, B. N.; Ritter, J. A.; White, R. E., *J. Electrochem. Soc.* **1999,** 146, (1), 8-14.
5. Zhao, J. S.; Wang, L.; He, X. M.; Wan, C. R.; Jiang, C. Y., *J. Electrochem. Soc.* **2008,** 155, (4), A292-A296.
6. Capiglia, C.; Saito, Y.; Kageyama, H.; Mustarelli, P.; Iwamoto, T.; Tabuchi, T.; Tukamoto, H. **J. Powder Sources**, **1999**, 81, 859-862.
7. Wagemaker, M.; Kentgens, A. P. M.; Mulder, F. M., *Nature* **2002,** 418, (6896), 397-399.
8. Wagemaker, M.; van Well, A. A.; Kearley, G. J.; Mulder, F. M. *Solid State Ionics*, **2004**, 175, 191-193.
9. Chevallier, F.; Letellier, M.; Morcrette, M.; Tarascon, J. M.; Frackowiak, E.; Rouzaud, J. N.; Beguin, F., *Electrochem. Solid State Lett.* **2003,** 6, (11), A225-A228.
10. Letellier, M.; Chevallier, F.; Clinard, C.; Frackowiak, E.; Rouzaud, J. N.; Beguin,

F.; Morcrette, M.; Tarascon, J. M., *J. Chem. Phys.* **2003,** 118, (13), 6038-6045.

11. Key, B.; Bhattacharyya, R.; Morcrette, M.; Sezne, V.; Tarascon, J. M.; Grey, C. P., *J. Am. Chem. Soc.* **2009**, (ASAP).

CHAPTER 6

CONCLUSIONS

The objective of this dissertation work is to improve the rate performance of the cathode materials of LIBs by controlling their particle size and morphology, with focus on the $LiMO_2$ type cathode materials. These morphological and particle size-controlling approaches have been demonstrated to be effective by the results from the $LiCoO_2$ nanoparticles (Chapter 2) and “desert rose” $LiCoO_2$ (Chapter 3). These $LiCoO_2$ materials, with small particle size and, more importantly, with electrochemically-favorable morphologies, showed much better rate performances than commercial $LiCoO_2$. The latter was synthesized using solid state reactions and has micrometer-particle sizes and electrochemically unfavorable morphologies. Rate performances of most of the known electrode materials largely depend on their morphologies, except for a few cases, e.g., $LiMn_2O_4$, which has a cubic structure and isotropic 3-D Li diffusion channels. Particle size also plays an important role for the rate performance of electrode materials. For some materials, such as $LiFePO_4$ and some newly developed conversion compounds, particle size is demonstrated to be a crucial factor for them to function well in batteries. Therefore the morphological and particle size-controlling approaches developed in this dissertation work are expected to be also useful for many other electrode materials.

Crystal growth mechanisms of the $LiMO_2$ type cathode materials were also studied, especially for the chosen model compound, $LiCoO_2$, in order to resolve the questions about how to control the morphology of the electrode materials. As two examples, the growth mechanisms of the “desert rose” form of $LiCoO_2$ and the concaved cuboctahedron form $LiCoO_2$ were proposed and supported by comprehensive experimental evidence. The results show that by choosing proper starting materials and by changing the concentrations of reagents in the initial reaction solutions and therefore by controlling the growth kinetics, it is feasible to tune particle size and morphology to be electrochemically favorable. A better understanding on the growth mechanism of electrode materials is very helpful to design synthetic methods.

Structural analysis on the cathode materials upon cycling, by using comprehensive techniques such as NMR, XRD and electron microscopy, both *ex situ* and *in situ*, provides insights of how cathode materials function in the cells. Such information can help to understand the rate limiting factors in a battery system. The 1st order phase transitions with high activation energies that occur during cycling, such as the O3-O1 transition of $LiCoO_2$ at high voltages, can be problematic for practical application. *In situ* NMR experiment results demonstrated that the electrochemical reactions can be monitored in real time. More importantly, with further improvement of this technique and with some modeling work, we believe it is feasible to quantitatively measure Li^+ flow across the cell and to provide insights into the rate limiting steps in the batteries. Such information will be very helpful for the development of new high power, high rate LIBs.

BIBLIOGRAPHY

CHAPTER 1

1. http://www.energy.gov/.
2. Tarascon, J. M.; Armand, M., *Nature* **2001,** 414, (6861), 359-367.
3. www.howstuffswork.com.
4. Ferg, E.; Gummow, R. J.; Dekock, A.; Thackeray, M. M., *J. Electrochem. Soc.* **1994,** 141, (11), L147-L150.
5. Zaghib, K.; Simoneau, M.; Armand, M.; Gauthier, M., *J. Power Sources* **1999,** 81, 300-305.
6. Cao, A. M.; Hu, J. S.; Liang, H. P.; Wan, L. J., *Angew. Chem. Int. Edit.* **2005,** 44, (28), 4391-4395.
7. West, K.; ZachauChristiansen, B.; Skaarup, S.; Saidi, Y.; Barker, J.; Olsen, II; Pynenburg, R.; Koksbang, R., *J. Electrochem. Soc.* **1996,** 143, (3), 820-825.
8. Kepler, K. D.; Vaughey, J. T.; Thackeray, M. M., *J. Power Sources* **1999,** 81, 383-387.
9. Tamura, N.; Ohshita, R.; Fujimoto, M.; Fujitani, S.; Kamino, M.; Yonezu, I., *J. Power Sources* **2002,** 107, (1), 48-55.
10. Poizot, P.; Laruelle, S.; Grugeon, S.; Dupont, L.; Tarascon, J. M., *Nature* **2000,** 407, (6803), 496-499.
11. Debart, A.; Dupont, L.; Poizot, P.; Leriche, J. B.; Tarascon, J. M., *J. Electrochem.*

Soc. **2001,** 148, (11), A1266-A1274.

12. Park, J. C.; Kim, J.; Kwon, H.; Song, H., *Adv. Mater.* **2009,** 21, (7), 803-+.
13. Mabuchi, A.; Tokumitsu, K.; Fujimoto, H.; Kasuh, T., *J. Electrochem. Soc.* **1995,** 142, (4), 1041-1046.
14. Richard, M. N.; Dahn, J. R., *J. Electrochem. Soc.* **1999,** 146, (6), 2068-2077.
15. Wang, Q.; Li, H.; Chen, L. Q.; Huang, X. J., *Solid State Ionics* **2002,** 152, 43-50.
16. Li, H.; Huang, X. J.; Chen, L. Q.; Wu, Z. G.; Liang, Y., *Electrochem. Solid State Lett.* **1999,** 2, (11), 547-549.
17. Li, H.; Huang, X. J.; Chen, L. Q.; Zhou, G. W.; Zhang, Z.; Yu, D. P.; Mo, Y. J.; Pei, N., *Solid State Ionics* **2000,** 135, 181-191.
18. Cui, L. F.; Ruffo, R.; Chan, C. K.; Peng, H. L.; Cui, Y., *Nano Lett.* **2009,** 9, (1), 491-495.
19. Chan, C. K.; Peng, H. L.; Liu, G.; McIlwrath, K.; Zhang, X. F.; Huggins, R. A.; Cui, Y., *Nat. Nanotechnol.* **2008,** 3, (1), 31-35.
20. Mizushima, K.; Jones, P. C.; Wiseman, P. J.; Goodenough, J. B., *Mater. Res. Bull.* **1980,** 15, (6), 783-789.
21. Dahn, J. R.; Vonsacken, U.; Juzkow, M. W.; Aljanaby, H., *J. Electrochem. Soc.* **1991,** 138, (8), 2207-2211.
22. Ohzuku, T.; Makimura, Y., *Chem. Lett.* **2001**, (7), 642-643.
23. Thackeray, M. M.; David, W. I. F.; Bruce, P. G.; Goodenough, J. B., *Mater. Res. Bull.* **1983,** 18, (4), 461-472.

24. Thackeray, M. M.; Johnson, P. J.; Depicciotto, L. A.; Bruce, P. G.; Goodenough, J. B., *Mater. Res. Bull.* **1984,** 19, (2), 179-187.

25. Padhi, A. K.; Nanjundaswamy, K. S.; Goodenough, J. B., *J. Electrochem. Soc.* **1997,** 144, (4), 1188-1194.

26. Chung, S. Y.; Bloking, J. T.; Chiang, Y. M., *Nat. Mater.* **2002,** 1, (2), 123-128.

27. Yamada, A.; Chung, S. C.; Hinokuma, K., *J. Electrochem. Soc.* **2001,** 148, (3), A224-A229.

28. Huang, H.; Yin, S. C.; Nazar, L. F., *Electrochem. Solid State Lett.* **2001,** 4, (10), A170-A172.

29. Yang, S. F.; Zavalij, P. Y.; Whittingham, M. S., *Electrochem. Commun.* **2001,** 3, (9), 505-508.

30. Li, G. H.; Azuma, H.; Tohda, M., *Electrochem. Solid State Lett.* **2002,** 5, (6), A135-A137.

31. Delacourt, C.; Poizot, P.; Morcrette, M.; Tarascon, J. M.; Masquelier, C., *Chem. Mater.* **2004,** 16, (1), 93-99.

32. Li, H.; Balaya, P.; Maier, J., *J. Electrochem. Soc.* **2004,** 151, (11), A1878-A1885.

33. Li, H.; Richter, G.; Maier, J., *Adv. Mater.* **2003,** 15, (9), 736-739.

34. Zhao, J. S.; Wang, L.; He, X. M.; Wan, C. R.; Jiang, C. Y., *J. Electrochem. Soc.* **2008,** 155, (4), A292-A296.

35. Capiglia, C.; Saito, Y.; Kageyama, H.; Mustarelli, P.; Iwamoto, T.; Tabuchi, T.; Tukamoto, H., *J. Power Sources* **1999,** 81, 859-862.

36. Doyle, M.; Newman, J.; Gozdz, A. S.; Schmutz, C. N.; Tarascon, J. M., *J. Electrochem. Soc.* **1996,** 143, (6), 1890-1903.

37. Xie, J.; Imanishi, N.; Matsumura, T.; Hirano, A.; Takeda, Y.; Yamamoto, O., *Solid State Ionics* **2008,** 179, (9-10), 362-370.

38. Dokko, K.; Mohamedi, M.; Fujita, Y.; Itoh, T.; Nishizawa, M.; Umeda, M.; Uchida, I., *J. Electrochem. Soc.* **2001,** 148, (5), A422-A426.

39. Xia, H.; Lu, L.; Meng, Y. S.; Ceder, G., *J. Electrochem. Soc.* **2007,** 154, (4), A337-A342.

40. Kim, D. H.; Kim, J., *Electrochem. Solid State Lett.* **2006,** 9, (9), A439-A442.

41. Bao, S. J.; Liang, Y. Y.; Zhou, W. H.; He, B. L.; Li, H. L., *J. Power Sources* **2006,** 154, (1), 239-245.

42. Sun, Y. K.; Myung, S. T.; Kim, M. H.; Prakash, J.; Amine, K., *J. Electrochem. Soc.* **2005,** 127, (38), 13411-13418.

43. Chen, H. L.; Qiu, X. P.; Zhu, W. T.; Hagenmuller, P., *Electrochem. Commun.* **2002,** 4, (6), 488-491.

44. Hwang, B. J.; Santhanam, R.; Liu, D. G., *J. Power Sources* **2001,** 97-8, 443-446.

45. Park, D. H.; Lim, S. T.; Hwang, S. J.; Yoon, C. S.; Sun, Y. K.; Choy, J. H., *Adv. Mater.* **2005,** 17, (23), 2834-+.

46. Zhou, Y. K.; Huang, J.; Li, H. L., *Appl. Phys. B-Lasers Opt.* **2003,** 76, (1), 53-57.

47. Zhou, Y. K.; Huang, J.; Shen, C. M.; Li, H. L., *Mater. Sci. Eng. A-Struct. Mater. Prop. Microstruct. Process.* **2002,** 335, (1-2), 260-267.

48. Hosono, E.; Kudo, T.; Honma, I.; Matsuda, H.; Zhou, H. S., *Nano Lett.* **2009,** 9, (3), 1045-1051.

49. Li, N. C.; Patrissi, C. J.; Che, G. L.; Martin, C. R., *J. Electrochem. Soc.* **2000,** 147, (6), 2044-2049.

50. Sides, C. R.; Martin, C. R., *Adv. Mater.* **2005,** 17, (1), 125-+.

51. Breger, J.; Kang, K.; Cabana, J.; Ceder, G.; Grey, C. P., *J. Mater. Chem.* **2007,** 17, (30), 3167-3174.

52. Kang, K. S.; Meng, Y. S.; Breger, J.; Grey, C. P.; Ceder, G., *Science* **2006,** 311, (5763), 977-980.

53. Zhang, Q. T.; Qu, M. Z.; Niu, H.; Yu, Z. L., *New Carbon Mater.* **2007,** 22, (4), 361-364.

54. Li, X. L.; Kang, F. Y.; Bai, X. D.; Shen, W., *Electrochem. Commun.* **2007,** 9, (4), 663-666.

55. Li, X. L.; Kang, F. Y.; Shen, W. C., *Carbon* **2006,** 44, (7), 1334-1336.

56. Li, X. L.; Kang, F. Y.; Shen, W. C., *Electrochem. Solid State Lett.* **2006,** 9, (3), A126-A129.

57. Yang, X. L.; Wen, Z. Y.; Huang, S. H.; Zhu, X. J.; Zhang, X. F., *Solid State Ionics* **2006,** 177, 2807-2810.

58. Kang, B.; Ceder, G., *Nature* **2009,** 458, (7235), 190-193.

59. Lee, K. P.; Manesh, K. M.; Kim, K. S.; Gopalan, A. Y., *J. Nanosci. Nanotechnol.* **2009,** 9, (1), 417-422.

60. Zhou, F.; Zhao, X. M.; Liu, Y. Q.; Li, L.; Yuan, C. G., *J. Phys. Chem. Solids* **2008,** 69, (8), 2061-2065.

61. Bates, J. B.; Dudney, N. J.; Neudecker, B. J.; Hart, F. X.; Jun, H. P.; Hackney, S. A., *J. Electrochem. Soc.* **2000,** 147, (1), 59-70.

62. Wang, H. F.; Jang, Y. I.; Huang, B. Y.; Sadoway, D. R.; Chiang, Y. T., *J. Electrochem. Soc.* **1999,** 146, (2), 473-480.

63. Amatucci, G. G.; Tarascon, J. M.; Klein, L. C., *J. Electrochem. Soc.* **1996,** 143, (3), 1114-1123.

64. Ozawa, K., *Solid State Ionics* **1994,** 69, (3-4), 212-221.

65. Rougier, A.; Gravereau, P.; Delmas, C., *J. Electrochem. Soc.* **1996,** 143, (4), 1168-1175.

66. Peres, J. P.; Weill, F.; Delmas, C., *Solid State Ionics* **1999,** 116, (1-2), 19-27.

67. Wang, M. J.; Navrotsky, A., *Solid State Ionics* **2004,** 166, (1-2), 167-173.

68. Whitfield, P. S.; Davidson, I. J.; Cranswick, L. M. D.; Swainson, I. P.; Stephens, P. W., *Solid State Ionics* **2005,** 176, (5-6), 463-471.

69. Hirayama, M.; Sakamoto, K.; Hiraide, T.; Mori, D.; Yamada, A.; Kanno, R.; Sonoyama, N.; Tamura, K.; Mizuki, J., *Electrochim. Acta* **2007,** 53, (2), 871-881.

70. Hirayama, M.; Sonoyama, N.; Abe, T.; Minoura, M.; Ito, M.; Mori, D.; Yamada, A.; Kanno, R.; Terashima, T.; Takano, M.; Tamura, K.; Mizuki, J., *J. Power Sources* **2007,** 168, (2), 493-500.

71. Gummow, R. J.; Dekock, A.; Thackeray, M. M., *Solid State Ionics* **1994,** 69, (1),

59-67.

72. Jang, D. H.; Shin, Y. J.; Oh, S. M., *J. Electrochem. Soc.* **1996,** 143, (7), 2204-2211.

73. Xia, Y. Y.; Zhou, Y. H.; Yoshio, M. *J. Electrochem. Soc.* **1997**, 144, 2593-2600.

74. Amine, K.; Tukamoto, H.; Yasuda, H.; Fujita, Y., *J. Electrochem. Soc.* **1996,** 143, (5), 1607-1613.

75. Arora, P.; Popov, B. N.; White, R. E., *J. Electrochem. Soc.* **1998,** 145, (3), 807-815.

76. Ravet, N.; Chouinard, Y.; Magnan, J. F.; Besner, S.; Gauthier, M.; Armand, M., *J. Power Sources* **2001,** 97-8, 503-507.

77. Wang, L.; Zhou, F.; Meng, Y. S.; Ceder, G., *Phys. Rev. B* **2007,** 76, (16).

78. Islam, M. S.; Driscoll, D. J.; Fisher, C. A. J.; Slater, P. R., *Chem. Mater.* **2005,** 17, (20), 5085-5092.

79. Nishimura, S.; Kobayashi, G.; Ohoyama, K.; Kanno, R.; Yashima, M.; Yamada, A., *Nat. Mater.* **2008,** 7, (9), 707-711.

CHAPTER 2

1. Ohzuku, T.; Makimura, Y., *Chem. Lett.* **2001**, (7), 642-643.
2. Chen, H. L.; Qiu, X. P.; Zhu, W. T.; Hagenmuller, P., *Electrochem. Commun.* **2002,** 4, (6), 488-491.
3. Thurston, T. R.; Jisrawi, N. M.; Mukerjee, S.; Yang, X. Q.; McBreen, J.; Daroux, M. L.; Xing, X. K., *Appl. Phys. Lett.* **1996,** 69, (2), 194-196.
4. Okubo, M.; Hosono, E.; Kim, J.; Enomoto, M.; Kojima, N.; Kudo, T.; Zhou, H. S.; Honma, I., *J. Am. Chem. Soc.* **2007,** 129, (23), 7444-7452.
5. Levasseur, S.; Menetrier, M.; Delmas, C., *Chem. Mater.* **2002,** 14, (8), 3584-3590.
6. Levasseur, S.; Menetrier, M.; Suard, E.; Delmas, C., *Solid State Ionics* **2000,** 128, (1-4), 11-24.
7. Menetrier, M.; Carlier, D.; Blangero, M.; Delmas, C., *Electrochem. Solid State Lett.* **2008,** 11, (11), A179-A182.
8. Menetrier, M.; Saadoune, I.; Levasseur, S.; Delmas, C., *J. Mater. Chem.* **1999,** 9, (5), 1135-1140.
9. Menetrier, M.; Shao-Horn, Y.; Wattiaux, A.; Fournes, L.; Delmas, C., *Chem. Mater.* **2005,** 17, (18), 4653-4659.
10. Amatucci, G. G.; Tarascon, J. M.; Larcher, D.; Klein, L. C., *Solid State Ionics* **1996,** 84, (3-4), 169-180.
11. Larcher, D.; Palacin, M. R.; Amatucci, G. G.; Tarascon, J. M., *J. Electrochem. Soc.* **1997,** 144, (2), 408-417.

12. Aurbach, D.; Markovsky, B.; Rodkin, A.; Cojocaru, M.; Levi, E.; Kim, H. J., *Electrochim. Acta* **2002,** 47, (12), 1899-1911.

13. Wang, Z. X.; Liu, L. J.; Chen, L. Q.; Huang, X. J., *Solid State Ionics* **2002**, 148, 335-342.

14. Casas-Cabanas, M.; Rodriguez-Carvajal, J.; Canales-Vazquez, J.; Palacin, M. R., *J. Mater. Chem.* **2006,** 16, (28), 2925-2939.

15. Du, K.; Yang, Y. N.; Hu, G. R.; Peng, Z. D.; Qi, L., *Chin. J. Inorg. Chem.* **2008,** 24, (4), 615-620.

16. Chang, Z. R.; Chen, Z. J.; Wu, F.; Tang, H. W.; Zhu, Z. H., *Acta Phys.-Chim. Sin.* **2008,** 24, (3), 513-519.

17. Reddy, M. V.; Rao, G. V. S.; Chowdari, B. V. R., *J. Phys. Chem. C* **2007,** 111, (31), 11712-11720.

18. Ni, J. F.; Zhou, H. H.; Chen, J. T.; Zhang, X. X., *Mater. Lett.* **2007,** 61, (4-5), 1260-1264.

19. Reddy, M. V.; Rao, G. V. S.; Chowdari, B. V. R., *J. Power Sources* **2006,** 159, (1), 263-267.

20. Wen, L.; Lu, Q.; Xu, G. X., *Electrochim. Acta* **2005,** 51, (21), 4388-4392.

21. Du, K.; Qi, L.; Hu, G. R.; Peng, Z. D., *Chin. J. Inorg. Chem.* **2006,** 22, (5), 867-871.

22. Tan, K. S.; Reddy, M. V.; Rao, G. V. S.; Chowdari, B., *J. Power Sources* **2005,** 147, (1-2), 241-248.

23. Kim, J. H.; Myung, S. T.; Sun, Y. K., *Electrochim. Acta* **2004,** 49, (2), 219-227.

24. Han, C. H.; Hong, Y. S.; Kim, K., *Solid State Ionics* **2003,** 159, (3-4), 241-247.

25. Han, C. H.; Hong, Y. S.; Park, C. M.; Kim, K., *J. Power Sources* **2001,** 92, (1-2), 95-101.

26. Liang, H. Y.; Qiu, X. P.; Chen, H. L.; He, Z. Q.; Zhu, W. T.; Chen, L. Q., *Electrochem. Commun.* **2004,** 6, (8), 789-794.

27. Liang, H. Y.; Qiu, X. P.; Zhang, S. C.; He, Z. Q.; Zhu, W. T.; Chen, L. Q., *Electrochem. Commun.* **2004,** 6, (5), 505-509.

28. Breger, J.; Meng, Y. S.; Hinuma, Y.; Kumar, S.; Kang, K.; Shao-Horn, Y.; Ceder, G.; Grey, C. P., *Chem. Mater.* **2006,** 18, (20), 4768-4781.

29. Breger, J.; Dupre, N.; Chupas, P. J.; Lee, P. L.; Proffen, T.; Parise, J. B.; Grey, C. P., *J. Am. Chem. Soc.* **2005,** 127, (20), 7529-7537.

30. Meng, Y. S.; Ceder, G.; Grey, C. P.; Yoon, W. S.; Shao-Horn, Y., *Electrochem. Solid State Lett.* **2004,** 7, (6), A155-A158.

31. Yoon, W. S.; Grey, C. P.; Balasubramanian, M.; Yang, X. Q.; McBreen, J., *Chem. Mater.* **2003,** 15, (16), 3161-3169.

32. Yoon, W. S.; Paik, Y.; Yang, X. Q.; Balasubramanian, M.; McBreen, J.; Grey, C. P., *Electrochem. Solid State Lett.* **2002,** 5, (11), A263-A266.

33. Chemova, N. A.; Ma, M.; Xiao, J.; Whittingham, M. S.; Breger, J.; Grey, C. P., *Chem. Mater.* **2007,** 19, (19), 4682-4693.

34. Yoon, W. S.; Balasubramanian, M.; Chung, K. Y.; Yang, X. Q.; McBreen, J.; Grey,

C. P.; Fischer, D. A., *J. Am. Chem. Soc.* **2005,** 127, (49), 17479-17487.

35. Yoon, W. S.; Grey, C. P.; Balasubramanian, M.; Yang, X. Q.; Fischer, D. A.; McBreen, J., *Electrochem. Solid State Lett.* **2004,** 7, (3), A53-A55.

36. Lee, Y. J.; Grey, C. P., *J. Electrochem. Soc.* **2002,** 149, (2), A103-A114.

37. Lee, Y. J.; Park, S. H.; Eng, C.; Parise, J. B.; Grey, C. P., *Chem. Mater.* **2002,** 14, (1), 194-205.

38. Lee, Y. J.; Grey, C. P., *Chem. Mater.* **2000,** 12, (12), 3871-3878.

39. Lee, Y. J.; Wang, F.; Mukerjee, S.; McBreen, J.; Grey, C. P., *J. Electrochem. Soc.* **2000,** 147, (3), 803-812.

40. Lee, Y. J.; Wang, F.; Grey, C. P., *J. Am. Chem. Soc.* **1998,** 120, (48), 12601-12613.

41. Zeng, D. L.; Cabana, J.; Breger, J. L.; Yoon, W. S.; Grey, C. P., *Chem. Mater.* **2007,** 19, (25), 6277-6289.

42. Mukai, K.; Ikedo, Y.; Nozaki, H.; Sugiyama, J.; Nishiyama, K.; Andreica, D.; Amato, A.; Russo, P. L.; Ansaldo, E. J.; Brewer, J. H.; Chow, K. H.; Ariyoshi, K.; Ohzuku, T., *Phys. Rev. Lett.* **2007,** 99, (8).

43. Amatucci, G. G.; Tarascon, J. M.; Klein, L. C., *J. Electrochem. Soc.* **1996,** 143, (3), 1114-1123.

44. Yang, X. Q.; Sun, X.; McBreen, J., *Electrochem. Commun.* **2000,** 2, (2), 100-103.

45. Ohzuku, T.; Ueda, A.; Yamamoto, N., *J. Electrochem. Soc.* **1995,** 142, (5), 1431-1435.

46. Sun, X.; Yang, X. Q.; McBreen, J.; Gao, Y.; Yakovleva, M. V.; Xing, X. K.;

Daroux, M. L., *J. Power Sources* **2001,** 97-8, 274-276.

47. Van der Ven, A.; Aydinol, M. K.; Ceder, G.; Kresse, G.; Hafner, J., *Phys. Rev. B* **1998,** 58, (6), 2975-2987.

48. Van der Ven, A.; Aydinol, M. K.; Ceder, G., *J. Electrochem. Soc.* **1998,** 145, (6), 2149-2155.

49. Kavan, L.; Prochazka, J.; Spitler, T. M.; Kalbac, M.; Zukalova, M. T.; Drezen, T.; Gratzel, M., *J. Electrochem. Soc.* **2003,** 150, (7), A1000-A1007.

50. Gibot, P.; Casas-Cabanas, M.; Laffont, L.; Levasseur, S.; Carlach, P.; Hamelet, S.; Tarascon, J. M.; Masquelier, C., *Nat. Mater.* **2008,** 7, (9), 741-747.

51. Carlier, D.; Saadoune, I.; Croguennec, L.; Menetrier, M.; Suard, E.; Delmas, C., *Solid State Ionics* **2001,** 144, (3-4), 263-276.

52. Pereira, N.; Al-Sharab, J. F.; Cosandey, F.; Badway, F.; Amatucci, G. G., *J. Electrochem. Soc.* **2008,** 155, (11), A831-A838.

53. Sun, Y. K.; Cho, S. W.; Lee, S. W.; Yoon, C. S.; Amine, K., *J. Electrochem. Soc.* **2007,** 154, (3), A168-A172.

54. Sun, Y. K.; Han, J. M.; Myung, S. T.; Lee, S. W.; Amine, K., *Electrochem. Commun.* **2006,** 8, (5), 821-826.

55. Woo, S. U.; Yoon, C. S.; Amine, K.; Belharouak, I.; Sun, Y. K., *J. Electrochem. Soc.* **2007,** 154, (11), A1005-A1009.

56. Park, B. C.; Kim, H. B.; Myung, S. T.; Amine, K.; Belharouak, I.; Lee, S. M.; Sun, Y. K. *J. Power Sources* **2008**, 178, 826-831.

CHAPTER 3

1. Du, K.; Yang, Y. N.; Hu, G. R.; Peng, Z. D.; Qi, L., *Chin. J. Inorg. Chem.* **2008,** 24, (4), 615-620.
2. Chang, Z. R.; Chen, Z. J.; Wu, F.; Tang, H. W.; Zhu, Z. H., *Acta Phys.-Chim. Sin.* **2008,** 24, (3), 513-519.
3. Reddy, M. V.; Rao, G. V. S.; Chowdari, B. V. R., *J. Phys. Chem. C* **2007,** 111, (31), 11712-11720.
4. Ni, J. F.; Zhou, H. H.; Chen, J. T.; Zhang, X. X., *Mater. Lett.* **2007,** 61, (4-5), 1260-1264.
5. Reddy, M. V.; Rao, G. V. S.; Chowdari, B. V. R., *J. Power Sources* **2006,** 159, (1), 263-267.
6. Wen, L.; Lu, Q.; Xu, G. X., *Electrochim. Acta* **2005,** 51, (21), 4388-4392.
7. Du, K.; Qi, L.; Hu, G. R.; Peng, Z. D., *Chin. J. Inorg. Chem.* **2006,** 22, (5), 867-871.
8. Tan, K. S.; Reddy, M. V.; Rao, G. V. S.; Chowdari, B., *J. Power Sources* **2005,** 147, (1-2), 241-248.
9. Kim, J. H.; Myung, S. T.; Sun, Y. K., *Electrochim. Acta* **2004,** 49, (2), 219-227.
10. Han, C. H.; Hong, Y. S.; Kim, K., *Solid State Ionics* **2003,** 159, (3-4), 241-247.
11. Han, C. H.; Hong, Y. S.; Park, C. M.; Kim, K., *J. Power Sources* **2001,** 92, (1-2), 95-101.
12. Liang, H. Y.; Qiu, X. P.; Chen, H. L.; He, Z. Q.; Zhu, W. T.; Chen, L. Q.,

Electrochem. Commun. **2004,** 6, (8), 789-794.

13. Liang, H. Y.; Qiu, X. P.; Zhang, S. C.; He, Z. Q.; Zhu, W. T.; Chen, L. Q., *Electrochem. Commun.* **2004,** 6, (5), 505-509.
14. Breger, J.; Kang, K.; Cabana, J.; Ceder, G.; Grey, C. P., *J. Mater. Chem.* **2007,** 17, (30), 3167-3174.
15. Kang, K. S.; Meng, Y. S.; Breger, J.; Grey, C. P.; Ceder, G., *Science* **2006,** 311, (5763), 977-980.
16. Ohzuku, T.; Makimura, Y., *Chem. Lett.* **2001**, (8), 744-745.
17. Yabuuchi, N.; Ohzuku, T. *J. Power Sources* **2003**, 119, 171-174.
18. Chung, S. Y.; Bloking, J. T.; Chiang, Y. M., *Nat. Mater.* **2002,** 1, (2), 123-128.
19. Bao, S. J.; Liang, Y. Y.; Zhou, W. H.; He, B. L.; Li, H. L., *J. Power Sources* **2006,** 154, (1), 239-245.
20. Sun, Y. K.; Myung, S. T.; Kim, M. H.; Prakash, J.; Amine, K., *J. Am. Chem. Soc.* **2005,** 127, (38), 13411-13418.
21. Chen, H. L.; Qiu, X. P.; Zhu, W. T.; Hagenmuller, P., *Electrochem. Commun.* **2002,** 4, (6), 488-491.
22. Sides, C. R.; Martin, C. R., *Adv. Mater.* **2005,** 17, (1), 125-+.
23. Larcher, D.; Palacin, M. R.; Amatucci, G. G.; Tarascon, J. M., *J. Electrochem. Soc.* **1997,** 144, (2), 408-417.
24. Amatucci, G. G.; Tarascon, J. M.; Larcher, D.; Klein, L. C., *Solid State Ionics* **1996,** 84, (3-4), 169-180.

25. Okubo, M.; Hosono, E.; Kim, J.; Enomoto, M.; Kojima, N.; Kudo, T.; Zhou, H. S.; Honma, I., *J. Am. Chem. Soc.* **2007,** 129, (23), 7444-7452.

26. Hu, C. G.; Liu, H.; Dong, W. T.; Zhang, Y. Y.; Bao, G.; Lao, C. S.; Wang, Z. L., *Adv. Mater.* **2007,** 19, (3), 470-+.

27. Liu, H.; Hu, C. G.; Wang, Z. L., *Nano Lett.* **2006,** 6, (7), 1535-1540.

28. Zhu, J.; Peng, H. L.; Chan, C. K.; Jarausch, K.; Zhang, X. F.; Cui, Y., *Nano Lett.* **2007,** 7, (4), 1095-1099.

29. Bierman, M. J.; Lau, Y. K. A.; Jin, S., *Nano Lett.* **2007,** 7, (9), 2907-2912.

30. Pralong, V.; Delahaye-Vidal, A.; Beaudoin, B.; Gerand, B.; Tarascon, J. M., *J. Mater. Chem.* **1999,** 9, (4), 955-960.

31. Chiang, Y. M.; Jang, Y. I.; Wang, H. F.; Huang, B. Y.; Sadoway, D. R.; Ye, P. X., *J. Electrochem. Soc.* **1998,** 145, (3), 887-891.

32. Levasseur, S.; Menetrier, M.; Suard, E.; Delmas, C., *Solid State Ionics* **2000,** 128, (1-4), 11-24.

33. Menetrier, M.; Saadoune, I.; Levasseur, S.; Delmas, C., *J. Mater. Chem.* **1999,** 9, (5), 1135-1140.

34. Levasseur, S.; Menetrier, M.; Delmas, C., *Chem. Mater.* **2002,** 14, (8), 3584-3590.

35. Menetrier, M.; Carlier, D.; Blangero, M.; Delmas, C., *Electrochem. Solid State Lett.* **2008,** 11, (11), A179-A182.

36. Menetrier, M.; Shao-Horn, Y.; Wattiaux, A.; Fournes, L.; Delmas, C., *Chem. Mater.* **2005,** 17, (18), 4653-4659.

CHAPTER 4

1. Jang, D. H.; Shin, Y. J.; Oh, S. M. *J. Electrochem. Soc.* **1996,** *143,* (7), 2204-2211.
2. Xia, Y. Y.; Zhou, Y. H.; Yoshio, M. *J. Electrochem. Soc.* **1997,** *144,* 2593-2600.
3. Chung, S. Y.; Bloking, J. T.; Chiang, Y. M. *Nat. Mater.* **2002,** *1,* (2), 123-128.
4. Huang, H.; Yin, S. C.; Nazar, L. F. *Electrochem. Solid State Lett.* **2001,** *4*, (10), A170-A172.
5. Yamada, A.; Chung, S. C.; Hinokuma, K. *J. Electrochem. Soc.* **2001,** *148*, (3), A224-A229.
6. Islam, M. S.; Driscoll, D. J.; Fisher, C. A. J.; Slater, P. R. *Chem. Mater.* **2005,** *17*, (20), 5085-5092.
7. Nishimura, S.; Kobayashi, G.; Ohoyama, K.; Kanno, R.; Yashima, M.; Yamada, A. *Nat. Mater.* **2008,** *7*, (9), 707-711.
8. Wu, C. Y.; Yu, S. H.; Antonietti, M. *Chem. Mater.* **2006,** *18*, (16), 3599-3601.
9. Vayssieres, L.; Keis, K.; Hagfeldt, A.; Lindquist, S. E. *Chem. Mater.* **2001,** *13*, (12), 4395.
10. Lobachev, A. N. Crystallization processes under hydrothermal conditions. **1973**.
11. Okubo, M.; Hosono, E.; Kim, J.; Enomoto, M.; Kojima, N.; Kudo, T.; Zhou, H. S.; Honma, I. *J. Am. Chem. Soc.* **2007,** *129*, (23), 7444-7452.

CHAPTER 5

1. Aurbach, D.; Levi, M. D.; Levi, E.; Teller, H.; Markovsky, B.; Salitra, G.; Heider, U.; Heider, L., *J. Electrochem. Soc.* **1998,** 145, (9), 3024-3034.
2. Jang, Y. I.; Neudecker, B. J.; Dudney, N. J., *Electrochem. Solid State Lett.* **2001,** 4, (6), A74-A77.
3. Levi, M. D.; Aurbach, D., *J. Phys. Chem. B* **1997,** 101, (23), 4641-4647.
4. Yu, P.; Popov, B. N.; Ritter, J. A.; White, R. E., *J. Electrochem. Soc.* **1999,** 146, (1), 8-14.
5. Zhao, J. S.; Wang, L.; He, X. M.; Wan, C. R.; Jiang, C. Y., *J. Electrochem. Soc.* **2008,** 155, (4), A292-A296.
6. Capiglia, C.; Saito, Y.; Kageyama, H.; Mustarelli, P.; Iwamoto, T.; Tabuchi, T.; Tukamoto, H. **J. Powder Sources**, **1999**, 81, 859-862.
7. Wagemaker, M.; Kentgens, A. P. M.; Mulder, F. M., *Nature* **2002,** 418, (6896), 397-399.
8. Wagemaker, M.; van Well, A. A.; Kearley, G. J.; Mulder, F. M. *Solid State Ionics*, **2004**, 175, 191-193.
9. Chevallier, F.; Letellier, M.; Morcrette, M.; Tarascon, J. M.; Frackowiak, E.; Rouzaud, J. N.; Beguin, F., *Electrochem. Solid State Lett.* **2003,** 6, (11), A225-A228.
10. Letellier, M.; Chevallier, F.; Clinard, C.; Frackowiak, E.; Rouzaud, J. N.; Beguin, F.; Morcrette, M.; Tarascon, J. M., *J. Chem. Phys.* **2003,** 118, (13), 6038-6045.

11. Key, B.; Bhattacharyya, R.; Morcrette, M.; Sezne, V.; Tarascon, J. M.; Grey, C. P., *J. Am. Chem. Soc.* **2009**, (ASAP).